UNIVERSITY OF LIVERPOOL

UNCERTAINTY QUANTIFICATION AND MANAGEMENT IN OPERATIONAL MODAL ANALYSIS WITH MULTIPLE SETUPS

Thesis submitted in accordance with the requirements of

the University of Liverpool for

the degree of Doctor in Philosophy

By

Yan-Long Xie

September 2018

ABSTRACT

Operational modal analysis (OMA) aims at identifying the structural modal properties (e.g., natural frequencies, damping ratios and mode shapes) using ambient vibration data that is measured when the structure is under its working condition. Due to its economy in implementation, OMA has attracted considerable attention in field testing of civil engineering structures. Considering practical constraints (e.g., budget) in field tests, a multiple-setup strategy is often employed to measure a large number of degrees of freedom with a limited number of sensors. In ambient vibration tests, the input loading is not measured. Because of this, the identification uncertainty of modal parameters can become significant. Different test configurations can yield different levels of uncertainty. It is therefore desirable to quantitatively assess the identification uncertainty and investigate how it is related to test configuration. For planning purpose, especially for multiple setups, it is desirable to have an uncertainty-based assessment for a given test configuration. Motivated by the above concerns, the research in this thesis aims at quantifying and managing identification uncertainties in OMA with multiple setups.

Based on a Bayesian modal identification framework, uncertainty quantification is first addressed by investigating the computation of the 'posterior covariance matrix' from the inverse of the Hessian of the negative log-likelihood function of modal parameters. Difficulties arise in deriving the Hessian matrix since the modal parameters are subjected to constraints, e.g., the mode shape is subjected to a scaling constraint. A theoretical framework is developed for evaluating the Hessian of a function under general constraints. The theory is applied to Bayesian OMA with single setup and multiple setups, where new analytical expressions for calculating the

posterior covariance matrix are derived. Numerical examples are also provided to validate the proposed theory.

The uncertainty management of multiple setups is addressed by investigating the leading order behaviour of the posterior covariance matrix. For sufficiently long data, the posterior covariance matrix is asymptotically equal to the inverse of the Fisher Information Matrix (FIM). A closed-form asymptotic expression for the FIM is derived with small damping and high modal signal-to-noise ratio. Leveraging on the asymptotic decoupling of modal parameters, the dimension of the FIM can be reduced, making the inverse algebraically manageable. This leads to closed-form expressions of the leading order posterior coefficient of variation (standard deviation / mean) of the modal parameters. The collection of these results is referred as 'uncertainty law' of multiple setups, which reveals how identification uncertainty is related to test configuration. Investigation into the uncertainty law provides engineering guidance for the experimental design of multiple setups. Illustrative examples with synthetic, laboratory and field test data are presented to validate the proposed theory. The uncertainty law is applied for multiple-setup ambient vibration test of an office building and a suspension footbridge, where the test configuration is quantitatively assessed from an uncertainty point of view.

ACKNOWLEDGEMENTS

First and foremost, I would like to express my sincere gratitude to my supervisor Prof. Siu-Kui Au, for his continuous guidance and encouragement during my Ph.D. study. He shepherded me into the scientific world and guided me with a rigorous attitude towards research. I still remember 'Cargo-Cult Science', the first paper that he recommended to me. It is a great honour to conduct research under his supervision.

Secondly, my sincere thanks go to Prof. James Brownjohn at the University of Exeter and Prof. Mitsuyoshi Akiyama at Waseda University, for offering me opportunities to conduct field tests and apply OMA to situations outside my expertise. I would also like to thank the technician staff at the university of Liverpool, Mr Raymond Edun and Mr Derek Neary. Special thanks also go to my colleagues and academic staff at the School of Engineering, for their kind suggestions and supports. They include Dr. Bin-Bin Li, Dr. Xiao-Jun Wei, Dr. Jing Yang, Dr. Shan-Cheng Cao, Mr. Yi-Chen Zhu, Miss. Xin-Rui Wang and Mr. Zuo Zhu. I am grateful to the Chinese Scholarship Council and the University of Liverpool for the financial support, as well as the UK Engineering and Physical Sciences Research Council (Grant EP/N017897/1).

Finally, I would like to express my deep gratitude to my parents. Without their support and encouragement, I would never have been able to reach this goal. My greatest appreciation goes to my fiancée, Si-Min Dong, for her care and company during my Ph.D. life with unfailing tolerance and understanding.

TABLE OF CONTENTS

LIST OF FIGURES

LIST OF TABLES

NOMENCLATURE

c.o.v.	Coefficient of variation
CRB	Cramér-Rao bound
DOF	Degree(s) of freedom
FFT	Fast Fourier transform
FIM	Fisher information matrix
MPV	Most probable value
NL	Negative logarithm function
NLLF	Negative log-likelihood function
OMA	Operational modal analysis
PDF	Probability density function
PSD	Power spectral density
RHS	Right-hand side
SHM	Structural health monitoring
s/n	Signal-to-noise ratio
SSI	Stochastic subspace identification
SVD	Singular value decomposition
w.r.t.	With respect to

Chapter 1 Introduction

1.1 Background

Civil infrastructure provides fundamental support for human living and daily activities. Establishing a stable, healthy and well-adjusted urban community requires the civil infrastructure system to be sustainable and reliable. A large proportion of existing infrastructure in many countries was built during their fast economic growth periods. After decades of booming development, an enormous amount of civil infrastructure is now facing deterioration problems, accompanied by threats from natural (e.g., floods, earthquakes and storms) and human-made (e.g., vehicular collisions and explosive blasts) hazards [1–3]. It has been reported that the UK spends over 15 billion pounds per year on maintenance and this amount is continuously increasing each year [4]. Civil infrastructure maintenance is prioritised in the UK government report of the 2016-2021 national infrastructure delivery plan [5].

In order to conduct maintenance work on civil infrastructure, a structural in-service health diagnosis and serviceability inspection is normally required initially, which can be considered as one of the objectives of a broader topic commonly called ‘structural health monitoring’ (SHM) [6–8]. SHM helps operators understand the structural condition in real-time and make decisions for the planning of maintenance work. In SHM, a field dynamic test is often required to measure structural vibration response, where the response data is used to extract structural dynamic characteristics [9–11].

Considering practical constraints (e.g., availability, budget), it is common in dynamic tests that the number of DOFs (degrees of freedom) to be measured is larger than the number of available sensors. Under this situation, a multiple-setup strategy can be employed, which entails moving (or 'roving') some of the sensors to different locations in different setups, while other sensors remain in the same locations and serve as references during the test [12,13]. The multiple-setup strategy is especially effective in facilitating the dynamic testing of large civil infrastructure, such as supertall buildings and long-span bridges [14–17].

Modal identification aims at identifying structural modal properties (e.g., natural frequencies, damping ratios and mode shapes) using measured vibration data [18]. Natural frequency is associated with structural resonance. The structure dynamic response is amplified when the frequency of excitation is close to the natural frequency. One of the targets in the design or maintenance of civil infrastructure against dynamic loads (e.g., wind, earthquake, human-induced excitation) is to properly accounting for resonance effect [19–21]. The damping ratio depends on structural vibration level and is a reflection of energy dissipation. It has a crucial effect on the magnitude of structural response [22,23]. Mode shape reflects the distribution patterns of the structure associated with mass and stiffness. The change in mode shape may also help identify potential structural damage [24–26].

Modal identification is often one of the first few steps in SHM to provide information about in-service dynamic performance. Ambient modal identification, also known as 'operational modal analysis' (OMA) [27,28], aims at identifying structural modal properties using 'output-only' ambient vibration response data, where the data is measured when the structure is under its normal working condition. OMA does not

require artificial loading to be applied to the structure, and so large equipment (e.g., shakers) is not necessary in ambient vibration tests. This greatly facilitates application to civil infrastructures. Since ambient excitation is not measured, the identification uncertainty of modal parameters becomes significant. It is therefore necessary to have a quantitative assessment of the uncertainty and quality control of the identified modal properties. Since different test configurations can yield potentially different levels of uncertainty, it is also of interest to know how the uncertainty is related to test configuration.

1.2 Literature review

This section presents a review of the literature relevant to the thesis topic. A review of OMA techniques is first presented, followed by a review of multiple-setup modal identification. The identification uncertainty of OMA is then reviewed, where both uncertainty quantification and management are addressed. Finally, dynamic test planning is reviewed.

1.2.1 OMA techniques

OMA techniques have been under development for decades. There are methods that can handle a variety of situations, such as well-separated modes, close modes, single setup data and multiple-setup data. Methods can generally be classified as Bayesian and non-Bayesian, based on their philosophies.

1.2.1.1 Non-Bayesian methods

Regardless of whether it is Bayesian or not, a method can be classified as time domain or frequency domain depending on the way it models or operates the data for identification.

Time domain

The natural excitation technique (NExT) [29] is a conventional time domain method initially developed for analysing 'input-output' data. It was then extended to OMA by treating the correlation function of the random response under natural excitation as a sum of decaying sinusoids. Most NExT-type methods can incorporate the random decrement (RD) technique, where the system response is treated as a random decrement function and is proportional to the correlation function [30]. The RD technique was first proposed by Cole in the late 1960s [31]. It computes from the measured response an artificial free vibration response by averaging a sufficiently large number of vibration responses with initial conditions of the same sign. The NExT-type methods that incorporate the RD technique include the Ibrahim time domain method [32], the least square complex estimation [33], the poly-reference time domain method [34] and the eigensystem realization algorithm (ERA) [35]. The NExT-type methods were developed during the early stages of OMA development and have been enhanced to deal with close modes and spurious harmonics [27].

The auto-regressive moving average (ARMA) model and the vector-ARMA model are general models for linear time-invariant systems, which can also be used for modal identification [36–41]. The prediction error method [39] utilises the ARMA model to estimate modal parameters by minimising the estimation error, which results in a high nonlinear optimisation problem. Later, a vector ARMA model based prediction error method was developed [40]. The ARMA model was also applied in state-space to improve identification efficiency and convergence rate [42]. However, due to the issues in computational efficiency and convergence capability, the application of the ARMA-type methods is limited [43].

Stochastic subspace identification (SSI) [44] employs a discrete-time stochastic state-space model to estimate modal parameters from an observed output correlation sequence. Since the physical modes extracted from data cannot be directly separated from noise, a stabilisation diagram is normally used to further distinguish the structural physical modes from spurious ones [45]. Two main types of SSI, namely covariance-driven SSI [46] and data-driven SSI [44], have been developed. The covariance-driven SSI addresses the so-called stochastic realisation problem, which is similar to the ERA modal identification. Data-driven SSI takes the identification of the state sequence prior to the estimation of the state-space matrices. By using linear algebra techniques, the state-space matrices can be identified directly from the raw data. The SSI-type modal identification methods provide a robust and efficient way of estimating structural modal parameters. They have been widely used in OMA applications [47–49].

Frequency domain

Frequency domain methods operate in a transformed space (often frequency) of the data, effectively making use of the information on the resonance band of modes for modal identification. In the frequency domain, the spectral density function is exploited to extract modal parameters [27]. Peak picking (PP) [50–52] is one of the simplest frequency domain methods. It utilises the fact that a structure subjected to ambient excitation has large response at its natural frequencies, i.e., resonances. The natural frequencies are then simply picked up from the peaks in the power spectra density (PSD). The accuracy of the estimated modal parameters depends on the frequency resolution of the spectra. Since mode shape information is directly extracted from matrix decomposition of the PSD matrix, the method need not give the actual

mode shape for close modes. The eigenvector is generally called 'operational defection shape'. Damping is often estimated using the half-power bandwidth technique, which is found to be inaccurate [28]. Based on the PP method, a frequency domain decomposition (FDD) method [53] was developed, which overcomes the limitations of the PP method. FDD uses singular value decomposition to decompose the PSD matrix in order to obtain natural frequencies and mode shapes. Later, an enhanced FDD method [54] was developed to additionally identify damping ratios. A frequency-spatial domain decomposition method was also developed based on FDD, which improved identification precision by utilising an enhanced PSD [55].

1.2.1.2 Bayesian methods

Bayesian methods [56–58] constitute another school of thought. It models the modal properties as random variables, whose probability distribution depends on the given data and modelling assumptions. From a Bayesian point of view, the identification results are encapsulated in the 'posterior' (i.e., given data) probability distribution of parameters. This posterior distribution is a joint probability density function (PDF) conditional on modelling assumptions and given data [59]. In modal identification, the 'prior' information is typically negligible compared to the information provided by the data. The posterior distribution is then proportional to the likelihood function, which describes the distribution of data with given modal properties. In OMA, the likelihood function depends in a nonlinear manner on the modal properties. With sufficiently long data, the posterior distribution has a centralised shape but it does not belong to any standard distribution [56]. The posterior PDF can be approximated using a Gaussian distribution, which is characterised by the posterior 'most probable value' (MPV) of modal properties and the posterior covariance matrix [60]. Determining the

MPV involves solving an optimisation problem with respect to (w.r.t.) the modal parameters. Determining the posterior covariance matrix requires calculating the inverse of the Hessian of the negative log-likelihood function (NLLF) at the MPV.

Formulating the likelihood function in Bayesian OMA is a fundamental element for modal identification. Formulations have been derived based on different data types, including time domain data [57], sample PSD [61] and Fast Fourier Transform (FFT) of data [62]. Comparing these formulations, the FFT formulation has fairly robust modelling assumptions and is mathematically tractable [60]. Based on the FFT of ambient vibration data, fast computational algorithms have been developed for different situations, including well-separated modes [63], close modes [64], multiple-setup data [65] and asynchronised data [66]. Field test applications of Bayesian FFT modal identification can be found in [14,67–69].

1.2.2 Multiple-setup modal identification

In dynamic tests, it is desirable to measure a large number of DOFs to capture as much structural information as possible. To cover all DOFs with a single setup, it requires at least the same number of sensors as the number of measured locations, which is not economical and may create other concerns such as logistics. Considering practical constraints (e.g., budget) and the availability of sensors, a multiple-setup strategy [13,70] is commonly employed to measure a large number of DOFs with a limited number of sensors. In multiple setups, some of the sensors are kept in the same location during the test (i.e., reference sensors), while the remaining sensors are moved progressively to different locations in different setups until all the locations of interest are covered (i.e., roving sensors).

Modal identification using multiple-setup data requires more efforts in processing data compared to that using single setup data. The multiple-setup data from different setups cannot be directly merged together since the excitations in different setups are different [13]. Conventionally, the modal parameters are identified individually for each setup. The 'representative' natural frequencies and damping ratios can be taken as the average values from different setups. The global mode shapes need to be assembled from the partial ones identified from individual setups. This way of processing multiple-setup data is referred as the post-separate estimation re-scaling (PoSER) strategy [13,70]. Assembling the global mode shape can be done by using least-square or more advanced techniques, such as the expectation maximisation algorithm [71] or the global least square method [72]. A comparison of the modal identification using multiple-setup data and simultaneous measurement data can be found in [73].

Besides the conventional PoSER approach, a post-identification strategy was developed. This strategy merges the multiple-setup data into a single set and hence the modal identification only needs to be performed once. A strategy of re-scaling and merging data from different setups was first proposed for modal identification using the SSI method [70]. Pre-global estimation re-scaling (PreGER) and post global estimation re-scaling (PoGER) strategies are then introduced to handle multiple-setup data [74]. These two strategies follow the procedure of merging-identification-normalisation and normalisation-merging-identification, respectively. A reference-based covariance-driven SSI using PreGER and PoGER for modal identification was proposed in [13]. The applications of different merging strategies can be found in [75,76].

Apart from the above 'multi-step' strategies for processing multiple-setup data, modal identification methods directly incorporating multiple-setup data have been developed. A SSI based method was developed to manage multiple-setup data with a joint state-space model [76]. The modal parameters of the state-space model are estimated using a maximum likelihood estimation with an expectation maximisation algorithm. A Bayesian approach was also developed to incorporate multiple-setup data for modal identification. The modal properties including global mode shapes are obtained from a fast iterative algorithm [65].

1.2.3 Identification uncertainty

Due to the absence of input loading information, identification uncertainty in OMA can be significant. The impact of uncertainty on identified modal parameters has been studied [77,78], where the uncertainty is classified into two types, aleatory and epistemic. Aleatory uncertainty refers to the inherent variation of the physical structure, which reveals the variability aspect of nature and is irreducible. Epistemic uncertainty is primarily caused by a lack of data information, measurement noise and modelling errors [79]. In this section, a review of uncertainty quantification and management is presented.

1.2.3.1 Uncertainty quantification

Uncertainty quantification can differ between the classical statistics ('frequentist') and the Bayesian approach. In a frequentist approach, uncertainty quantification refers to obtaining the ensemble variance of the estimates through hypothetical repeated experiments [80–82]. Quantifying the uncertainty requires calculating the variance of the modal property estimates, which is the expectation of the squared deviation from the mean. The random data is modelled as arising from some 'unknown true' modal

parameters. Quantification techniques have been developed for different modal identification methods. A variance estimation procedure was proposed that uses the first-order sensitivity of the modal parameters estimates to perturb the measured data [80]. The theory was applied to the reference-based covariance-driven SSI for uncertainty quantification. Later, the first-order perturbation analysis was extended to incorporate multiple-setup data using SSI modal identification [83]. In order to reduce the computational burden associated with calculating the variance in SSI, a multi-order computation strategy was proposed [84]. A method for estimating the confidence interval based on perturbation analysis was developed for the ERA modal identification [85]. An uncertainty quantification technique was also developed based on the ARMA model and the prediction error method [81]. A high-order time domain based uncertainty quantification was proposed, incorporating poly-reference time domain modal identification [86].

In Bayesian modal identification, the modal parameters are uncertain and modelled as random variables. All the information about modal parameters with given data is encapsulated in the posterior distribution. The identification uncertainty can be quantified by the posterior covariance, which can be obtained from the inverse of the Hessian matrix of the NLLF formulated with the modal parameters [87]. Based on different types of data, computational strategies for determining the posterior covariance matrix have been developed, including single setup data [63], multiple-setup data [88] and asynchronised data [89].

1.2.3.2 Uncertainty management

Uncertainty quantification offers a ‘point-wise’ view of the uncertainty for a given set of data. However, quantifying uncertainty alone does not provide much insight for the

control of uncertainty or guiding vibration tests [60]. Uncertainty management aims at investigating what factors the uncertainty depends on and what the relationship is [90]. Due to the complication involved in describing the uncertainty associated with the modal parameters, it is unlikely that one can express the uncertainty exactly in a simple expression [91]. A study has shown that, for sufficiently long data, the leading order of the posterior covariance can be expressed in a closed form [92]. Focusing on well-separated modes with single setup data, closed-form expressions of the posterior c.o.v. (coefficient of variation = standard derivation / mean) of the modal parameters were developed [91]. The results of the posterior c.o.v. were collectively referred as 'uncertainty law', which provides explicit expressions for the uncertainty of the modal parameters w.r.t. test configuration [90,92]. The original uncertainty law [91] was developed in 'zeroth order', where the signal-to-noise (s/n) ratio effect did not appear in the formula. It was later extended to account for the s/n ratio in a 'first order law' [90]. The uncertainty law allows test configurations to be planned from an uncertainty point of view. Implementation in designing field tests can be found in [14,15,93].

In the development of uncertainty law, it was found that when the data is modelled to have a distribution as the likelihood function (i.e., no modelling error), the posterior covariance matrix is asymptotically equal to a deterministic quantity that depends on the 'information content' of data [92]. For sufficiently long data, the posterior covariance matrix is asymptotically equal to the inverse of the Fisher Information Matrix (FIM). This naturally coincides with the tightest Cramér-Rao bound (CRB) in classical statistics for any unbiased estimator [94]. This fact can be used to simplify the derivation of the uncertainty law. Asymptotics and stochastic ordering of terms in the likelihood function from first principles can be bypassed. This allows the

uncertainty law for other unexplored cases (e.g., close modes and multiple setups) to be derived in a systematic manner.

1.2.4 Dynamic test planning

The planning of dynamic test is important to the quality of identified structural dynamic characteristics [9,95]. Dynamic test planning primarily includes the planning of sensor location, quantity and quality [15,96]. For multiple setups, it also includes the allocation of different sensors (i.e., reference and roving sensors) in different setups [97,98]. Sensor location planning is also known as sensor placement. The objective is to find the good or optimal location of sensors, so that the measured data is most informative in providing desired information about the subject structure [96,99]. Among existing techniques, information theory based [100–102] optimal sensor placement approach has received considerable attention. The effective independence method is first proposed, which aims at maximising the determinant of the Fisher Information Matrix of the estimated parameters [103]. Similar methods that maximise some norm (e.g., determinant, trace) of the FIM can be found in [102,104,105]. Under the Bayesian framework, an optimisation strategy was proposed to minimise the information entropy [106]. It shows that, for sufficiently long data, minimising the information entropy is asymptotically equivalent to maximising the determinant of the FIM [107]. In addition, maximum expected utility theory and a Bayesian linear model can also be used for optimal sensor placement [108]. A Bayesian optimal sensor strategy was proposed to maximise the expected utility function, taken as the Kullback–Leibler divergence between the prior and posterior distribution [109]. The information theory based techniques have been applied to the dynamic testing of civil structures, such as bridges [110–112] and buildings [113–115].

There are also optimal sensor placement techniques based on modal kinetic energy [96,116], modal reduction [117], and observability [118].

The planning of multiple setups requires the allocation of reference sensors and roving sensors in different setups. However, multiple-setup planning is still an open problem. Most existing planning works are based on the operator's knowledge and experience [14,49]. Optimisation criteria for reference sensors were introduced in [97], where the optimality is defined as using as few references as possible and placing the reference sensors away from the nodal location of the mode shapes of interest. A strategy for optimising reference locations was proposed using predicted power spectral amplitudes and initial finite element models [119]. The performance depends on the accuracy of the finite element model and experimentally obtained modal parameters. An information entropy based optimisation strategy was proposed for multiple setups [98]. The objective of the strategy is to optimise the worst setup and hence to make all setups good.

1.3 Objectives and outline of this work

OMA has received considerable attention in field testing of civil engineering structures. The multiple-setup strategy is widely employed in full-scale dynamic tests due to its economy in implementation. Due to the absence of input loading information, the identification uncertainty of modal parameters becomes significant and is crucial to identification results. Being able to quantify uncertainty becomes important in OMA. Moreover, different test configurations can yield different levels of uncertainty. It is necessary to investigate how the uncertainty is related to the test configuration. This is especially important for multiple setups, since it involves additional deployment of different sensors, which can be complicated. For planning purposes, it

is also desirable to have an uncertainty-based test configuration assessment. Motivated by the above concerns, this thesis contributes to quantifying and managing identification uncertainty in operational modal analysis with multiple setups.

Based on Bayesian modal identification framework, uncertainty quantification is addressed by investigating the computation of the posterior covariance matrix as the inverse of the Hessian of NLLF of modal parameters. Difficulties arise in deriving the Hessian matrix, since modal parameters are subjected to constraints. In order to properly handle the constraints in a systematic manner, a theoretical framework is proposed for deriving the Hessian of a function subjected to constraints. This is developed for system identification in general. The proposed theory is applied to Bayesian modal identification with single setup and multiple-setup data, where new analytical expressions for calculating the posterior covariance matrix are derived. Synthetic data examples are used to validate the proposed theory.

The uncertainty management of multiple setups is addressed by investigating the leading order behaviour of the posterior covariance matrix. With sufficient data, it is possible to express the posterior covariance matrix via the inverse of the FIM. Small damping and high modal s/n ratio leads to a closed-form expression of the FIM. Considering asymptotic decoupling of modal parameters, the dimension of the FIM is reduced. This subsequently yields closed-form expressions of the leading order posterior c.o.v. of the modal parameters as the target uncertainty law. The uncertainty law is applied to multiple-setup ambient vibration test of an office building and a suspension footbridge, where test configurations are quantitatively assessed from an uncertainty point of view.

This thesis is outlined as follow:

Chapter 2 presents a theoretical framework for deriving the Hessian of a function subjected to constraints. The theory is applicable for Bayesian system identification with globally identifiable models in general, where the posterior covariance matrix is derived from the inverse of the Hessian of a function related to the likelihood function. Two formulae are developed to handle constraints in a systematic manner.

Chapter 3 presents uncertainty quantification in Bayesian modal identification with single setup and multiple-setup data. The posterior covariance matrix is evaluated using the theory proposed in Chapter 2, where the constraints arise from mode shape scaling. The newly developed formulae for calculating the posterior covariance are validated with synthetic data. Computational efficiency is also discussed.

Chapter 4 presents uncertainty management in multiple-setup OMA, where the leading order behaviour of the posterior covariance matrix is investigated. The asymptotic posterior c.o.v.s of the modal parameters are derived and written in closed-form expressions. A parametric study with regard to mode shape c.o.v. is conducted to generate insights for the planning of multiple setups. The proposed theory is validated using synthetic, laboratory and field test data.

Chapter 5 presents full-scale dynamic tests on an eight-storey office building and a suspension footbridge. Preparation work for the field test is presented, followed by multiple-setup planning. The field test data is analysed using a Bayesian modal identification capable of incorporating information from multiple setups. The test configurations are quantitatively assessed using the theory developed in Chapter 4.

Chapter 6 concludes the thesis and provides suggestions for future research.

Chapter 2 Hessian with constraints in system identification

2.1 Introduction

System identification aims at identifying the mathematical model parameters of a real system from given data. It is relevant to many disciplines, such as structural dynamics in civil and mechanical engineering [120–124]. Structural system identification commonly considers modal identification as its first step, where the modal identification results are used for making inference about structural model parameters (e.g., stiffness, mass). Bayesian system identification provides a rigorous way to identify system model parameters as well as to fundamentally quantify their uncertainties [125–127]. In this approach, the identification results are encapsulated in the posterior PDF of model parameters. Let $\boldsymbol{\theta}$ denote the parameters to be identified and D be the measured data. Applying Bayes' Theorem, the posterior PDF of $\boldsymbol{\theta}$ given data D can be expressed as

$$p(\boldsymbol{\theta}|D) = p(\boldsymbol{\theta})\, p(D|\boldsymbol{\theta})\, p(D)^{-1} \tag{1}$$

where $p(\boldsymbol{\theta})$ is the 'prior' distribution reflecting one's knowledge in the absence of data; $p(D)$ is a normalising constant that is immaterial to the distribution of $\boldsymbol{\theta}$; $p(D|\boldsymbol{\theta})$ is the 'likelihood function' of D given $\boldsymbol{\theta}$. For convenience in analysis and computation, the posterior PDF $p(\boldsymbol{\theta}|D)$ is often written as

$$p(\boldsymbol{\theta}|D) \propto e^{-L(\boldsymbol{\theta})} \tag{2}$$

where $L(\boldsymbol{\theta}) = -\ln[p(D|\boldsymbol{\theta})p(\boldsymbol{\theta})]$ is called the 'negative logarithm function' (NL) in this work.

For 'globally identifiable problems', the posterior PDF has a unique maximum in the interior of the parameter space, called the posterior MPV, say $\hat{\boldsymbol{\theta}}$, where the NL function is minimised [128]. A second order expansion of $L(\boldsymbol{\theta})$ w.r.t. $\hat{\boldsymbol{\theta}}$ leads to a Gaussian approximation of the posterior PDF, where the mean value is equal to $\hat{\boldsymbol{\theta}}$ and the covariance matrix $\hat{\mathbf{C}}$ is equal to the inverse of the Hessian of $L(\boldsymbol{\theta})$ at MPV, i.e.,

$$\hat{\mathbf{C}} = (\nabla^2_{\boldsymbol{\theta}}\hat{L})^{-1} \tag{3}$$

Depending on how the identification problem is formulated, some of the model parameters may be subjected to constraints. For example, in structural modal identification, mode shapes are commonly subjected to norm constraints; in a state-space model, the covariance matrices for noise are subjected to symmetry constraints. For determining the MPV, the constraints can be handled by parameterisation or using Lagrange multipliers. For determining the posterior covariance matrix, simply taking the Hessian of the NL function w.r.t. original parameters leads to incorrect results. One way of handling the constraints is to have a set of 'free parameters' mapping the constrained model parameters, so that the constraints are always satisfied. Due to the composite action of the NL function and the mapping function, the expressions for the Hessian and further posterior covariance matrix become complicated. This may also create a burden in computation and programming.

Motivated by the above concerns, this chapter presents a systematic way of deriving the posterior covariance matrix in Bayesian system identification capable of incorporating constraints. A theoretical framework is proposed for deriving the Hessian of a function subjected to constraints. Two formulae are developed. One is applicable for general parameter values, while the other is only applicable at the MPV but its expression is more compact. This chapter develops the theory with mathematical proofs. In the next chapter, the proposed framework will be applied to uncertainty calculation in Bayesian modal identification for single setup and multiple-setup data, followed by validation with numerical examples.

2.2 Transforming variables for covariance matrix

In order to derive the posterior covariance matrix from the inverse of the Hessian with constrained model parameters, one way is to map the constrained parameters by a set of free parameters, so that the constraints are always satisfied. Let $\boldsymbol{\theta} = [\theta_1, ..., \theta_{n_\theta}]^T$ denote a set of parameters subjected to n_c independent constraints, which can be written as

$$G_i(\boldsymbol{\theta}) = 0 \qquad (\text{i}=1,...,\text{n}_c) \tag{4}$$

Define $\mathbf{v}_c(\mathbf{u}) : R^p \mapsto R^{n_\theta}$ as a function that maps free parameter $\mathbf{u}$ to $\boldsymbol{\theta}$, where $\mathbf{u} = [u_1, ..., u_p]^T$, so that it always satisfies the constraints, i.e.,

$$G_i(\mathbf{v}_c(\mathbf{u})) = 0 \qquad (\text{i}=1,...,\text{n}_c) \quad \text{for any } \mathbf{u} \tag{5}$$

Note that the dimension of $\mathbf{u}$ should not be less than the dimension of admissible space since $\boldsymbol{\theta}$ is subjected to n_c constraints, i.e., $p \geq n_\theta - n_c$.

Let $L(\boldsymbol{\theta})$ be the NL function in the Bayesian system identification problem that is formulated in terms of $\boldsymbol{\theta}$. When the problem is formulated in terms of the free parameter $\mathbf{u}$ with the mapping function $\mathbf{v}_c(\mathbf{u})$, the NL function can be written as

$$L_c(\mathbf{u}) = L\left(\mathbf{v}_c(\mathbf{u})\right) \tag{6}$$

Note that the MPV of $\mathbf{u}$ and $\boldsymbol{\theta}$ are related by $\hat{\boldsymbol{\theta}} = \mathbf{v}_c(\hat{\mathbf{u}})$, where the hat '^' denotes the MPV. Within a Gaussian approximation of the posterior PDF of $\mathbf{u}$, its posterior covariance matrix is given by the inverse of the Hessian of $L_c(\mathbf{u})$ evaluated at $\hat{\mathbf{u}}$. By transforming variables through $\boldsymbol{\theta} = \mathbf{v}_c(\mathbf{u})$, the posterior covariance of $\boldsymbol{\theta}$ can be obtained.

Let $\Delta\boldsymbol{\theta}$ and $\Delta\mathbf{u}$ be uncertain variations in $\boldsymbol{\theta}$ and $\mathbf{u}$ from their MPV, respectively. To the first order of $\Delta\boldsymbol{\theta}$

$$\Delta\boldsymbol{\theta} = \sum_{i=1}^{p} \frac{\partial \hat{\mathbf{v}}_c}{\partial u_i} \Delta u_i = \left[\frac{\partial \hat{\mathbf{v}}_c}{\partial u_1} \quad \cdots \quad \frac{\partial \hat{\mathbf{v}}_c}{\partial u_p} \right] \begin{bmatrix} \Delta u_1 \\ \vdots \\ \Delta u_p \end{bmatrix} = \nabla_{\mathbf{u}} \hat{\mathbf{v}}_c \Delta\mathbf{u} \tag{7}$$

where $\nabla_{\mathbf{u}} \hat{\mathbf{v}}_c$ is the gradient of $\mathbf{v}_c(\mathbf{u})$ evaluated at the MPV. The posterior covariance of $\boldsymbol{\theta}$ is then given by

$$\hat{\mathbf{C}}(\boldsymbol{\theta}) = E[\Delta\boldsymbol{\theta}\Delta\boldsymbol{\theta}^T \mid D] = (\nabla_{\mathbf{u}} \hat{\mathbf{v}}_c) E[\Delta\mathbf{u}\Delta\mathbf{u}^T \mid D] (\nabla_{\mathbf{u}} \hat{\mathbf{v}}_c)^T = (\nabla_{\mathbf{u}} \hat{\mathbf{v}}_c) \hat{\mathbf{C}}_{\mathbf{u}} (\nabla_{\mathbf{u}} \hat{\mathbf{v}}_c)^T \tag{8}$$

where $\hat{\mathbf{C}}_{\mathbf{u}}$ is the posterior covariance of $\mathbf{u}$ at the MPV, which is equal to the inverse of the Hessian of $\hat{L}_c(\mathbf{u})$. Note that this Hessian only has a rank of $n_\theta - n_c$, and so it is singular when $p > n_\theta - n_c$. However, this singularity is immaterial to the posterior uncertainty of $\boldsymbol{\theta}$, since the variations of $\boldsymbol{\theta}$ are orthogonal to the singular directions.

Due to this singularity, the inverse of the Hessian should be taken as a 'pseudo-inverse'. The matrix $\hat{\mathbf{C}}(\boldsymbol{\theta})$ is then given by

$$\hat{\mathbf{C}}(\boldsymbol{\theta}) = (\nabla_{\mathbf{u}} \hat{\mathbf{v}}_c)\left[\nabla^2_{\mathbf{u}} \hat{L}_c\right]^{+} (\nabla_{\mathbf{u}} \hat{\mathbf{v}}_c)^T \tag{9}$$

where ' + ' denotes the pseudo-inverse, which is obtained through eigenvector representation ignoring the components that correspond to the zero eigenvalues.

2.3 Constrained Hessian formulae

Obtaining $\hat{\mathbf{C}}(\boldsymbol{\theta})$ requires deriving the Hessian of $L_c(\mathbf{u})$, which can be complicated since $L_c(\mathbf{u}) = L\left(\mathbf{v}_c(\mathbf{u})\right)$ is a composite function of $\mathbf{u}$. This section outlines the key theoretical results, where two formulae are derived for the Hessian of $L_c(\mathbf{u})$. Their mathematical proofs are provided in the next section.

For a general $\mathbf{u}$, it can be shown that $\nabla^2_{\mathbf{u}} L_c(\mathbf{u})$ can be expressed in terms of the gradient and Hessian of $L(\boldsymbol{\theta})$ and $\mathbf{v}_c(\mathbf{u})$. That is

$$\nabla^2_{\mathbf{u}} L_c = (\nabla_{\mathbf{u}} \mathbf{v}_c)^T (\nabla^2_{\boldsymbol{\theta}} L)(\nabla_{\mathbf{u}} \mathbf{v}_c) + (\mathbf{I}_p \otimes \nabla_{\boldsymbol{\theta}} L)\nabla^2_{\mathbf{u}} \mathbf{v}_c \tag{10}$$

where ' $\otimes$ ' denotes the Kronecker product; $\mathbf{I}_p$ is the $p \times p$ identity matrix;

The gradient and the Hessian of $\nabla_{\mathbf{u}} \mathbf{v}_c$ are given by

$$\nabla_{\mathbf{u}} \mathbf{v}_c = \left[\frac{\partial \mathbf{v}_c}{\partial u_1} \quad \cdots \quad \frac{\partial \mathbf{v}_c}{\partial u_p}\right] \tag{11}$$

$$\nabla^2_{\mathbf{u}}\mathbf{v}_c = \begin{bmatrix} \dfrac{\partial^2 \mathbf{v}_c}{\partial u_1^2} & \dfrac{\partial^2 \mathbf{v}_c}{\partial u_1 \partial u_2} & \cdots & \dfrac{\partial^2 \mathbf{v}_c}{\partial u_1 \partial u_p} \\ & \ddots & & \dfrac{\partial^2 \mathbf{v}_c}{\partial u_2 \partial u_p} \\ & & & \vdots \\ \text{Block sym.} & & & \dfrac{\partial^2 \mathbf{v}_c}{\partial u_p^2} \end{bmatrix} \tag{12}$$

Equation (10) is called the 'direct formula' in this work, which is applicable for any $\mathbf{u}$. Due to the Kronecker product, this formula requires multiplying large matrices which are sparse. Deriving $\nabla^2_{\mathbf{u}}\mathbf{v}_c \in R^{p^2 \times p}$ also involves operating with a large number of second derivatives. The direct formula does not consider the fact that constraints $G_i\left(\mathbf{v}_c(\mathbf{u})\right) = 0$ for $i = 1,...,n_c$ are always satisfied. Taking this fact into account and using the Lagrange multiplier, it can be shown that the constrained Hessian of $L_c(\mathbf{u})$ at the MPV can be simplified to

$$\nabla^2_{\mathbf{u}}\hat{L}_c = (\nabla_{\mathbf{u}}\hat{\mathbf{v}}_c)^T \left[\nabla^2_{\boldsymbol{\theta}}\hat{L} + \sum_{i=1}^{n_c} \hat{\lambda}_i \nabla^2_{\boldsymbol{\theta}}\hat{G}_i \right] \nabla_{\mathbf{u}}\hat{\mathbf{v}}_c \tag{13}$$

where the hat '^' denotes the quantity evaluated at the MPV; $\{\hat{\lambda}_i\}_{i=1}^{n_c}$ are Lagrange multipliers;

$$\hat{\boldsymbol{\lambda}} = \begin{bmatrix} \hat{\lambda}_1 \\ \vdots \\ \hat{\lambda}_{n_c} \end{bmatrix} = -\frac{\nabla_{\boldsymbol{\theta}}\hat{\mathbf{G}}(\nabla_{\boldsymbol{\theta}}\hat{L})^T}{\nabla_{\boldsymbol{\theta}}\hat{\mathbf{G}}(\nabla_{\boldsymbol{\theta}}\hat{\mathbf{G}})^T} \tag{14}$$

Equation (13) is referred as the 'Lagrange formula', which is only applicable at the MPV. The expression does not involve the Kronecker product or the second derivative of the mapping function.

The two proposed formulae can be used for deriving the Hessian of a function subjected to constraints in Bayesian system identification, and both of them are expressed in a systemic manner. The direct formula is applicable for any parameter value. The Lagrange formula is only applicable at MPV, but the expression is more compact compared to the former formula. The next section provides the mathematical proofs of these two formulae.

2.4 Mathematical proofs

2.4.1 Direct formula

To prove the direct formula (10), we first derive the gradient of $L(\mathbf{u})$, when $\mathbf{u}$ is mapped through $\mathbf{v}_c(\mathbf{u})$. Denote $\mathbf{v}_c(\mathbf{u})$ as a vector of $[v_1(\mathbf{u}),...,v_{n_\theta}(\mathbf{u})]^T$. For $i=1,...,p$, differentiating $L_c(\mathbf{u})$ w.r.t. u_i gives

$$\frac{\partial L_c}{\partial u_i}=\sum_{j=1}^{n_\theta}\frac{\partial L}{\partial v_j}\frac{\partial v_j}{\partial u_i}=\left[\frac{\partial L}{\partial v_1}\quad\cdots\quad\frac{\partial L}{\partial v_{n_\theta}}\right]\left[\frac{\partial v_1}{\partial u_i}\quad\cdots\quad\frac{\partial v_{n_\theta}}{\partial u_i}\right]^T=\nabla_{\boldsymbol{\theta}}L\frac{\partial \mathbf{v}_c}{\partial u_i} \tag{15}$$

Assembling all the u_i for $i=1,...,p$ row-wise gives

$$\nabla_{\mathbf{u}}L_c=\left[\frac{\partial L_c}{\partial u_1}\quad\cdots\quad\frac{\partial L_c}{\partial u_p}\right]=\left[\nabla_{\boldsymbol{\theta}}L\frac{\partial \mathbf{v}_c}{\partial u_1}\quad\cdots\quad\nabla_{\boldsymbol{\theta}}L\frac{\partial \mathbf{v}_c}{\partial u_p}\right]=\nabla_{\boldsymbol{\theta}}L\nabla_{\mathbf{u}}\mathbf{v}_c \tag{16}$$

Further differentiating the gradient of $L_c(\mathbf{u})$ w.r.t. u_i using chain rule gives

$$\frac{\partial \nabla_{\mathbf{u}}L_c}{\partial u_i}=\frac{\partial \nabla_{\boldsymbol{\theta}}L}{\partial u_i}\nabla_{\mathbf{u}}\mathbf{v}_c+\nabla_{\boldsymbol{\theta}}L\frac{\partial \nabla_{\mathbf{u}}\mathbf{v}_c}{\partial u_i} \tag{17}$$

For the first term on RHS of (17), it can be shown that

$$\begin{aligned}\frac{\partial \nabla_{\boldsymbol{\theta}} L}{\partial u_i} \nabla_{\mathbf{u}} \mathbf{v}_c &= \frac{\partial}{\partial u_i}\left[\frac{\partial L}{\partial v_1},...,\frac{\partial L}{\partial v_{n_\theta}}\right]\nabla_{\mathbf{u}} \mathbf{v}_c \\ &= \sum_{j=1}^{n_\theta}\frac{\partial v_j}{\partial u_i}\left[\frac{\partial^2 L}{\partial v_j \partial v_1},...,\frac{\partial^2 L}{\partial v_j \partial v_{n_\theta}}\right]\nabla_{\mathbf{u}} \mathbf{v}_c \\ &= \left[\frac{\partial v_1}{\partial u_i},...,\frac{\partial v_{n_\theta}}{\partial u_i}\right]\left[\nabla^2_{\boldsymbol{\theta}} L\right]\nabla_{\mathbf{u}} \mathbf{v}_c \\ &= (\frac{\partial \mathbf{v}_c}{\partial u_i})^T\left[\nabla^2_{\boldsymbol{\theta}} L\right]\nabla_{\mathbf{u}} \mathbf{v}_c\end{aligned} \tag{18}$$

Assembling all the u_i for $i = 1,..., p$ column-wise gives

$$\begin{aligned}\begin{bmatrix}\frac{\partial \nabla_{\boldsymbol{\theta}} L}{\partial u_1}\nabla_{\mathbf{u}} \mathbf{v}_c \\ \vdots \\ \frac{\partial \nabla_{\boldsymbol{\theta}} L}{\partial u_p}\nabla_{\mathbf{u}} \mathbf{v}_c\end{bmatrix} &= \begin{bmatrix}(\frac{\partial \mathbf{v}_c}{\partial u_1})^T(\nabla^2_{\boldsymbol{\theta}} L)\nabla_{\mathbf{u}} \mathbf{v}_c \\ \vdots \\ (\frac{\partial \mathbf{v}_c}{\partial u_p})^T(\nabla^2_{\boldsymbol{\theta}} L)\nabla_{\mathbf{u}} \mathbf{v}_c\end{bmatrix} \\ &= \begin{bmatrix}(\frac{\partial \mathbf{v}_c}{\partial u_1})^T \\ \vdots \\ (\frac{\partial \mathbf{v}_c}{\partial u_p})^T\end{bmatrix}\left[\nabla^2_{\boldsymbol{\theta}} L\right]\nabla_{\mathbf{u}} \mathbf{v}_c = (\nabla_{\mathbf{u}} \mathbf{v}_c)^T\left[\nabla^2_{\boldsymbol{\theta}} L\right]\nabla_{\mathbf{u}} \mathbf{v}_c\end{aligned} \tag{19}$$

For the second term on RHS of (17),

$$\nabla_{\boldsymbol{\theta}} L \frac{\partial \nabla_{\mathbf{u}} \mathbf{v}_c}{\partial u_i} = \nabla_{\boldsymbol{\theta}} L\left[\frac{\partial^2 \mathbf{v}_c}{\partial u_i \partial u_1},...,\frac{\partial^2 \mathbf{v}_c}{\partial u_i \partial u_p}\right] \tag{20}$$

Assembling all the u_i for $i = 1,..., p$ column-wise gives

$$\begin{bmatrix} \nabla_{\boldsymbol{\theta}} L \dfrac{\partial \nabla_{\mathbf{u}} \mathbf{v}_c}{\partial u_1} \\ \vdots \\ \nabla_{\boldsymbol{\theta}} L \dfrac{\partial \nabla_{\mathbf{u}} \mathbf{v}_c}{\partial u_p} \end{bmatrix} = \begin{bmatrix} \nabla_{\boldsymbol{\theta}} L & & \\ & \ddots & \\ & & \nabla_{\boldsymbol{\theta}} L \end{bmatrix} \begin{bmatrix} \dfrac{\partial \nabla_{\mathbf{u}} \mathbf{v}_c}{\partial u_1} \\ \vdots \\ \dfrac{\partial \nabla_{\mathbf{u}} \mathbf{v}_c}{\partial u_p} \end{bmatrix}$$

$$= (\mathbf{I}_p \otimes \nabla_{\boldsymbol{\theta}} L) \begin{bmatrix} \dfrac{\partial_{\mathbf{u}}^2 \mathbf{v}_c}{\partial u_i \partial u_1}, \ldots, \dfrac{\partial_{\mathbf{u}}^2 \mathbf{v}_c}{\partial u_i \partial u_p} \\ \vdots \\ \dfrac{\partial^2 \mathbf{v}_c}{\partial u_i \partial u_1}, \ldots, \dfrac{\partial^2 \mathbf{v}_c}{\partial u_i \partial u_p} \end{bmatrix} = \left[\mathbf{I}_p \otimes \nabla_{\boldsymbol{\theta}} L \right] \nabla_{\mathbf{u}}^2 \mathbf{v}_c \tag{21}$$

By assembling (17) column-wise for all u_i and using the results from (19) and (21), (10) can be obtained.

2.4.2 Lagrange formula

The Lagrange formula (13) is derived from (10). To prove this, we first show that the second term on RHS of (10) is

$$(\mathbf{I}_p \otimes \nabla_{\boldsymbol{\theta}} \hat{L})(\nabla_{\mathbf{u}}^2 \hat{\mathbf{v}}_c) = (\nabla_{\mathbf{u}} \hat{\mathbf{v}}_c)^T (\sum_{i=1}^{n_c} \hat{\lambda}_i \nabla_{\boldsymbol{\theta}}^2 \hat{G}_i)(\nabla_{\mathbf{u}} \hat{\mathbf{v}}_c) \tag{22}$$

Recall that the constraints satisfy (5), i.e.,

$$G_i\left(\mathbf{v}_c(\mathbf{u})\right) = 0 \qquad \text{for any } i = 1, \ldots, n_c \tag{23}$$

Take the Hessian of (23) for $i = 1, \ldots, n_c$ w.r.t. $\mathbf{u}$ using (10), i.e., treating $G_i\left(\mathbf{v}_c(\mathbf{u})\right)$ as a composite function similar to $L_c\left(\mathbf{v}_c(\mathbf{u})\right)$. This gives

$$(\nabla_{\mathbf{u}} \hat{\mathbf{v}}_c)^T (\nabla_{\boldsymbol{\theta}}^2 \hat{G}_i)(\nabla_{\mathbf{u}} \hat{\mathbf{v}}_c) + (\mathbf{I}_p \otimes \nabla_{\boldsymbol{\theta}} \hat{G}_i)(\nabla_{\mathbf{u}}^2 \hat{\mathbf{v}}_c) = \mathbf{0} \tag{24}$$

Multiplying $\hat{\lambda}_i$ on both sides of (24) and summing over $i = 1, \ldots, n_c$ gives

$$\sum_{i=1}^{n_c}\left[\lambda_i(\mathbf{I}_p \otimes \nabla_{\boldsymbol{\theta}}\hat{G}_i)\right](\nabla^2_{\mathbf{u}}\hat{\mathbf{v}}_c) = -(\nabla_{\mathbf{u}}\hat{\mathbf{v}}_c)^T\sum_{i=1}^{n_c}(\lambda_i\nabla^2_{\boldsymbol{\theta}}\hat{G}_i)(\nabla_{\mathbf{u}}\hat{\mathbf{v}}_c) \tag{25}$$

Consider a Lagrange function w.r.t. $L(\boldsymbol{\theta})$ with constraints $\{G_i(\boldsymbol{\theta})\}_{i=1}^{n_c}$, that is

$$J(\boldsymbol{\theta},\boldsymbol{\lambda}) = L(\boldsymbol{\theta}) + \sum_{i=1}^{n_c}\lambda_i G_i(\boldsymbol{\theta}) \tag{26}$$

where $\boldsymbol{\lambda} = [\lambda_1,...,\lambda_{n_c}]^T$ is a collection of Lagrange multipliers. Supposing $\hat{\boldsymbol{\theta}}$ minimises $L(\boldsymbol{\theta})$ under constraints $G_i(\boldsymbol{\theta}) = 0$ for $i = 1,...,n_c$. Then there is a $\hat{\boldsymbol{\lambda}} = [\hat{\lambda}_1,...,\hat{\lambda}_{n_c}]^T$ such that $(\hat{\boldsymbol{\theta}},\hat{\boldsymbol{\lambda}})$ is a stationary point $J(\boldsymbol{\theta},\boldsymbol{\lambda})$, i.e.,

$$\nabla_{\boldsymbol{\theta}}J(\hat{\boldsymbol{\theta}},\hat{\boldsymbol{\lambda}}) = \nabla_{\boldsymbol{\theta}}\hat{L} + \sum_{i=1}^{n_c}\hat{\lambda}_i\nabla_{\boldsymbol{\theta}}\hat{G}_i = \mathbf{0} \tag{27}$$

where $\nabla_{\boldsymbol{\theta}}J$ stands for the gradient of J w.r.t. $\boldsymbol{\theta}$. Equation (27) can be rewritten in a matrix form, i.e.,

$$\nabla_{\boldsymbol{\theta}}\hat{L} = -\begin{bmatrix}\hat{\lambda}_1 & \cdots & \hat{\lambda}_{n_c}\end{bmatrix}\begin{bmatrix}\nabla_{\boldsymbol{\theta}}\hat{G}_1 \\ \vdots \\ \nabla_{\boldsymbol{\theta}}\hat{G}_{n_c}\end{bmatrix} = -\hat{\boldsymbol{\lambda}}^T\nabla_{\boldsymbol{\theta}}\hat{\mathbf{G}} \tag{28}$$

so that the $\hat{\lambda}_i$ can be calculated from

$$\hat{\lambda}_i = -\frac{\nabla_{\boldsymbol{\theta}}\hat{G}_i(\nabla_{\boldsymbol{\theta}}\hat{L})^T}{\nabla_{\boldsymbol{\theta}}\hat{G}_i(\nabla_{\boldsymbol{\theta}}\hat{G}_i)^T} \tag{29}$$

Take the Kronecker product of $\mathbf{I}_{n_p}$ with both sides of (27), and then right-multiply $\nabla^2_{\mathbf{u}}\hat{\mathbf{v}}_c$. It gives

$$\left[\mathbf{I}_{n_p} \otimes \nabla_{\boldsymbol{\theta}} \hat{L})\right] \nabla_{\mathbf{u}}^2 \hat{\mathbf{v}}_c = -\sum_{i=1}^{n_c} \hat{\lambda}_i \left[\mathbf{I}_{n_p} \otimes \nabla_{\boldsymbol{\theta}} \hat{G}_i\right] \nabla_{\mathbf{u}}^2 \hat{\mathbf{v}}_c \tag{30}$$

Substituting (25) into (30) gives (22), and hence (13).

2.5 Transformation invariance

In this section, we show that the formulae developed for calculating the posterior covariance matrix are invariant to the choice of constraint functions and free parameters. The invariance to the constrained functions is demonstrated by showing that the Hessian of L_c remains the same when $G_i(\boldsymbol{\theta})$ is replaced by $H_i\left(G_i(\boldsymbol{\theta})\right)$ for any scalar monotonic function $H_i(x)$ with $H_i(0) = 0$ and non-zero derivative at $x = 0$. The invariance to any free parameters is demonstrated by showing that the posterior covariance remains the same if one works with a new set of admissible free parameters.

2.5.1 Invariance w.r.t. constraint function

Let $K_i(\boldsymbol{\theta}) = H_i\left(G_i(\boldsymbol{\theta})\right)$ for $i = 1,...,n_c$ be a composite function with $H_i(0) = 0$. Since $\boldsymbol{\theta} = \mathbf{v}_c(\mathbf{u})$, we have $K_i\left(\mathbf{v}_c(\mathbf{u})\right) = 0$ and $G_i\left(\mathbf{v}_c(\mathbf{u})\right) = 0$. Now denote $\hat{\boldsymbol{\lambda}} = [\hat{\lambda}_1,...,\hat{\lambda}_{n_c}]^T$ and $\hat{\boldsymbol{\lambda}}' = [\hat{\lambda}_1',...,\hat{\lambda}_{n_c}']^T$ as the vectors of Lagrange multipliers at MPV corresponding to the constraint functions $\left\{G_i(\boldsymbol{\theta})\right\}_{i=1}^{n_c}$ and $\left\{K_i(\boldsymbol{\theta})\right\}_{i=1}^{n_c}$, respectively.

For any $\boldsymbol{\theta}$, the gradient and the Hessian of the composite function $K_i(\boldsymbol{\theta})$ for $i = 1,...,n_c$ are respectively given by

$$\nabla_{\boldsymbol{\theta}} K_i = H_i' \nabla_{\boldsymbol{\theta}} G_i \qquad \nabla_{\boldsymbol{\theta}}^2 K_i = H_i'' \left(\nabla_{\boldsymbol{\theta}} G_i\right)^T \nabla_{\boldsymbol{\theta}} G_i + H_i' \nabla_{\boldsymbol{\theta}}^2 G_i \tag{31}$$

where

$$H_i' = \left.\frac{dH_i(x)}{dx}\right|_{x=G_i(\boldsymbol{\theta})} \qquad H_i'' = \left.\frac{d^2 H_i(x)}{dx^2}\right|_{x=G_i(\boldsymbol{\theta})} \tag{32}$$

Evaluating (31) at the MPV and noting $G_i(\hat{\boldsymbol{\theta}}) = 0$ for $i = 1,...,n_c$ gives

$$\nabla_{\boldsymbol{\theta}} \hat{K}_i = H_i'(0) \nabla_{\boldsymbol{\theta}} \hat{G}_i \tag{33}$$

$$\nabla_{\boldsymbol{\theta}}^2 \hat{K}_i = H_i''(0) \left(\nabla_{\boldsymbol{\theta}} \hat{G}_i\right)^T \nabla_{\boldsymbol{\theta}} \hat{G}_i + H_i'(0) \nabla_{\boldsymbol{\theta}}^2 \hat{G}_i \tag{34}$$

Now assemble the gradient of $\hat{K}_i(\boldsymbol{\theta})$ column-wise for $i = 1,...,n_c$. It gives

$$\nabla_{\boldsymbol{\theta}} \hat{\mathbf{K}} = \begin{bmatrix} \nabla_{\boldsymbol{\theta}} \hat{K}_1 \\ \vdots \\ \nabla_{\boldsymbol{\theta}} \hat{K}_{n_c} \end{bmatrix} = \begin{bmatrix} H_i'(0) & & \\ & \ddots & \\ & & H_{n_c}'(0) \end{bmatrix} \begin{bmatrix} \nabla_{\boldsymbol{\theta}} \hat{G}_1 \\ \vdots \\ \nabla_{\boldsymbol{\theta}} \hat{G}_{n_c} \end{bmatrix} = \mathbf{D} \nabla_{\boldsymbol{\theta}} \hat{\mathbf{G}} \tag{35}$$

where

$$\mathbf{D} = \begin{bmatrix} H_i'(0) & & \\ & \ddots & \\ & & H_{n_c}'(0) \end{bmatrix} \tag{36}$$

The Lagrange multiplier corresponding to $\left\{K_i(\boldsymbol{\theta})\right\}_{i=1}^{n_c}$ can be calculated from

$$\hat{\boldsymbol{\lambda}}' = -\frac{\nabla_{\boldsymbol{\theta}} \hat{\mathbf{K}} (\nabla_{\boldsymbol{\theta}} \hat{L})^T}{\nabla_{\boldsymbol{\theta}} \hat{\mathbf{K}} (\nabla_{\boldsymbol{\theta}} \hat{\mathbf{K}})^T} = -\frac{\mathbf{D} \nabla_{\boldsymbol{\theta}} \hat{\mathbf{G}} (\nabla_{\boldsymbol{\theta}} \hat{L})^T}{\mathbf{D} \nabla_{\boldsymbol{\theta}} \hat{\mathbf{G}} (\nabla_{\boldsymbol{\theta}} \hat{\mathbf{G}})^T \mathbf{D}^T} = \mathbf{D}^{-1} \hat{\boldsymbol{\lambda}} \tag{37}$$

This implies

$$\hat{\lambda}_i' = \frac{\hat{\lambda}_i}{H_i'(0)} \qquad \text{for} \quad i = 1,...,n_c \tag{38}$$

Multiplying (38) by both sides of (34) gives

$$\hat{\lambda}_i \nabla_{\boldsymbol{\theta}}^2 \hat{K}_i = \hat{\lambda}_i \frac{H_i''(0)}{H_i'(0)} (\nabla_{\boldsymbol{\theta}} \hat{G}_i)^T \nabla_{\boldsymbol{\theta}} \hat{G}_i + \hat{\lambda}_i \nabla_{\boldsymbol{\theta}}^2 \hat{G}_i \tag{39}$$

Further left and right multiplying $\nabla \hat{\mathbf{v}}_c$ by both sides of (39) gives

$$(\nabla_{\mathbf{u}} \hat{\mathbf{v}}_c)^T (\hat{\lambda}_i \nabla_{\boldsymbol{\theta}}^2 \hat{K}_i) \nabla_{\mathbf{u}} \hat{\mathbf{v}}_c = \hat{\lambda}_i \frac{H_i''(0)}{H_i'(0)} (\nabla_{\boldsymbol{\theta}} \hat{G}_i \nabla_{\mathbf{u}} \hat{\mathbf{v}}_c)^T \nabla_{\boldsymbol{\theta}} \hat{G}_i \nabla_{\mathbf{u}} \hat{\mathbf{v}}_c + (\nabla_{\mathbf{u}} \hat{\mathbf{v}}_c)^T (\hat{\lambda}_i \nabla_{\boldsymbol{\theta}}^2 \hat{G}_i) \nabla_{\mathbf{u}} \hat{\mathbf{v}}_c \tag{40}$$

Since the gradient of $G_i(\mathbf{v}_c(\mathbf{u})) = 0$ evaluated at the MPV is $\nabla_{\boldsymbol{\theta}} \hat{G}_i \nabla_{\mathbf{u}} \hat{\mathbf{v}}_c = \mathbf{0}$, the first term on the RHS of (40) is zero. It then gives

$$(\nabla_{\mathbf{u}} \hat{\mathbf{v}}_c)^T (\hat{\lambda}_i \nabla_{\boldsymbol{\theta}}^2 \hat{K}_i) \nabla_{\mathbf{u}} \hat{\mathbf{v}}_c = (\nabla_{\mathbf{u}} \hat{\mathbf{v}}_c)^T (\hat{\lambda}_i \nabla_{\boldsymbol{\theta}}^2 \hat{G}_i) \nabla_{\mathbf{u}} \hat{\mathbf{v}}_c \tag{41}$$

It finally gives the same $\nabla_{\mathbf{u}}^2 \hat{L}_c$, which proves the invariance of the constraint function.

2.5.2 Invariance w.r.t. free parameters

Let $\mathbf{a} = [a_1,...,a_q]^T$ be a new set of free parameters and $\mathbf{u} = \mathbf{T}(\mathbf{a})$, where $\mathbf{T}$ is a transformation function. Define a function $\boldsymbol{\theta} = \mathbf{w}(\mathbf{a})$ that maps $\mathbf{a}$ to $\boldsymbol{\theta}$, so that it always satisfies the constraints and it has $\mathbf{w}(\mathbf{a}) = \mathbf{v}_c\left(\mathbf{T}(\mathbf{a})\right)$. The mappings are expressed as

$$\mathbf{a} = \begin{bmatrix} a_1 \\ \vdots \\ a_p \end{bmatrix} \xrightarrow{\mathbf{w}(\mathbf{a})} \boldsymbol{\theta} = \begin{bmatrix} \theta_1 \\ \vdots \\ \theta_n \end{bmatrix} \qquad \mathbf{u} = \begin{bmatrix} u_1 \\ \vdots \\ u_p \end{bmatrix} \xrightarrow{\mathbf{v}(\mathbf{u})} \boldsymbol{\theta} = \begin{bmatrix} \theta_1 \\ \vdots \\ \theta_n \end{bmatrix} \tag{42}$$

The NL function of the Bayesian inference problem can then be formulated as

$$K(\mathbf{a}) = L(\mathbf{w}(\mathbf{a})) \tag{43}$$

Now working on the new NL function and applying (9), the posterior covariance matrix, denoted by $\hat{\mathbf{C}}'$, is given by

$$\hat{\mathbf{C}}' = (\nabla_{\mathbf{a}}\hat{\mathbf{w}})(\nabla_{\mathbf{a}}^2\hat{K})^{+}(\nabla_{\mathbf{a}}\hat{\mathbf{w}})^T \tag{44}$$

where

$$\nabla_{\mathbf{a}}^2\hat{K} = (\nabla_{\mathbf{a}}\hat{\mathbf{w}})^T(\nabla_{\mathbf{a}}^2\hat{J})(\nabla_{\mathbf{a}}\hat{\mathbf{w}}) \tag{45}$$

and

$$\nabla_{\mathbf{a}}^2\hat{J} = \nabla_{\mathbf{a}}^2\hat{L} + \sum_{i=1}^{n_c}\hat{\lambda}_i\nabla_{\mathbf{a}}^2\hat{G}_i \tag{46}$$

Denoting $\mathbf{T} = [t_1,...,t_p]^T$ and noting $\mathbf{w}(\mathbf{a}) = \mathbf{v}_c\left(\mathbf{T}(\mathbf{a})\right)$, it can be shown that the derivative of $\mathbf{w}(\mathbf{a})$ w.r.t. a_i is given by

$$\frac{\partial\mathbf{w}}{\partial a_i} = \sum_{j=1}^{p}\frac{\partial\mathbf{v}_c}{\partial t_j}\frac{\partial t_j}{\partial a_i} = \left[\begin{array}{ccc}\frac{\partial\mathbf{v}_c}{\partial t_1} & \cdots & \frac{\partial\mathbf{v}_c}{\partial t_p}\end{array}\right]\left[\begin{array}{c}\partial t_1/\partial a_i \\ \vdots \\ \partial t_p/\partial a_i\end{array}\right] = \nabla_{\mathbf{t}}\mathbf{v}_c\frac{\partial\mathbf{T}}{\partial a_i} \tag{47}$$

The gradient of $\mathbf{w}(\mathbf{a})$ evaluating at MPV is then given by

$$\nabla\hat{\mathbf{w}} = \left[\begin{array}{ccc}\frac{\partial\hat{\mathbf{w}}}{\partial a_1} & \cdots & \frac{\partial\hat{\mathbf{w}}}{\partial a_q}\end{array}\right] = \nabla_{\mathbf{t}}\hat{\mathbf{v}}_c\left[\begin{array}{ccc}\frac{\partial\hat{\mathbf{T}}}{\partial a_1} & \cdots & \frac{\partial\hat{\mathbf{T}}}{\partial a_q}\end{array}\right] = \nabla_{\mathbf{t}}\hat{\mathbf{v}}_c\nabla_{\mathbf{a}}\hat{\mathbf{T}} \tag{48}$$

Substituting (48) into (44) and (45) gives

$$\hat{\mathbf{C}}' = \nabla_{\mathbf{t}}\hat{\mathbf{v}}_c \nabla_{\mathbf{a}}\hat{\mathbf{T}}\left[(\nabla_{\mathbf{a}}\hat{\mathbf{T}})^T(\nabla_{\mathbf{t}}\hat{\mathbf{v}}_c)^T \nabla_{\mathbf{a}}^2 \hat{J} \nabla_{\mathbf{t}}\hat{\mathbf{v}}_c \nabla_{\mathbf{a}}\hat{\mathbf{T}}\right]^+ (\nabla_{\mathbf{t}}\hat{\mathbf{v}}_c \nabla_{\mathbf{a}}\hat{\mathbf{T}})^T \tag{49}$$

On the other hand, recall $\nabla^2 \hat{L}_c$ from (13) and consider singular value decomposition, i.e.,

$$\nabla_{\mathbf{a}}^2 \hat{L}_c = (\nabla_{\mathbf{t}}\hat{\mathbf{v}}_c)^T(\nabla_{\mathbf{a}}^2 \hat{J})(\nabla_{\mathbf{t}}\hat{\mathbf{v}}_c) = \mathbf{U}\Lambda\mathbf{U}^T \tag{50}$$

where $\Lambda \in R^{s\times s}$ is a diagonal matrix containing $p - n_\theta + n_c$ singular values ; $\mathbf{U} \in R^{p\times s}$ is the corresponding matrix that contains orthonormal singular vectors and has $\mathbf{U}^T\mathbf{U} = \mathbf{I}_s$ (identity matrix). The pseudo-inverse of $\nabla_{\mathbf{a}}^2 \hat{L}_c$ can then be expressed in terms of Λ and $\mathbf{U}$, i.e.,

$$[\nabla_{\mathbf{a}}^2 \hat{L}_c]^+ = \mathbf{U}\Lambda^{-1}\mathbf{U}^T \tag{51}$$

and hence the posterior covariance matrix $\hat{\mathbf{C}}$ is

$$\hat{\mathbf{C}} = \nabla_{\mathbf{t}}\hat{\mathbf{v}}\left[\mathbf{U}\Lambda^{-1}\mathbf{U}^T\right](\nabla_{\mathbf{t}}\hat{\mathbf{v}})^T \tag{52}$$

In order to show the invariance to the choice of different sets of free parameters, it is necessary for the $\hat{\mathbf{C}}'$ from (49) to be equal to the $\hat{\mathbf{C}}$ from (52). This is shown in the following.

To facilitate the derivations, we first introduce the SVD of $\mathbf{U}^T\nabla_{\mathbf{a}}\hat{\mathbf{T}}$, i.e.,

$$\underbrace{\mathbf{U}^T}_{s\times p}\ \underbrace{\nabla_{\mathbf{a}}\hat{\mathbf{T}}}_{p\times q}\ \Big\}_{s\times q} = \underset{s\times s}{P_1}\ \underset{s\times s}{\Lambda_1}\ \underset{s\times q}{R_1^T} \tag{53}$$

and further the SVD of $\Lambda_1 P_1^T \Lambda P_1 \Lambda_1$, i.e.,

$$\underbrace{\Lambda_1 P_1^T \Lambda P_1 \Lambda_1}_{s\times s} = \underset{s\times s}{P_2}\ \underset{s\times s}{\Lambda_2}\ \underset{s\times s}{P_2^T} \tag{54}$$

Using $R_i^T R_i = \mathbf{I}_s$ and $P_i^T P_i = \mathbf{I}_s$, it can be shown that $(R_1 P_2)^T (R_1 P_2) = \mathbf{I}_s$. This implies that the columns of $(R_1 P_2)$ are orthonormal. The pseudo-inverse of $(R_1 P_2)\Lambda_2 (R_1 P_2)^T$ is then given by

$$[(R_1 P_2)\Lambda_2 (R_1 P_2)^T]^+ = (R_1 P_2)\Lambda_2^{-1} (R_1 P_2)^T \tag{55}$$

Substituting (50) into (49) and using (53), (54) and (55), $\hat{\mathbf{C}}'$ can be derived as

$$\begin{aligned}
\hat{\mathbf{C}}' &= (\nabla_{\mathbf{t}} \hat{\mathbf{v}}_c \nabla_{\mathbf{a}} \hat{\mathbf{T}})[\underbrace{(\nabla_{\mathbf{a}} \hat{\mathbf{T}})^T \mathbf{U}}_{R_1 \Lambda_1 P_1^T} \Lambda \underbrace{\mathbf{U}^T \nabla_{\mathbf{a}} \hat{\mathbf{T}}}_{P_1 \Lambda_1 R_1^T}]^+ (\nabla_{\mathbf{t}} \hat{\mathbf{v}}_c \nabla_{\mathbf{a}} \hat{\mathbf{T}})^T \\
&= (\nabla_{\mathbf{t}} \hat{\mathbf{v}}_c \nabla_{\mathbf{a}} \hat{\mathbf{T}})[R_1 \underbrace{\Lambda_1 P_1^T \Lambda P_1 \Lambda_1}_{P_2 \Lambda_2 P_2^T} R_1^T]^+ (\nabla_{\mathbf{t}} \hat{\mathbf{v}}_c \nabla_{\mathbf{a}} \hat{\mathbf{T}})^T \\
&= (\nabla_{\mathbf{t}} \hat{\mathbf{v}}_c \nabla_{\mathbf{a}} \hat{\mathbf{T}})[(R_1 P_2)\Lambda_2 (R_1 P_2)^T]^+ (\nabla_{\mathbf{t}} \hat{\mathbf{v}}_c \nabla_{\mathbf{a}} \hat{\mathbf{T}})^T \\
&= (\nabla_{\mathbf{t}} \hat{\mathbf{v}}_c \nabla_{\mathbf{a}} \hat{\mathbf{T}}) R_1 \underbrace{P_2 \Lambda_2^{-1} P_2^T}_{(\Lambda_1 P_1^T \Lambda P_1 \Lambda_1)^{-1}} R_1^T (\nabla_{\mathbf{t}} \hat{\mathbf{v}}_c \nabla_{\mathbf{a}} \hat{\mathbf{T}})^T \\
&= \nabla_{\mathbf{t}} \hat{\mathbf{v}}_c [(\nabla_{\mathbf{a}} \hat{\mathbf{T}}) R_1] \Lambda_1^{-1} P_1^T \Lambda^{-1} P_1 \Lambda_1^{-1} [(\nabla_{\mathbf{a}} \hat{\mathbf{T}}) R_1]^T (\nabla_{\mathbf{t}} \hat{\mathbf{v}}_c)^T
\end{aligned} \tag{56}$$

As shown by (50), $\nabla_{\mathbf{a}}^2 \hat{L}_c$ and $\nabla_{\mathbf{t}} \hat{\mathbf{v}}_c$ have the same null space. This null space is orthogonal to the space that is spanned by the columns in $\mathbf{U}$. Let the identity matrix $\mathbf{I}_{n_\theta}$ be expressed as

$$\mathbf{I}_{n_\theta} = \mathbf{U}\mathbf{U}^T + \mathbf{V}\mathbf{V}^T \tag{57}$$

where $\mathbf{V}$ contains orthonormal basis for the null space. It then gives

$$\nabla_{\mathbf{t}} \hat{\mathbf{v}}_c = \nabla_{\mathbf{t}} \hat{\mathbf{v}}_c (\mathbf{U}\mathbf{U}^T + \mathbf{V}\mathbf{V}^T) = \nabla_{\mathbf{t}} \hat{\mathbf{v}}_c \mathbf{U}\mathbf{U}^T \tag{58}$$

Since $\nabla_{\mathbf{t}}\hat{\mathbf{v}}_c\mathbf{V}=\mathbf{0}$, substituting (58) into (56) gives

$$\hat{\mathbf{C}}' = \nabla_{\mathbf{t}}\hat{\mathbf{v}}_c\mathbf{U}[\mathbf{U}^T(\nabla_{\mathbf{a}}\hat{\mathbf{T}})R_1]\Lambda_1^{-1}P_1^T\Lambda^{-1}P_1\Lambda_1^{-1}[\mathbf{U}^T(\nabla_{\mathbf{a}}\hat{\mathbf{T}})R_1]^T(\nabla_{\mathbf{t}}\hat{\mathbf{v}}_c\mathbf{U})^T \tag{59}$$

Right-multiply R_1 with both sides of $\mathbf{U}^T\nabla_{\mathbf{a}}\hat{\mathbf{T}}=P_1\Lambda_1R_1^T$ and note that $R_1^TR_1=\mathbf{I}_s$. It then gives $\mathbf{U}^T(\nabla_{\mathbf{a}}\hat{\mathbf{T}})R_1=P_1\Lambda_1$. Substituting the above into (59) and noting $P_1P_1^T=\mathbf{I}_s$ gives

$$\begin{aligned}\hat{\mathbf{C}}' &= \nabla_{\mathbf{t}}\hat{\mathbf{v}}_c\mathbf{U}(P_1\Lambda_1)\Lambda_1^{-1}P_1^T\Lambda^{-1}P_1\Lambda_1^{-1}(\Lambda_1^TP_1^T)(\nabla_{\mathbf{t}}\hat{\mathbf{v}}_c\mathbf{U})^T \\ &= \nabla_{\mathbf{t}}\hat{\mathbf{v}}_c\mathbf{U}\Lambda^{-1}\mathbf{U}^T(\nabla_{\mathbf{t}}\hat{\mathbf{v}}_c)^T=\hat{\mathbf{C}}\end{aligned} \tag{60}$$

The invariance of the posterior covariance matrix to the choice of free parameters is therefore proved.

2.6 Conclusion

This chapter has presented a method for deriving the posterior covariance matrix from the inverse of the Hessian of the NL function, where constraints are systematically incorporated. Two formulae have been derived. The direct formula is applicable for any parameter values. The Lagrange formula is only valid at MPV but the expression is more compact. Both formulae can be used for deriving the Hessian of a function that is subjected to constraints. Compared to the conventional way of deriving constrained Hessian, which involves brute-force and repeated differentiation using the chain rule, the proposed theory provides a systemic way of handling the constraints. This potentially facilitates efficient computer coding in calculating the Hessian matrix and hence the posterior covariance matrix. In the next chapter, the proposed theory is applied to the uncertainty calculation of Bayesian modal identification with single setup and multiple-setup data, followed by validation with numerical examples.

Chapter 3 Uncertainty calculation in Bayesian OMA

3.1 Introduction

In Bayesian modal identification, the prior PDF is often assumed to be uniformly distributed, since it is slowly varying compared to the likelihood function. The posterior PDF is then proportional to the likelihood function, i.e.,

$$p(\boldsymbol{\theta}|D) \propto p(D|\boldsymbol{\theta}) = e^{-L(\boldsymbol{\theta})} \tag{61}$$

where $L(\boldsymbol{\theta}) = -\ln p(D|\boldsymbol{\theta})$ is the NLLF; $\boldsymbol{\theta}$ and D denote the set of modal parameters and measured data, respectively. The posterior covariance matrix is then determined from the inverse of the Hessian of the NLLF. Computational issues associated with the Hessian arise from the norm constraint with regard to the mode shape. One conventional way of deriving the Hessian under constraints involves brute-force and repeated differentiation using the chain rule [63,88]. Alternatively, the Hessian with constrained modal parameters can be systematically handled using the theory developed in Chapter 2. This chapter applies the theory to derive the constrained Hessian and evaluate the posterior covariance matrix in Bayesian modal identification with single setup and multiple-setup data. Synthetic data examples are provided to validate the proposed theory, where computation efficiency is also discussed.

3.2 Single setup data

The Bayesian FFT formulation for a single setup [63] is first reviewed. The direct formula (10) and Lagrange formula (13) developed in Chapter 2 are applied for deriving the constrained Hessian matrix, and hence the posterior covariance matrix.

3.2.1 Review of Bayesian FFT formulation with single setup data

In the single setup setting, let $\boldsymbol{\theta}$ be a collection of modal parameters that consists of the natural frequency (f), damping ratio (ζ), modal force PSD (S), prediction error (S_e) and mode shape ($\boldsymbol{\varphi}$), i.e., $\boldsymbol{\theta} = \{f, \zeta, S, S_e, \boldsymbol{\varphi}\}$. Define $\{\mathbf{y}_j \in R^n\}_{j=1}^N$ as the time history of ambient acceleration data with n measured DOFs. The (scaled) FFT of $\{\mathbf{y}_j\}$ is defined as

$$\mathcal{F}_k = \sqrt{\frac{2\Delta t}{N}} \sum_{j=1}^{N} \hat{\mathbf{y}}_j \exp\left[-2\pi \mathbf{i} \frac{(k-1)(j-1)}{N} \right] \qquad (k = 1, ..., N) \tag{62}$$

where $\mathbf{i}^2 = -1$ and Δt is the sampling interval. Let $\{\mathcal{F}_k\}$ denote the collection of FFT data over a selected frequency band around the mode of interest. For small Δt and large N , it can be shown that $\{\mathcal{F}_k\}$ are asymptotically independent and jointly 'circularly complex Gaussian' with zero mean and covariance matrix equal to the PSD matrix of data [59]. Correspondingly, the NLLF is given by

$$L(\boldsymbol{\theta}) = nN_f \ln \pi + \sum_k \ln |\mathbf{E}_k(\boldsymbol{\theta})| + \sum_k \mathcal{F}_k^* \mathbf{E}_k(\boldsymbol{\theta})^{-1} \mathcal{F}_k \tag{63}$$

where the sum is over the selected frequency band with N_f FFT points; $\mathbf{E}_k(\boldsymbol{\theta}) = E[\mathcal{F}_k \mathcal{F}_k^* | \boldsymbol{\theta}]$ is the theoretical PSD matrix of data for given $\boldsymbol{\theta}$. Assuming that the selected frequency band is dominated by a single mode, $\mathbf{E}_k$ is given by

$$\mathbf{E}_k = SD_k \boldsymbol{\varphi}\boldsymbol{\varphi}^T + S_e \mathbf{I}_n \tag{64}$$

where $\mathbf{I}_n$ is the $n \times n$ identity matrix; D_k is the dynamic amplification factor:

$$D_k = \frac{1}{(1-\beta_k^2)^2 + (2\zeta\beta_k)^2} \qquad (\beta_k = f / \mathrm{f}_k) \tag{65}$$

Using analytical expressions for the determinant and inverse of $\mathbf{E}_k$ [63], and then substituting it into (63), the NLLF can be derived as

$$L(\boldsymbol{\theta}) = nN_f \ln \pi + \sum_k \ln(SD_k + S_e) + (n-1)N_f \ln S_e + S_e^{-1} d - S_e^{-1} \boldsymbol{\varphi}^T \mathbf{A} \boldsymbol{\varphi} \tag{66}$$

where

$$\mathbf{A} = \sum_k (1 + \frac{S_e}{SD_k})^{-1} \hat{\mathbf{D}}_k \qquad \hat{\mathbf{D}}_k = \mathrm{Re}(\mathcal{F}_k \mathcal{F}_k^*) \qquad d = \sum_k \mathcal{F}_k^* \mathcal{F}_k \tag{67}$$

The mode shape is assumed to have unit Euclidean norm, i.e., $\| \boldsymbol{\varphi} \|^2 = \boldsymbol{\varphi}^T \boldsymbol{\varphi} = 1$. Deriving the posterior covariance matrix requires the inverse of the Hessian of the NLLF, where the unit norm constraint has to be taken into account. The following section applies the proposed theory in Chapter 2 for deriving the constrained Hessian matrix, inverting which will give the posterior covariance matrix.

3.2.2 Calculating the posterior covariance matrix

Let $\mathbf{u} = [\varpi;\ \boldsymbol{\varphi}]$ be a vector of free parameters, where $\varpi = [f, \zeta, S, S_e]^T$ comprises the modal parameters other than the mode shape. To apply the developed formulae (i.e., (10) and (13)) for constrained Hessian, we first define a mapping function $\mathbf{v}_c(\mathbf{u})$ from $\mathbf{u}$ to $\boldsymbol{\theta}$ that always satisfies the constraint, i.e., $G(\mathbf{v}_c(\mathbf{u})) \equiv 0$. The definitions are listed below

$$\mathbf{u}=\begin{bmatrix}\varpi\\ \boldsymbol{\varphi}\end{bmatrix} \qquad \boldsymbol{\theta}=\begin{bmatrix}\varpi\\ \bar{\boldsymbol{\varphi}}\end{bmatrix} \qquad \mathbf{v}_c(\mathbf{u})=\begin{bmatrix}\varpi\\ \boldsymbol{\varphi}/\|\boldsymbol{\varphi}\|\end{bmatrix} \qquad G(\boldsymbol{\theta})=1-\boldsymbol{\varphi}^T\boldsymbol{\varphi} \tag{68}$$

Deriving the constrained Hessian through the direct formula (10) requires the gradient and the Hessian of $\mathbf{v}_c(\mathbf{u})$ and $L(\boldsymbol{\theta})$ evaluated at MPV. They are given by

$$\nabla_{\mathbf{u}}\hat{\mathbf{v}}_c=\begin{bmatrix}\mathbf{I}_{4\times4} & \\ & \mathbf{I}_n-\hat{\boldsymbol{\varphi}}\hat{\boldsymbol{\varphi}}^T\end{bmatrix} \tag{69}$$

$$\nabla^2_{\mathbf{u}}\hat{\mathbf{v}}_c=\begin{bmatrix}\nabla^2_{\varpi}\hat{\mathbf{v}}_c\\ \nabla^2_{\boldsymbol{\varphi}}\hat{\mathbf{v}}_c\end{bmatrix}=\begin{bmatrix}\mathbf{0}_{4p\times p}\\ (3\hat{\boldsymbol{\varphi}}\hat{\boldsymbol{\varphi}}^T-\mathbf{I}_n)\otimes\hat{\boldsymbol{\varphi}}-\hat{\boldsymbol{\varphi}}\otimes\mathbf{I}_n-\mathbf{I}_n(:)\otimes\hat{\boldsymbol{\varphi}}^T\end{bmatrix} \tag{70}$$

$$\nabla_{\boldsymbol{\theta}}\hat{L}=\begin{bmatrix}\nabla_{\varpi}\hat{L} & -2\hat{S}_e^{-1}\hat{\boldsymbol{\varphi}}^T\hat{\mathbf{A}}\end{bmatrix} \tag{71}$$

$$\nabla^2_{\boldsymbol{\theta}}\hat{L}=\begin{bmatrix}\nabla^2_{\varpi}\hat{L} & -2\hat{\boldsymbol{\varphi}}^T(\hat{S}_e^{-1}\hat{\mathbf{A}})^{(\varpi)}\\ sym. & -2\hat{S}_e^{-1}\hat{\mathbf{A}}\end{bmatrix} \tag{72}$$

where $\mathbf{I}_n(:)$ denotes the vectorisation of an n dimensional identity matrix by stacking its columns.

Substituting (69) and (72) into the first term on the RHS of (10) gives

$$(\nabla_{\mathbf{u}}\hat{\mathbf{v}}_c)^T\nabla^2_{\boldsymbol{\theta}}\hat{L}(\nabla_{\mathbf{u}}\hat{\mathbf{v}}_c)=\begin{bmatrix}\nabla^2_{\varpi}\hat{L} & -2\hat{\boldsymbol{\varphi}}^T(\hat{S}_e^{-1}\hat{\mathbf{A}})^{(\varpi)}(\mathbf{I}_n-\hat{\boldsymbol{\varphi}}\hat{\boldsymbol{\varphi}}^T)\\ sym. & 2S_e^{-1}(\hat{\lambda}\hat{\boldsymbol{\varphi}}\hat{\boldsymbol{\varphi}}^T-\hat{\mathbf{A}})\end{bmatrix} \tag{73}$$

Substituting (70) and (71) into the second term on the RHS of (10) gives

$$\left[\mathbf{I}_p\otimes\nabla_{\boldsymbol{\theta}}\hat{L}\right]\nabla^2_{\mathbf{u}}\hat{\mathbf{v}}_c=\begin{bmatrix}\mathbf{0}_{4\times4} & \\ & \mathbf{U}\end{bmatrix} \tag{74}$$

where

$$\mathbf{U} = [\mathbf{I}_n \otimes (-2S_e^{-1}\hat{\boldsymbol{\varphi}}^T \mathbf{A})] \times \left[(3\hat{\boldsymbol{\varphi}}\hat{\boldsymbol{\varphi}}^T - \mathbf{I}_n) \otimes \hat{\boldsymbol{\varphi}} - \hat{\boldsymbol{\varphi}} \otimes \mathbf{I}_n - \mathbf{I}_n(:) \otimes \hat{\boldsymbol{\varphi}}^T \right] \tag{75}$$

Using the mixed-product property of Kronecker

$$(\mathbf{A} \otimes \mathbf{B})(\mathbf{C} \otimes \mathbf{D}) = (\mathbf{AC}) \otimes (\mathbf{BD}) \tag{76}$$

where $\mathbf{A}$, $\mathbf{B}$, $\mathbf{C}$, $\mathbf{D}$ are matrices with proper size, (75) can be simplified as

$$\begin{aligned} \mathbf{U} &= (3\hat{\boldsymbol{\varphi}}\hat{\boldsymbol{\varphi}}^T - \mathbf{I}_n) \otimes (-2S_e^{-1}\hat{\boldsymbol{\varphi}}^T \mathbf{A})\hat{\boldsymbol{\varphi}} - \hat{\boldsymbol{\varphi}} \otimes (-2S_e^{-1}\hat{\boldsymbol{\varphi}}^T \mathbf{A}) - \mathbf{I}_n(:) \otimes \hat{\boldsymbol{\varphi}}^T (-2S_e^{-1}\hat{\boldsymbol{\varphi}}^T \mathbf{A}) \\ &= -2S_e^{-1}[\hat{\lambda}(3\hat{\boldsymbol{\varphi}}\hat{\boldsymbol{\varphi}}^T - \mathbf{I}_n) - \hat{\lambda}\hat{\boldsymbol{\varphi}}\hat{\boldsymbol{\varphi}}^T - \hat{\lambda}\hat{\boldsymbol{\varphi}}\hat{\boldsymbol{\varphi}}^T] \\ &= 2S_e^{-1}\hat{\lambda}(\mathbf{I}_n - \hat{\boldsymbol{\varphi}}\hat{\boldsymbol{\varphi}}^T) \end{aligned} \tag{77}$$

Substituting (73) and (74) into (10) gives

$$\nabla_{\mathbf{u}}^2 L_c = \begin{bmatrix} \hat{L}^{(\varpi\varpi)} & -2\hat{\boldsymbol{\varphi}}^T (\hat{S}_e^{-1}\hat{\mathbf{A}})^{(\varpi)} (\mathbf{I}_n - \hat{\boldsymbol{\varphi}}\hat{\boldsymbol{\varphi}}^T) \\ sym. & 2S_e^{-1}(\hat{\lambda}_1 \mathbf{I}_n - \hat{\mathbf{A}}) \end{bmatrix} \tag{78}$$

Equation (78) gives an analytical expression of the Hessian of the NLLF, where the mode shape constraint has been incorporated. Further substituting (69) and (78) into (9) gives the posterior covariance matrix. The derivation through the direct formula involves calculating the first two derivatives of $\hat{\mathbf{v}}_c$ and $\hat{L}$.

To apply the Lagrange formula (13) for deriving the constrained Hessian, we first obtain the gradient of $G(\boldsymbol{\theta})$ and $L(\boldsymbol{\theta})$ evaluated at MPV, i.e.,

$$\nabla_{\boldsymbol{\theta}} \hat{G} = [\mathbf{0}_{1\times 4} \quad -2\hat{\boldsymbol{\varphi}}^T] \tag{79}$$

$$\nabla_{\boldsymbol{\theta}} \hat{L} = \left[\nabla_{\varpi} \hat{L} \quad -2\hat{S}_e^{-1}\hat{\boldsymbol{\varphi}}^T \hat{\mathbf{A}} \right] \tag{80}$$

By substituting (79) and (80) into (14), the Lagrange multiplier $\hat{\boldsymbol{\lambda}}$ can be calculated as

$$\hat{\boldsymbol{\lambda}} = -S_e^{-1}\frac{\hat{\boldsymbol{\varphi}}^T\hat{\mathbf{A}}\hat{\boldsymbol{\varphi}}}{\hat{\boldsymbol{\varphi}}^T\hat{\boldsymbol{\varphi}}} = -S_e^{-1}\hat{\lambda}_1 \tag{81}$$

where $\hat{\lambda}_1$ is the maximum eigenvalue of $\hat{\mathbf{A}}$.

Further taking the gradient of $\mathbf{v}_c(\mathbf{u})$ and the second derivatives of $G(\boldsymbol{\theta})$ and $L(\hat{\boldsymbol{\theta}})$ gives

$$\nabla_{\mathbf{u}}^2\mathbf{v}_c = \begin{bmatrix} \mathbf{I}_{4\times4} & \\ & \mathbf{I}_n - \hat{\boldsymbol{\varphi}}\hat{\boldsymbol{\varphi}}^T \end{bmatrix} \tag{82}$$

$$\nabla_{\boldsymbol{\theta}}^2 G = \begin{bmatrix} \mathbf{0}_{4\times4} & \\ & -2\mathbf{I}_n \end{bmatrix} \tag{83}$$

$$\nabla_{\boldsymbol{\theta}}^2\hat{L} = \begin{bmatrix} \nabla_{\varpi}^2\hat{L} & -2\hat{\boldsymbol{\varphi}}^T(\hat{S}_e^{-1}\hat{\mathbf{A}})^{(\varpi)} \\ sym. & -2\hat{S}_e^{-1}\hat{\mathbf{A}} \end{bmatrix} \tag{84}$$

Substituting the above derivatives into (13) gives the constrained Hessian as

$$\nabla_{\mathbf{u}}^2\hat{L}_c = \begin{bmatrix} \hat{L}^{(\varpi\varpi)} & -2\hat{\boldsymbol{\varphi}}^T(\hat{S}_e^{-1}\hat{\mathbf{A}})^{(\varpi)}(\mathbf{I}_n - \hat{\boldsymbol{\varphi}}\hat{\boldsymbol{\varphi}}^T) \\ sym. & 2S_e^{-1}(\hat{\lambda}\mathbf{I}_n - \hat{\mathbf{A}}) \end{bmatrix} \tag{85}$$

The expression of (85) is the same as that in (78), which verifies the consistency of the two formulae. The posterior covariance matrix can be obtained by substituting (69) and (85) into (9).

3.3 Multiple-setup data

In order to facilitate the derivation of the constrained Hessian, the original Bayesian FFT method [65] is reformulated. The constrained Hessian matrix is then derived through the Lagrange formula.

3.3.1 Reformulation of the Bayesian OMA with multiple-setup data

Consider an ambient vibration test with a total number of n DOFs to be covered in n_s setups. At least one common DOF is shared between two setups. Define $\boldsymbol{\theta}$ as a collection of $\{f_i, \zeta_i, S_i, S_{e_i}\}_{i=1}^{n_s}$ and global mode shape $\boldsymbol{\varphi}$. Let $\mathbf{L}_i \in R^{n_i \times n}$ denote the selection matrix for the i-th setup to choose n_i measured channels from a total of n DOFs, where n_i is the number of DOFs in setup i. The (j,k) entry of $\mathbf{L}_i$ is equal to 1, indicating that the k-th DOF is measured by the j-th channel in setup i. The remaining entries of $\mathbf{L}_i$ are zero. The partial mode shape $\mathbf{v}_i$ for the i-th setup is then given by

$$\mathbf{v}_i = \mathbf{L}_i \boldsymbol{\varphi} \qquad (i = 1, ..., n_s) \tag{86}$$

Denote $D_i = \{\mathcal{F}_k^{(i)}\}$ as a collection of FFT data for setup i over a selected frequency band that covers the mode to be identified. The data in different setups are assumed to be independent. The posterior PDF is then given by

$$p(\boldsymbol{\theta}|D) \propto \prod_{r=1}^{n_s} p(D_r|\boldsymbol{\theta}) \tag{87}$$

Correspondingly, the NLLF is given by

$$L(\boldsymbol{\theta}) = \sum_{r=1}^{n_s} L_r \tag{88}$$

where

$$L_r = n_r N_f^{(r)} \ln \pi + \sum_k \left| \mathbf{E}_k^{(r)} \right| + \sum_k \boldsymbol{\mathcal{F}}_k^{(r)^*} \mathbf{E}_k^{(r)^{-1}} \boldsymbol{\mathcal{F}}_k^{(r)} \tag{89}$$

denotes the NLLF for the r-th setup and $\mathbf{E}_k^{(r)}$ is the theoretical PSD matrix of data given by

$$\mathbf{E}_k^{(r)} = S_r D_k^{(r)} \mathbf{v}_r \mathbf{v}_r^T + S_{e_r} \mathbf{I}_{n_r} \tag{90}$$

To facilitate derivation, we denote

$$S_r' = \left\| \mathbf{v}_r \right\|^2 S_r \tag{91}$$

so that $\mathbf{E}_k^{(r)}$ can be rewritten as

$$\mathbf{E}_k^{(r)} = S_r' D_k^{(r)} \bar{\mathbf{v}}_r \bar{\mathbf{v}}_r^T + S_{e_r} \mathbf{I}_{n_r} \tag{92}$$

where $\bar{\mathbf{v}}_r = \left\| \mathbf{v}_r \right\|^{-1} \mathbf{v}_r$ is scaled to have unit norm.

The NLLF for setup r can then be written as

$$\begin{aligned} L_r(\boldsymbol{\theta}_r) = {} & n_r N_f^{(r)} \ln \pi + \sum_k \ln(S_r' D_k^{(r)} + S_{e_r}) + (n_r - 1) N_f^{(r)} \ln S_{e_r} \\ & + S_{e_r}^{-1} d_r - S_{e_r}^{-1} \mathbf{v}_r^T \mathbf{A}_r \mathbf{v}_r \end{aligned} \tag{93}$$

where $\boldsymbol{\theta}_r = \left[f_r,\ \zeta_r,\ S_r',\ S_{e_r},\ \mathbf{v}_r \right]$ and

$$\mathbf{A}_r = \sum_k (1+\frac{S_{e_r}}{S_r' D_k^{(r)}})^{-1} \hat{\mathbf{D}}_k^{(r)} \qquad \hat{\mathbf{D}}_k^{(r)} = \mathrm{Re}(\mathcal{F}_k^{(r)} \mathcal{F}_k^{(r)^*}) \qquad d_r = \sum_k \mathcal{F}_k^{(r)^*} \mathcal{F}_k^{(r)} \tag{94}$$

Working with S_r' instead of S_r, $L_r(\boldsymbol{\theta}_r)$ derived in (94) is of the same form as the NLLF expressed in single setup case. This allows the MPVs and the posterior covariance to be derived with the same mathematical treatment as that in the single setup case. This also facilitates the calculation and computer coding for multiple setups.

3.3.2 Calculating the posterior covariance matrix

Depending on the problem size of multiple setups, the dimension of the Kronecker product in the direct formula can be very large, which may be cumbersome for deriving the constrained Hessian. In this section, the Lagrange formula is applied to the multiple-setup case.

Define a vector of free parameter $\mathbf{u}$, a vector of modal parameter $\boldsymbol{\theta}$ for multiple setups, a mapping function $\mathbf{v}_c(\mathbf{u})$ and constraint function $\mathbf{G}(\boldsymbol{\theta})$ as follow

$$\mathbf{u} = \begin{bmatrix} \varpi_1 \\ \vdots \\ \varpi_q \\ \boldsymbol{\varphi} \end{bmatrix} \quad \boldsymbol{\theta} = \begin{bmatrix} \varpi_1 \\ \vdots \\ \varpi_q \\ \mathbf{v}_1 \\ \vdots \\ \mathbf{v}_q \\ \bar{\boldsymbol{\varphi}} \end{bmatrix} \quad \mathbf{v}_c(\mathbf{u}) = \begin{bmatrix} \varpi_1 \\ \vdots \\ \varpi_q \\ \mathbf{L}_1\boldsymbol{\varphi}/\|\boldsymbol{\varphi}\| \\ \vdots \\ \mathbf{L}_q\boldsymbol{\varphi}/\|\boldsymbol{\varphi}\| \\ \boldsymbol{\varphi}/\|\boldsymbol{\varphi}\| \end{bmatrix} \quad \mathbf{G}(\boldsymbol{\theta}) = \begin{bmatrix} \mathbf{v}_1 - \mathbf{L}_1\boldsymbol{\varphi} \\ \vdots \\ \mathbf{v}_q - \mathbf{L}_q\boldsymbol{\varphi} \\ 1 - \boldsymbol{\varphi}^T\boldsymbol{\varphi} \end{bmatrix} \tag{95}$$

where $\varpi_r = \left[f_r,\ \zeta_r,\ S_r',\ S_{e_r} \right]^T$ contains the parameters for setup r.

Since $\{\mathbf{v}_i\}_{i=1}^q$ are explicitly contained in $\boldsymbol{\theta}$, the derivatives of L w.r.t. partial mode shapes can be treated as independent variables. The derivatives w.r.t. the global mode

shape is then zero because $L = \sum_{r=1}^{n_s} L_r$ and L_r depends on $\mathbf{v}_r$ instead of $\boldsymbol{\varphi}$. When the NLLF in multiple setups is reformulated using S_r' instead of S_r, it has the same expression as the NLLF for the single setup. As a result, the first two derivatives of the NLLF for single setup can be used for multiple setups. The computer codes developed for the single setup can also be used for multiple setups.

The gradient and Hessian of $\mathbf{v}_c(\mathbf{u})$ and $\mathbf{G}(\boldsymbol{\theta})$ at MPV are given by

$$\nabla_{\mathbf{u}} \hat{\mathbf{v}}_c = \begin{bmatrix} \mathbf{I}_{4q} & & \\ & \mathbf{L}_1(\mathbf{I}_n - \hat{\boldsymbol{\varphi}}\hat{\boldsymbol{\varphi}}^T) & \\ & \vdots & \\ & \mathbf{L}_q(\mathbf{I}_n - \hat{\boldsymbol{\varphi}}\hat{\boldsymbol{\varphi}}^T) & \\ & \mathbf{I}_n - \hat{\boldsymbol{\varphi}}\hat{\boldsymbol{\varphi}}^T & \end{bmatrix} \tag{96}$$

$$\nabla_{\boldsymbol{\theta}} \hat{\mathbf{G}} = \begin{bmatrix} \mathbf{0}_{n_1 \times 4q} & \mathbf{I}_{n_1} & & & -\mathbf{L}_1 \\ \vdots & & \ddots & & \vdots \\ \mathbf{0}_{n_q \times 4q} & & & \mathbf{I}_{n_q} & -\mathbf{L}_q \\ \mathbf{0}_{1\times 4q} & \mathbf{0}_{1\times n_1} & \cdots & \mathbf{0}_{1\times n_q} & -2\hat{\boldsymbol{\varphi}}^T \end{bmatrix} \tag{97}$$

$$\nabla_{\boldsymbol{\theta}}^2 \hat{G}_i(\boldsymbol{\theta}) = \mathbf{0}_{n_\theta} \qquad (i = 1, ..., \Sigma n_r) \tag{98}$$

$$\nabla_{\boldsymbol{\theta}}^2 \hat{G}_{1+\Sigma n_r} = \begin{bmatrix} \mathbf{0}_{4q+\Sigma n_r} & \\ & -2\mathbf{I}_n \end{bmatrix} \tag{99}$$

By noting $\boldsymbol{\theta}_r = [\varpi_r; \mathbf{v}_r]$, the gradient and Hessian of $L_r(\boldsymbol{\theta}_r)$ can be expressed as

$$\nabla_{\boldsymbol{\theta}_r} \hat{L}_r = [\hat{L}_r^{(\varpi_r)} \quad \hat{L}_r^{(\mathbf{v}_r)}] \qquad \nabla_{\boldsymbol{\theta}_r}^2 \hat{L}_r(\boldsymbol{\theta}_r) = \begin{bmatrix} \hat{L}_r^{(\varpi_r \varpi_r)} & \hat{L}_r^{(\varpi_r \mathbf{v}_r)} \\ \text{sym.} & \hat{L}_r^{(\mathbf{v}_r \mathbf{v}_r)} \end{bmatrix} \tag{100}$$

The $\nabla_{\boldsymbol{\theta}} L$ and $\nabla_{\boldsymbol{\theta}}^2 L$ can then be derived as

$$\nabla_{\boldsymbol{\theta}}\hat{L}=\begin{bmatrix}\hat{L}_1^{(\varpi_1)} & \cdots & \hat{L}_q^{(\varpi_q)} & \hat{L}_1^{(\nu_1)} & \cdots & \hat{L}_q^{(\nu_q)} & \mathbf{0}_{1\times n}\end{bmatrix} \tag{101}$$

$$\nabla_{\boldsymbol{\theta}}^2\hat{L}=\begin{bmatrix}\hat{L}_1^{(\varpi_1\varpi_1)} & & & \hat{L}_1^{(\varpi_1\nu_1)} & & & \\ & \ddots & & & \ddots & & \\ & & \hat{L}_q^{(\varpi_q\varpi_q)} & & & \hat{L}_q^{(\varpi_q\nu_q)} & \\ & & & \hat{L}_1^{(\nu_1\nu_1)} & & & \\ & & & & \ddots & & \\ & & & & & \hat{L}_q^{(\nu_q\nu_q)} & \\ \text{sym.} & & & & & & \mathbf{0}_n\end{bmatrix} \tag{102}$$

By substituting (97) and (101) into (14), $\hat{\boldsymbol{\lambda}}$ can be obtained. The constrained Hessian $\nabla_{\mathbf{u}}^2\hat{L}_c$ can then be derived by substituting (96), (98), (99), (102) and $\hat{\boldsymbol{\lambda}}$ into (13). The posterior covariance can be obtained using (9). Since the derivation involves operating with large matrices and the dimension depends on the number of DOFs and the number of setups, it is unlikely to admit an analytical formula for the constrained Hessian matrix as in the single setup problem. In principle, since all the required terms for deriving the Hessian have been obtained, the posterior covariance can still be calculated.

3.4 Illustrative examples

In this section, the consistency and computational aspect of the proposed formulae for calculating the posterior covariance matrix are investigated using synthetic data examples. The consistency is demonstrated by comparing the results from the proposed formulae with those obtained from a finite difference method (FDM). The FDM calculates the Hessian matrix with numerical solutions through the partial differential equations, where the accuracy of the result depends on the finite difference approximation of the derivatives. The computational aspect is illustrated by comparing

the computational time of the proposed method with the FDM and a previous method (see [88]). To investigate how computational time scales with problem size, a parametric study is performed w.r.t. the number of DOFs for single setup and the number of setups for multiple setups.

Focusing on a well-separated mode with classical damping, the synthetic data can be modelled as

$$\hat{\mathbf{y}}(t) = \boldsymbol{\varphi}\ddot{\eta}(t) + \boldsymbol{\varepsilon}(t) \tag{103}$$

where $\boldsymbol{\varphi} \in R^{n\times 1}$ is the mode shape with n measured DOFs; $\boldsymbol{\varepsilon}(t)$ is the prediction error; $\eta(t)$ is the modal response that satisfies the uncoupled modal equation, i.e., $\ddot{\eta}(t) + 2\zeta\omega\dot{\eta}(t) + \omega^2\eta(t) = p(t)$, where $\omega = 2\pi f$; $p(t)$ is the modal excitation. Assume a natural frequency of 1 Hz and damping ratio of $\zeta = 1\%$. Assume the modal force and prediction error are i.i.d. Gaussian white noise with a PSD of $2.56\ (\mu g)^2/\text{Hz}$ and $1\ (\mu g)^2/\text{Hz}$, respectively. The data is generated for 1,000 seconds with a sampling rate of 100 Hz. For investigation w.r.t. the number of DOFs, the mode shape is assumed to be $[1,...,1]^T/\sqrt{n} \in R^n$. For the single setup case, the data with i DOFs simply comprises the first i DOFs from the n DOFs. For multiple-setup data, each setup is assumed to have four measured DOFs, including two references and two roving DOFs. The references are fixed at DOF 1 and DOF 2. The roving DOFs are set as $\{3,4\}$ for setup 1, $\{5,6\}$ for setup 2, and continuing with the same pattern until the last setup.

3.4.1 Consistency

The synthetic data for the case of single setup and multiple setups are first analysed using Bayesian modal identification methods [63,65]. The posterior covariance is then calculated using the proposed method and the FDM. The FDM requires the choice of a step size, denoted by $\Delta\boldsymbol{\theta}$. It is parameterised as $\Delta\boldsymbol{\theta} = \hat{\boldsymbol{\theta}} \times d$, where d is a dimensionless scalar and $\hat{\boldsymbol{\theta}}$ consists of all the identified modal parameters. The smaller d gives the smaller step size.

The two methods are compared by calculating the averaged absolute value of the ratio for all the entries of the posterior covariance matrix. The closer the value is to 1 the better.

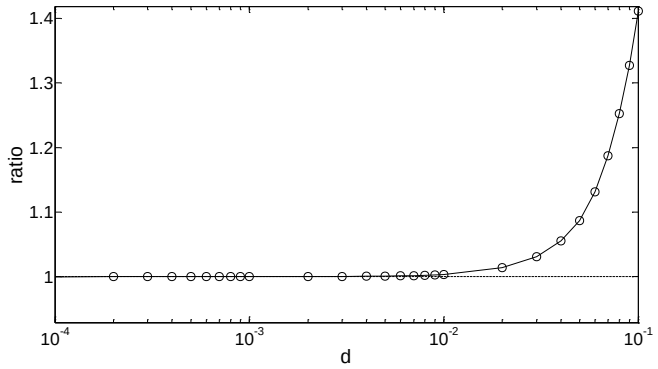

Figure 1 Average ratio of the entries in the posterior covariance matrix calculated by FDM and the proposed method, single setup data with 100 DOFs.

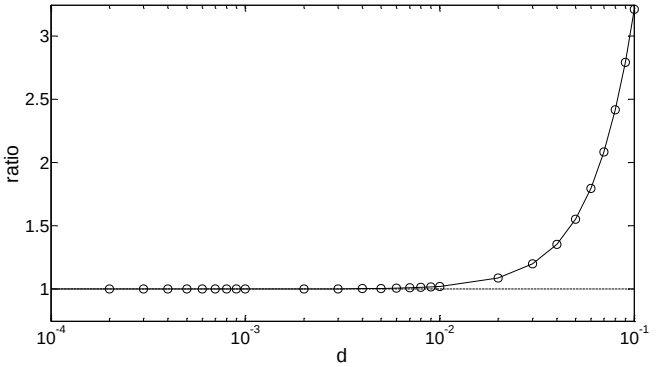

Figure 2 Average ratio of the entries in the posterior covariance matrix calculated by FDM and the proposed method, multiple-setup data with 10 setups.

Figure 1 shows the ratio for 100 DOFs in a single setup. It shows that the ratio converges close to 1 as d decreases to about 0.01. Figure 2 shows the ratio for multiple-setup data with 10 setups. Again, the ratio converges close to 1 as d decreases to about 0.01. Both figures demonstrate the correctness of the proposed method. For other numbers of DOFs and setups, similar results can be obtained. This also verifies the consistency of the proposed method.

3.4.2 Computational time

The computational aspect is investigated by comparing the computational time of the proposed method with the previous method and the FDM. For single setup data, the comparison is conducted by increasing the number of DOFs. For multiple-setup data, the comparison focuses on increasing the number of setups. Computations are performed in MATLAB on a desktop computer (HP Elite Desk, i5-4590T, 2GHz).

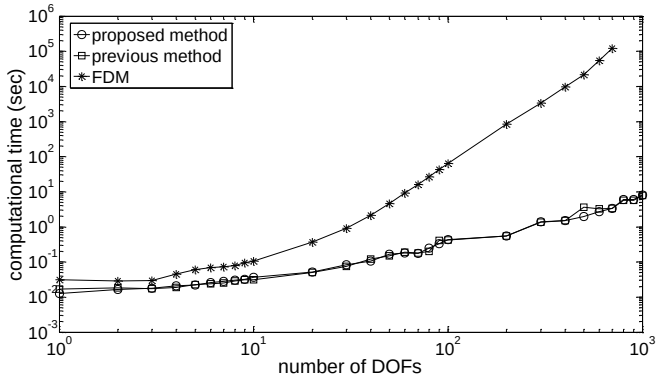

Figure 3 Computational time, single setup data.

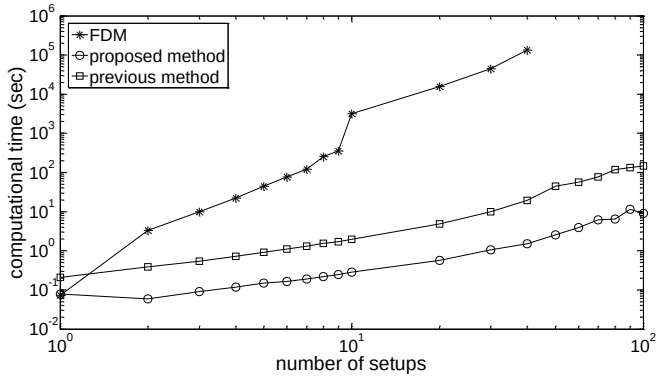

Figure 4 Computational time, multiple-setup data.

Figure 3 shows the computational time required for a single setup when the number of DOFs increases. It shows that the time required by the proposed method and the previous method are in the same order of magnitude, while the FDM requires a much longer period of time. Figure 4 compares the results for different number of setups. It can be seen that the proposed method requires less computational time than the other two methods. The FDM again requires more time for computation.

Although in reality the computational time highly depends on how the method is computer-coded, the results here suggest that the computational time required by the proposed method and the previous method are in the same order of magnitude, while using the FDM requires a substantially longer period of time. By leveraging on the compact and systematic expressions for handling the constrained Hessian, the proposed method requires much less programming effort compared to the existing methods.

3.5 Conclusion

This chapter has presented the application of the theory in Chapter 2 to calculate the Hessian of a function under constraints, which contributes to improving efficiency and effectiveness for uncertainty quantification in Bayesian OMA. Analytical expressions have been derived for calculating the posterior covariance matrix in ambient modal identification with single setup and multiple-setup data. Since the derivatives and constraints are handled separately, the Hessian can be derived in a systematic manner. Using specialised mapping functions, the derivation is significantly simplified, especially for the multiple-setup data case. The formulae for deriving the posterior covariance have been verified using synthetic data examples. The computational aspect has been investigated by comparing the required time with that in the previous

method and the FDM. Results show that the computational time required by the proposed method and previous method are in the same order of magnitude, while the FDM requires a substantially longer time. Leveraging on the existing single setup computer codes, the programming effort for multiple setups is significantly reduced. The merit of the proposed method lies in the systematic and simplified nature of the required programming effort.

Chapter 4 Uncertainty law (management)

4.1 Introduction

In ambient vibration tests, the (input) excitation to the structure is not measured, but is assumed to be statistically random. In the absence of loading information, the identification uncertainty of the modal parameters becomes significant. Being able to quantify uncertainty for a given data set alone does not provide much insight for understanding and controlling uncertainty. Multiple-setup ambient vibration test has been widely used in field testing of civil engineering structures for its economy and efficiency in implementation [14,15,49,69,129]. Different ways of allocating reference and roving sensors can yield different levels of uncertainty. It is desirable to know how identification uncertainty is related to test configuration. This has both scientific and practical significance, i.e., to discover the identification precision limit and provide guidance for the planning of vibration tests.

Bayesian modal identification provides a fundamental method to quantify identification uncertainty via the posterior covariance matrix. Due to the complications involved in calculating the uncertainty associated with modal parameters, it is unlikely to be able to express the exact dependence of the uncertainty in an explicit closed-form expression [91]. A study has shown that, when the data is assumed to be distributed as the likelihood function (i.e., no modelling error), the posterior covariance matrix is asymptotic to a deterministic quantity that depends on the 'information content' of data [60]. With sufficient data, the posterior covariance

matrix is asymptotically equal to the Fisher information matrix. This coincides with the tightest Cramér-Rao bound in classical statistics [94].

This chapter investigates the leading order behaviour of the posterior covariance matrix in multiple-setup OMA. The asymptotic form of the posterior covariance matrix is derived from the inverse of the FIM. A closed-form expression of the FIM is developed under small damping and high modal s/n ratio assumptions. Leveraging on the discovery of asymptotic decoupling, the dimension of the FIM is significantly reduced, which makes the inverse of the FIM algebraically manageable. This subsequently yields closed-form expressions of the leading order posterior c.o.v. of modal parameters.

For the ease of reading, the results are first presented. The relationship of the CRB with the posterior covariance matrix is then provided, followed by derivation of the posterior c.o.v. of modal parameters. The global mode shape c.o.v. is investigated and guidance for planning multiple setups is provided. Finally, the proposed theory is validated with synthetic, laboratory and field test data.

4.2 Outline of results

The posterior c.o.v.s of modal parameters in multiple-setup OMA developed in this work are outlined. The collection of the results is referred as the multiple-setup uncertainty law.

Posterior c.o.v.s for f_r, ζ_r, S_r and S_{e_r}

Suppose the data from a selected frequency band $(1\pm\kappa_r\zeta_r)f_r$ is used for modal identification in the r-th setup, where κ_r is the 'bandwidth factor' for setup r. The

choice of the bandwidth factor is a trade-off between identification precision and modelling error. Under long data asymptotics and small damping assumption, the posterior covariance matrix can be asymptotically derived. The results are summarised in Table 4 and detailed derivations are shown in section 4.4. Based on the findings in Table 4, the leading order of the squared posterior c.o.v. of f_r, ζ_r, S_r and S_{e_r} for setup r can then be expressed as

$$\delta_{f_r}^2 = \frac{\zeta_r}{2\pi N_c^{(r)} B_f^{(r)}} \qquad \delta_{\zeta_r}^2 = \frac{1}{2\pi\zeta_r N_c^{(r)} B_\zeta^{(r)}}$$
$$\delta_{S_r}^2 = \frac{1}{N_f^{(r)} B_S^{(r)}} \qquad \delta_{S_{e_r}}^2 = \frac{1}{(n_r - 1) N_f^{(r)}} \tag{104}$$

where

$$B_f^{(r)} = \frac{2}{\pi}(\tan^{-1}\kappa_r - \frac{\kappa_r}{\kappa_r^{\,2}+1})$$
$$B_\zeta^{(r)} = \frac{2}{\pi}\left[\tan^{-1}\kappa_r + \frac{\kappa_r}{\kappa_r^{\,2}+1} - \frac{2(\tan^{-1}\kappa_r)^2}{\kappa_r}\right] \tag{105}$$
$$B_S^{(r)} = 1 - 2(\tan^{-1}\kappa_r)^2 \kappa_r^{-1}(\tan^{-1}\kappa_r + \frac{\kappa_r}{\kappa_r^{\,2}+1})^{-1}$$

are 'data length factors' that only depend on κ_r; n_r is the number of measured DOFs in the r-th setup; $N_c^{(r)} = T_d^{(r)} f_r$ is the normalised data length, where $T_d^{(r)}$ is the data duration in the r-th setup; $N_f^{(r)} = 2\kappa_r\zeta_r N_c^{(r)}$ is the number of FFT ordinates in the selected frequency band in the r-th setup.

Posterior c.o.v. for global mode shape φ

The (squared) global mode shape c.o.v. $\delta_{\boldsymbol{\varphi}}^2$ is defined as the trace of the posterior global mode shape covariance matrix [130]. For sufficiently long data and small damping, it can be shown that

$$\delta_{\boldsymbol{\varphi}}^2 = \sum_{\substack{i=1;\, j=2;\\ i\neq j}}^{C_{n_s}^2} \frac{c_i c_j}{c_{ref}} (k_i^{-1} + k_j^{-1}) + \sum_{i=1}^{n_s} n_{rov}^{(i)} k_i^{-1} + (n_{ref} - 1)(\sum_{i=1}^{n_s} k_i)^{-1} \tag{106}$$

where

$k_i = N_c^{(i)} \nu_i^{-1} \zeta_i^{-1} \tan^{-1}(\kappa_i)$ is the 'data quality factor' of the i-th setup and $\nu_i = S_{e_i} / S_i$ is the 'noise-to-environment' (n/e) ratio; n_{ref} is the number of reference DOFs; $n_{rov}^{(i)}$ is the number of roving DOFs in the i-th setup; $C_{n_s}^2$ is the combination of two different numbers selected from 1 to n_s; c_i and c_j are the sum of the squared mode shape values at the roving locations in the i-th and j-th setup, respectively; c_{ref} is the sum of the squared mode shape values at the reference locations.

To explain c_i and c_{ref}, consider a nine-DOF structure comprising two reference DOFs, two roving DOFs in setup 1 and 2, and three roving DOFs in setup 3. The global mode shape can be simply constructed as

$$[\underbrace{\varphi_1 \quad \varphi_2}_{c_{ref}} \quad \underbrace{\varphi_3 \quad \varphi_4}_{c_1} \quad \underbrace{\varphi_5 \quad \varphi_6}_{c_2} \quad \underbrace{\varphi_7 \quad \varphi_8 \quad \varphi_9}_{c_3}]^T$$

reference DOFs; roving DOFs for setup 1; roving DOFs for setup 2; roving DOFs for setup 3

where c_{ref} and c_i for $i = 1, 2, 3$ are given by

$$c_{ref} = \varphi_1^2 + \varphi_2^2 \qquad c_1 = \varphi_3^2 + \varphi_4^2 \qquad c_2 = \varphi_5^2 + \varphi_6^2 \qquad c_3 = \varphi_7^2 + \varphi_8^2 + \varphi_9^2 \tag{107}$$

Formula (106) can be used to determine the squared global mode shape c.o.v., which reflects the uncertainty of the global mode shape incorporating information from multiple setups. It can be shown that $n_s = 1$ gives the same expression as that for single setup (see [91]). For multiple setups, the formula assumes $n_{ref} \neq 0$ and $n_{rov}^{(i)} \neq 0$ for $i = 1, ..., n_s$. The roving DOFs in each setup should not overlap and the reference DOFs should be fixed in all setups. The above assumptions are typical for multiple-setup field tests.

4.3 Connecting the Cramér-Rao bound and posterior covariance matrix

For globally identifiable problems, the posterior distribution of the modal parameters $\boldsymbol{\theta}$ for given data D can be approximated by a Gaussian distribution with covariance matrix $\hat{\mathbf{C}}$ that is given by the inverse of the Hessian of the NLLF [60], i.e.,

$$\hat{\mathbf{C}} = \left[\nabla_{\boldsymbol{\theta}}^2 L(D, \boldsymbol{\theta}) \Big|_{\boldsymbol{\theta}=\hat{\boldsymbol{\theta}}} \right]^{-1} \tag{108}$$

where $L(D, \boldsymbol{\theta})$ is the NLLF with given D. On the other hand, in classical statistics, one constructs a statistical estimator $\mathbf{G}(D)$ as a function of data D. When the data is assumed to be distributed as the likelihood function for some 'true' parameters, denoted by $\boldsymbol{\theta}_0$, the Cramér-Rao bound provides the smallest possible variance that can be achieved by any unbiased estimator [131]. That is

$$\mathrm{cov}[\mathbf{G}(D)\big|\boldsymbol{\theta}_0] \geq \mathbf{J}(\boldsymbol{\theta}_0)^{-1} \tag{109}$$

where $\mathrm{cov}[.]$ is the covariance matrix of $\mathbf{G}(D)$; $\mathbf{J}(\boldsymbol{\theta}_0)$ is the FIM and it is given by

$$\mathbf{J}(\boldsymbol{\theta}_0) = E\left[\nabla^2_{\boldsymbol{\theta}} L(D,\boldsymbol{\theta})\Big|_{\boldsymbol{\theta}=\boldsymbol{\theta}_0}\right] \tag{110}$$

where $E[.]$ denotes the expectation of the quantity inside the bracket.

With sufficient data and assuming no modelling error, it is possible to mathematically relate the posterior covariance matrix to the 'tightest' CRB through the FIM [92]. For a large sample size N, the leading order of the posterior covariance matrix is asymptotically given by:

$$\hat{\mathbf{C}} = \underbrace{\mathbf{J}(\boldsymbol{\theta}_0)^{-1}}_{\text{leading order}}\left[\mathbf{I} + O(N^{-1/2})\right] \qquad N \to \infty \tag{111}$$

where $\mathbf{I}$ is the identity matrix; $O(N^{-1/2})$ denotes that the remainder depends on data D and is of order $N^{-1/2}$.

By relating Bayesian and frequentist statistics, the leading order of the posterior covariance matrix can be derived from the inverse of the FIM. This is derived in the following.

4.4 Main derivations

Three main asymptotics are involved in the derivation of the uncertainty law of multiple setups, including long data asymptotics, small damping asymptotics and asymptotic decoupling. The long data assumption allows the FIM to be analytically derived, which is presented in Section 4.4.1. Considering small damping and high

modal s/n ratio, the FIM can be simplified into a closed-form expression (see Section 4.4.2). Leveraging on the asymptotic decoupling of modal parameters, the dimension of the inverse of the FIM is significantly reduced, which is shown in Section 4.4.3. The leading order uncertainty of f_r, ζ_r, S_r and S_{e_r} is derived from the inverse of the FIM, which is presented in Section 4.4.3.2. Despite the above developments, it is still difficult to obtain explicit and intuitive expression for the global mode shape uncertainty, since it involves the inverse of the sum of the FIM over different setups. By examining the special pattern of the eigenvalues of the FIM of the global mode shape, a closed-from expression of the global mode shape c.o.v. is derived, which is presented in Section 4.4.5.

4.4.1 Long data asymptotics

With sufficient data, the leading order of the posterior covariance matrix is asymptotically equal to the inverse of the FIM. In multiple setups, let $\boldsymbol{\theta}_r$ be the collection of the modal parameters in the r-th setup, i.e., $\boldsymbol{\theta}_r = \{f_r, \zeta_r, S_r, S_{e_r}, \mathbf{v}_r\}$, where $\mathbf{v}_r = \mathbf{L}_r \boldsymbol{\varphi}$ is the partial mode shape for the r-th setup; $\boldsymbol{\varphi}$ is the global mode shape and $\mathbf{L}_r$ is the selection matrix. Denote n_s as the number of setups.

Let $L_r^{(x,y)}$ denote the derivatives of the NLLF w.r.t variables x and y in $\boldsymbol{\theta}_r$ and evaluated at MPV for given FFT data $\{\mathcal{F}_k^{(r)}\}$. The latter is distributed as the likelihood function $p\left(\{\mathcal{F}_k^{(r)}\}\middle|\boldsymbol{\theta}\right)$. It can be shown that

$$\hat{L}_r^{(x,y)} = J_r^{(x,y)}(\boldsymbol{\theta}_r)\left[1+O(N_f{}^{-1/2})\right] \qquad \text{for } N_f \to \infty \tag{112}$$

where $J_r^{(x,y)}(\boldsymbol{\theta}_r)$ is the entry in the FIM that corresponds to a parameter pair (x, y) for the r-th setup. With sufficiently long data, $L_r^{(x,y)}$ is asymptotically given by $J_r^{(x,y)}(\boldsymbol{\theta}_r)$ for each setup.

Let $\boldsymbol{\theta} = \{f_r, \zeta_r, S_r, S_{e_r} : r = 1, ..., n_s;\ \boldsymbol{\varphi}\}$ be the collection of modal parameters from all the setups. Incorporating multiple-setup data, the NLLF w.r.t. $\boldsymbol{\theta}$ is given by

$$L^{(x,y)}(\boldsymbol{\theta}) = \sum_{r=1}^{n_s} L_r^{(x,y)}(\boldsymbol{\theta}_r) \tag{113}$$

The entire FIM w.r.t. $\boldsymbol{\theta}$ is then given by the sum of $J_{xy}{}^{(r)}$ over different setups, i.e.,

$$J_{xy} = \sum_r J_{xy}{}^{(r)} \tag{114}$$

Since the FFT data in each setup follows a zero-mean complex Gaussian distribution, as a standard result, the FIM is given by [132], i.e.,

$$J_{xy}{}^{(r)} = \sum_k \mathrm{tr}[\mathbf{E}_k{}^{(r)^{-1}} \mathbf{E}_k{}^{(r)(x)} \mathbf{E}_k{}^{(r)^{-1}} \mathbf{E}_k{}^{(r)(y)}] \tag{115}$$

where tr[.] denotes the trace of the quantity inside the brackets and the superscripts x and y denote the partial derivatives; $\mathbf{E}_k^{(r)}$ is the theoretical PSD matrix of the data, which is given by (93) (see Section 3.3.1), i.e.,

$$\mathbf{E}_k{}^{(r)} = \left(S_r \left\|\mathbf{v}_r\right\|^2\right) D_{k_r} \bar{\mathbf{v}}_r \bar{\mathbf{v}}_r{}^T + S_{e_r} \mathbf{I}_{n_r} \tag{116}$$

where $\bar{\mathbf{v}}_r = \left\|\mathbf{v}_r\right\|^{-1} \mathbf{v}_r$ is the normalised partial mode shape; D_k is the dynamic amplification factor given by (65).

By treating $S_r \|\mathbf{v}_r\|^2$ as a single term, the expression in (116) for the r-th setup is the same as in the single setup case. The derivatives used in deriving the uncertainty law of single setup can be used for multiple setups.

Terms w.r.t $\{f_r, \zeta_r, S_r, S_{e_r}\}$

Using the eigenvector representation for $\mathbf{E}_k^{(r)}$, it can be shown that

$$\mathbf{E}_k^{(r)^{-1}} = (S_r \|\mathbf{v}_r\|^2 D_{k_r} + S_{e_r})^{-1} \mathbf{b}_1 \mathbf{b}_1^T + S_{e_r}^{-1} \sum_{i=2}^{n} \mathbf{b}_i \mathbf{b}_i^T \tag{117}$$

$$\mathbf{E}_k^{(r)^{(x)}} = (S_r \|\mathbf{v}_r\|^2 D_{k_r} + S_{e_r})^{(x)} \mathbf{b}_1 \mathbf{b}_1^T + S_{e_r}^{(x)} \sum_{i=2}^{n} \mathbf{b}_i \mathbf{b}_i^T \tag{118}$$

where $\{\mathbf{b}_i\}_{i=1}^n$ is an orthonormal basis in R^n with $\mathbf{b}_1 = \bar{\mathbf{v}}_r$ and $\mathbf{I}_{n_r} = \sum_{i=1}^{n} \mathbf{b}_i \mathbf{b}_i^T$. The superscript (x) denotes the differentiation of $\mathbf{E}_k^{(r)}$ w.r.t x from $\{f_r, \zeta_r, S_r, S_{e_r}\}$.

Based on (117) and (118), it can be shown that

$$\begin{aligned} \mathbf{E}_k^{(r)^{-1}} \mathbf{E}_k^{(r)^{(x)}} \mathbf{E}_k^{(r)^{-1}} \mathbf{E}_k^{(r)^{(y)}} = & \sum_k \frac{(S_r \|\mathbf{v}_r\|^2 D_{k_r} + S_{e_r})^{(x)} (S_r \|\mathbf{v}_r\|^2 D_{k_r} + S_{e_r})^{(y)}}{(S_r \|\mathbf{v}_r\|^2 D_{k_r} + S_{e_r})^2} \mathbf{b}_1 \mathbf{b}_1^T \\ & + \frac{S_{e_r}^{(x)} S_{e_r}^{(y)}}{S_{e_r}^2} \sum_{i=2}^{n} \mathbf{b}_i \mathbf{b}_i^T \end{aligned} \tag{119}$$

Taking the trace and summing over r and k gives

$$J_{xy} = \sum_r \left\{ \begin{array}{l} \displaystyle\sum_k \frac{(S_r \|\mathbf{v}_r\|^2 D_{k_r} + S_{e_r})^{(x)} (S_r \|\mathbf{v}_r\|^2 D_{k_r} + S_{e_r})^{(y)}}{(S_r \|\mathbf{v}_r\|^2 D_{k_r} + S_{e_r})^2} \\ \\ \displaystyle + (n_r - 1) N_f^{(r)} \frac{S_{e_r}^{(x)} S_{e_r}^{(y)}}{S_{e_r}^2} \end{array} \right\} \tag{120}$$

Denote $e_k^{(r)}$ as

$$e_k^{(r)} = \frac{S_{e_r}}{S_r \|\mathbf{v}_r\|^2 D_{k_r}} \tag{121}$$

Differentiating (120) w.r.t. x and y from $\{f_r, \zeta_r, S_r, S_{e_r}\}$ gives

$$J^{(f_r,f_r)} = \sum_k \frac{S_r{}^2 \|\mathbf{v}_r\|^4 D_{k_r}{}^{(f_r)} D_{k_r}{}^{(f_r)}}{(S_r \|\mathbf{v}_r\|^2 D_{k_r} + S_{e_r})^2} = \sum_k \frac{D_{k_r}^2 (D_{k_r}^{-1})^{(f_r)} (D_{k_r}^{-1})^{(f_r)}}{(1+e_k^{(r)})^2} \tag{122}$$

$$J^{(f_r,\zeta_r)} = \sum_k \frac{S_r{}^2 \|\mathbf{v}_r\|^4 D_{k_r}{}^{(f_r)} D_{k_r}{}^{(\zeta_r)}}{(S_r \|\mathbf{v}_r\|^2 D_{k_r} + S_{e_r})^2} = \sum_k \frac{D_{kr}^2 (D_{k_r}^{-1})^{(f_r)} (D_{k_r}^{-1})^{(\zeta_r)}}{(1+e_k^{(r)})^2} \tag{123}$$

$$J^{(f_r,S_r)} = \sum_k \frac{S_r \|\mathbf{v}_r\|^4 D_{k_r} D_{k_r}{}^{(f_r)}}{(S_r \|\mathbf{v}_r\|^2 D_{k_r} + S_{e_r})^2} = -S_r{}^{-1} \sum_k \frac{D_{k_r} (D_{k_r}^{-1})^{(f_r)}}{(1+e_k^{(r)})^2} \tag{124}$$

$$J^{(f_r,S_{e_r})} = \sum_k \frac{S_r \|\mathbf{v}_r\|^2 D_{k_r}{}^{(f_r)}}{(S_r \|\mathbf{v}_r\|^2 D_{k_r} + S_{e_r})^2} = -S_{er}{}^{-1} \sum_k \frac{D_{k_r} (D_{k_r}^{-1})^{(f_r)} e_k^{(r)}}{(1+e_k^{(r)})^2} \tag{125}$$

$$J^{(\zeta_r,\zeta_r)} = \sum_k \frac{S_r{}^2 \|\mathbf{v}_r\|^4 D_{k_r}{}^{(\zeta_r)} D_{k_r}{}^{(\zeta_r)}}{(S_r \|\mathbf{v}_r\|^2 D_{k_r} + S_{e_r})^2} = \sum_k \frac{D_{k_r}^2 (D_{k_r}^{-1})^{(\zeta_r)} (D_{k_r}^{-1})^{(\zeta_r)}}{(1+e_k^{(r)})^2} \tag{126}$$

$$J^{(\zeta_r,S_r)} = \sum_k \frac{S_r \|\mathbf{v}_r\|^4 D_{k_r} D_{k_r}{}^{(\zeta_r)}}{(S_r \|\mathbf{v}_r\|^2 D_{k_r} + S_{e_r})^2} = -S_r{}^{-1} \sum_k \frac{D_{k_r} (D_{k_r}^{-1})^{(\zeta_r)}}{(1+e_k^{(r)})^2} \tag{127}$$

$$J^{(\zeta_r,S_{e_r})} = \sum_k \frac{S_r \|\mathbf{v}_r\|^2 D_{k_r}{}^{(\zeta_r)}}{(S_r \|\mathbf{v}_r\|^2 D_{k_r} + S_{e_r})^2} = -S_{e_r}{}^{-1} \sum_k \frac{D_{k_r} (D_{k_r}^{-1})^{(\zeta_r)} e_k^{(r)}}{(1+e_k^{(r)})^2} \tag{128}$$

$$J^{(S_r,S_r)} = \sum_k \frac{\|\mathbf{v}_r\|^4 D_{k_r}^2}{(S_r \|\mathbf{v}_r\|^2 D_{k_r} + S_{e_r})^2} = S_r{}^{-2} \sum_k \frac{1}{(1+e_k^{(r)})^2} \tag{129}$$

$$J^{(S_r,S_{e_r})}=\sum_k \frac{\|\mathbf{v}_r\|^2 D_{k_r}}{(S_r\|\mathbf{v}_r\|^2 D_{k_r}+S_{e_r})^2}=S_r{}^{-1}S_{e_r}{}^{-1}\sum_k \frac{e_k{}^{(r)}}{(1+e_k{}^{(r)})^2} \tag{130}$$

$$\begin{aligned} J^{(S_{e_r},S_{e_r})} &= \sum_k \frac{1}{(S_r\|\mathbf{v}_r\|^2 D_{k_r}+S_{e_r})^2}+(n_r-1)N_f^{(r)}S_{e_r}{}^{-2} \\ &= S_{e_r}{}^{-2}\left[\sum_k \frac{(e_k{}^{(r)})^2}{(1+e_k{}^{(r)})^2}+(n_r-1)N_f^{(r)}\right] \end{aligned} \tag{131}$$

Terms w.r.t. global mode shape φ

Recall $\mathbf{E}_k{}^{(r)}$ from the previous section and substitute the partial mode shape $\mathbf{v}_r$ by $\mathbf{L}_r\boldsymbol{\varphi}$. Considering the norm constraint applied on the global mode shape, $\boldsymbol{\varphi}$ is replaced by $\bar{\boldsymbol{\varphi}}=\boldsymbol{\varphi}/\|\boldsymbol{\varphi}\|$. One can then write $\mathbf{E}_k{}^{(r)}$ as

$$\mathbf{E}_k{}^{(r)}=S_r D_{k_r}\mathbf{L}_r\bar{\boldsymbol{\varphi}}\bar{\boldsymbol{\varphi}}^T\mathbf{L}_r^T+S_{e_r}\mathbf{I}_{n_r} \tag{132}$$

Let $\boldsymbol{\varphi}=[\varphi_1,...,\varphi_n]^T$ and $\mathbf{e}_i$ be an $n\times 1$ vector with the i-th entry as the only non-zero entry that is equal to one. Then it can be shown that

$$\bar{\boldsymbol{\varphi}}^{(\varphi_i)}=(\nabla\bar{\boldsymbol{\varphi}})\mathbf{e}_i \qquad \nabla\bar{\boldsymbol{\varphi}}=\left[\frac{\partial\bar{\boldsymbol{\varphi}}}{\partial\varphi_1} \quad \cdots \quad \frac{\partial\bar{\boldsymbol{\varphi}}}{\partial\varphi_n}\right]=\mathbf{I}_n-\bar{\boldsymbol{\varphi}}\bar{\boldsymbol{\varphi}}^T \qquad (\|\boldsymbol{\varphi}\|=1) \tag{133}$$

Differentiating $\mathbf{E}_k{}^{(r)}$ w.r.t. φ_i $(i=1,...,n)$ gives

$$\mathbf{E}_k{}^{(r)(\varphi_i)}=S_r D_{k_r}(\mathbf{L}_r\nabla\bar{\boldsymbol{\varphi}}\mathbf{e}_i\bar{\boldsymbol{\varphi}}^T\mathbf{L}_r^T+\mathbf{L}_r\bar{\boldsymbol{\varphi}}\mathbf{e}_i{}^T\nabla\bar{\boldsymbol{\varphi}}^T\mathbf{L}_r^T)=S_r D_{k_r}(\mathbf{A}_i^{(r)T}+\mathbf{A}_i^{(r)}) \tag{134}$$

where

$$\mathbf{A}_i^{(r)}=\mathbf{L}_r\bar{\boldsymbol{\varphi}}\mathbf{e}_i{}^T\nabla\bar{\boldsymbol{\varphi}}^T\mathbf{L}_r^T \tag{135}$$

Because of the special structure of $\mathbf{A}_i^{(r)}$ and $\bar{\mathbf{v}}_r$, it can be shown that

$$\begin{aligned}
&\bar{\mathbf{v}}_r\bar{\mathbf{v}}_r{}^T\mathbf{A}_i^{(r)} = \mathbf{A}_i^{(r)} && \mathbf{A}_i^{(r)T}\bar{\mathbf{v}}_r\bar{\mathbf{v}}_r{}^T = \mathbf{A}_i^{(r)T}\\
&\mathbf{A}_i^{(r)}\mathbf{A}_j^{(r)} = a_i\mathbf{A}_j^{(r)} && \mathbf{A}_i^{(r)T}\mathbf{A}_j^{(r)T} = a_j\mathbf{A}_i^{(r)T}\\
&\mathbf{A}_i^{(r)}\mathbf{A}_j^{(r)T} = b\mathbf{v}_r\mathbf{v}_r{}^T && \mathbf{A}_i^{(r)T}\mathbf{A}_j^{(r)} = \|\mathbf{v}_r\|^2\mathbf{B}\\
&\bar{\mathbf{v}}_r\bar{\mathbf{v}}_r{}^T\mathbf{A}_i^{(r)T} = \mathbf{A}_i^{(r)}\bar{\mathbf{v}}_r\bar{\mathbf{v}}_r{}^T = a_i\bar{\mathbf{v}}_r\bar{\mathbf{v}}_r{}^T
\end{aligned} \tag{136}$$

where $\mathbf{B} = \mathbf{L}_r\nabla\bar{\boldsymbol{\varphi}}\mathbf{e}_i\mathbf{e}_j{}^T\nabla\bar{\boldsymbol{\varphi}}^T\mathbf{L}_r^T$ is an $n_r \times n_r$ matrix; $a_i = \mathbf{e}_i{}^T\nabla\bar{\boldsymbol{\varphi}}^T\mathbf{L}_r^T\mathbf{L}_r\bar{\boldsymbol{\varphi}}$ and $b = \mathbf{e}_j{}^T\nabla\bar{\boldsymbol{\varphi}}^T\mathbf{L}_r^T\mathbf{L}_r\nabla\bar{\boldsymbol{\varphi}}\mathbf{e}_i$ are scalars.

Making use of $e_k^{(r)}$, (117) can be rewritten as:

$$\mathbf{E}_k^{(r)^{-1}} = S_{e_r}{}^{-1}[\mathbf{I}_{n_r} - (1+e_k^{(r)})^{-1}\bar{\mathbf{v}}_r\bar{\mathbf{v}}_r^T] \tag{137}$$

It can be shown that

$$\mathbf{E}_k^{(r)^{-1}}\mathbf{E}_k^{(r)^{(\varphi_1)}} = \|\mathbf{v}_r\|^{-2}\left\{(1+e_k^{(r)})^{-1}\mathbf{A}_i + e_k^{(r)-1}\mathbf{A}_i{}^T - e_k^{(r)-1}(1+e_k^{(r)})^{-1}a_i\bar{\mathbf{v}}_r\bar{\mathbf{v}}_r{}^T\right\} \tag{138}$$

$$\mathbf{E}_k^{(r)^{-1}}\mathbf{E}_k^{(r)^{(x)}} = S_{e_r}{}^{-1}\left[e_k^{(r)}(1+e_k^{(r)})^{-1}(S_rD_{k_r} + S_{e_r})^{(x)}\bar{\mathbf{v}}_r\bar{\mathbf{v}}_r{}^T + S_{e_r}{}^{(x)}(\mathbf{I}_r - \bar{\mathbf{v}}_r\bar{\mathbf{v}}_r{}^T)\right] \tag{139}$$

$$\begin{aligned}
&\mathbf{E}_k^{(r)^{-1}}\mathbf{E}_k^{(r)^{(x)}}\mathbf{E}_k^{(r)^{-1}}\mathbf{E}_k^{(r)^{(\varphi_1)}}\\
&= \|\mathbf{v}_r\|^{-2}\,S_{e_r}{}^{-1}\begin{bmatrix}(S_rD_{k_r} + S_{e_r})^{(x)}e_k^{(r)}(1+e_k^{(r)})^{-2}(\mathbf{A}_i + a_i\bar{\mathbf{v}}_r\bar{\mathbf{v}}_r{}^T)\\ +S_{e_r}{}^{(x)}e_k^{(r)-1}(\mathbf{A}_i{}^T - a_i\bar{\mathbf{v}}_r\bar{\mathbf{v}}_r{}^T)\end{bmatrix}
\end{aligned} \tag{140}$$

$$\begin{aligned}&\mathbf{E}_k{}^{(r)^{-1}}\mathbf{E}_k{}^{(r)^{(\varphi_i)}}\mathbf{E}_k{}^{(r)^{-1}}\mathbf{E}_k{}^{(r)^{(\varphi_j)}}\\&=\|\mathbf{v}_r\|^{-4}\left\{\begin{array}{l}(e_k{}^{(r)}-1)e_k{}^{(r)^{-1}}(1+e_k{}^{(r)})^{-2}a_i\mathbf{A}_j+e_k{}^{(r)^{-1}}(1+e_k{}^{(r)})^{-1}a_j\mathbf{A}_i{}^T\\+e_k{}^{(r)^{-1}}(1+e_k{}^{(r)})^{-1}\|\mathbf{v}_r\|^2 b\mathbf{I}_r+e_k{}^{(r)^{-1}}(1+e_k{}^{(r)})^{-1}\|\mathbf{v}_r\|^2\mathbf{B}\\-2e_k{}^{(r)^{-1}}(1+e_k{}^{(r)})^{-2}a_i a_j\bar{\mathbf{v}}_r\bar{\mathbf{v}}_r{}^T\end{array}\right\}\end{aligned}\tag{141}$$

Taking the trace of (140) and (141), noting that $\mathrm{tr}(\bar{\mathbf{v}}_r\bar{\mathbf{v}}_r{}^T)=1$, $\mathrm{tr}(\mathbf{A}_i)=a_i$ and $\mathrm{tr}(\mathbf{B})=b$, one obtains

$$\begin{aligned}J^{(r)^{(x)(\varphi_i)}}&=\sum_k\mathrm{tr}(\mathbf{E}_k{}^{(r)^{-1}}\mathbf{E}_k{}^{(r)^{(x)}}\mathbf{E}_k{}^{(r)^{-1}}\mathbf{E}_k{}^{(r)^{(\varphi_i)}})\\&=2\|\mathbf{v}_r\|^{-2}S_{e_r}{}^{-1}\sum_k e_k{}^{(r)}(1+e_k{}^{(r)})^{-2}(S_r\|\mathbf{v}_r\|^2 D_{k_r}+S_{e_r})^{(x)}a_i\end{aligned}\tag{142}$$

and

$$\begin{aligned}J^{(r)^{(\varphi_i)(\varphi_j)}}&=\sum_k\mathrm{tr}(\mathbf{E}_k{}^{(r)^{-1}}\mathbf{E}_k{}^{(r)^{(\varphi_i)}}\mathbf{E}_k{}^{(r)^{-1}}\mathbf{E}_k{}^{(r)^{(\varphi_j)}})\\&=2\|\mathbf{v}_r\|^{-2}\sum_k\left\{e_k{}^{(r)^{-1}}(e_k{}^{(r)}+1)^{-1}\left[(e_k{}^{(r)}-1)(e_k{}^{(r)}+1)^{-1}\|\mathbf{v}_r\|^{-2}a_i a_j+b\right]\right\}\end{aligned}\tag{143}$$

Assembling $J^{(r)^{(x\boldsymbol{\varphi})}}$ and $J^{(\boldsymbol{\varphi}\boldsymbol{\varphi})}$ from (142) and (143) w.r.t $[\varphi_1,...,\varphi_n]^T$ gives

$$J^{(r)^{(x\boldsymbol{\varphi})}}=2S_{e_r}{}^{-1}\|\mathbf{v}_r\|^{-2}\sum_k\left[\frac{e_k{}^{(r)}(S_r\|\mathbf{v}_r\|^2 D_{k_r}+S_{e_r})^{(x)}}{(e_k{}^{(r)}+1)^2}\right]\bar{\boldsymbol{\varphi}}^T\mathbf{L}_r{}^T\mathbf{L}_r(\mathbf{I}_n-\bar{\boldsymbol{\varphi}}\bar{\boldsymbol{\varphi}}^T)\tag{144}$$

where x is from $\left\{f_r,\zeta_r,S_r,S_{e_r}\right\}$, and

$$J^{(\boldsymbol{\varphi}\boldsymbol{\varphi})}=\sum_r\sum_k\left\{\frac{2(\mathbf{I}_n-\bar{\boldsymbol{\varphi}}\bar{\boldsymbol{\varphi}}^T)\mathbf{L}_r{}^T\left[\mathbf{I}_{n_r}-\frac{(1-e_k{}^{(r)})}{(1+e_k{}^{(r)})}\bar{\mathbf{v}}_r\bar{\mathbf{v}}_r{}^T\right]\mathbf{L}_r(\mathbf{I}_n-\bar{\boldsymbol{\varphi}}\bar{\boldsymbol{\varphi}}^T)}{\|\mathbf{v}_r\|^2(e_k{}^{(r)}+1)e_k{}^{(r)}}\right\}\tag{145}$$

Now the entries of the FIM can be assembled from the expression of its entries derived above. The results are summarised in Table 1.

4.4.2 Small damping asymptotics

Terms w.r.t. $\{f_r,\ \zeta_r,\ S_r,\ S_{e_r}\}$

The asymptotic expression of J_{xy} from Table 1 involves discrete sums over k, which can be further simplified with small damping assumption. Applying the Taylor approximation $(1+e_k^{(r)})^{-1} \approx 1-e_k$ and $(1+e_k^{(r)})^{-2} \approx 1-2e_k$, the leading order of the sums can be written in the standard form $\sum_k D_k^a (\beta_k - 1)^b \beta_k^c$, where a, b and c are integers. Under small damping assumption ($\zeta \to 0$), the results of the discrete sum from [91] can be directly used for deriving the asymptotic closed-form expressions of J_{xy}. The results are summarised in Table 2.

Table 1 Summary of J_{xy} for parameters in the r-th setup and global mode shape; $N_f^{(r)} \to \infty$; $\|\boldsymbol{\varphi}\| = 1$.

	$x = f_r,\ \zeta_r$	S_r	S_{e_r}	$\boldsymbol{\varphi}$
$y = f_r, \zeta_r$	$\sum_k \frac{D_{k_r}^{\ 2}(D_{k_r}^{-1})^{(x)}(D_{k_r}^{-1})^{(y)}}{(1+e_k^{(r)})^2}$	$(-S_r)^{-1}\sum_k \frac{D_{k_r}(D_{k_r}^{\ -1})^{(y)}}{(1+e_k^{(r)})^2}$	$(-S_{e_r})^{-1}\sum_k \frac{D_{k_r}e_k^{(r)}(D_{k_r}^{-1})^{(y)}}{(1+e_k^{(r)})^2}$	$-2\|\mathbf{v}_r\|^{-2}\sum_k \frac{D_{k_r}(D_{k_r}^{\ -1})^{(y)}}{(1+e_k^{(r)})^2}\bar{\boldsymbol{\varphi}}^T\mathbf{L}_r^{\ T}\mathbf{L}_r(\mathbf{I}_n - \bar{\boldsymbol{\varphi}}\bar{\boldsymbol{\varphi}}^T)$
S_r		$(S_r)^{-2}\sum_k (1+e_k^{(r)})^{-2}$	$S_r^{\ -1}S_{e_r}^{\ -1}\sum_k \frac{e_k^{(r)}}{(1+e_k^{(r)})^2}$	$2\|\mathbf{v}_r\|^{-2}(S_r)^{-1}\sum_k \frac{1}{(1+e_k^{(r)})^2}\bar{\boldsymbol{\varphi}}^T\mathbf{L}_r^{\ T}\mathbf{L}_r(\mathbf{I}_n - \bar{\boldsymbol{\varphi}}\bar{\boldsymbol{\varphi}}^T)$
S_{er}			$S_{e_r}^{\ -2}\left[\sum_k \frac{\left(e_k^{(r)}\right)^2}{(1+e_k^{(r)})^2} + (n_r - 1)N_f^{(r)}\right]$	$2\|\mathbf{v}_r\|^{-2}S_{e_r}^{\ -1}\sum_k \frac{e_k^{(r)}}{(1+e_k^{(r)})^2}\ \bar{\boldsymbol{\varphi}}^T\mathbf{L}_r^{\ T}\mathbf{L}_r(\mathbf{I}_n - \bar{\boldsymbol{\varphi}}\bar{\boldsymbol{\varphi}}^T)$
$\boldsymbol{\varphi}$	sym.			$\sum_r\sum_k \left\{\frac{2(\mathbf{I}_n - \bar{\boldsymbol{\varphi}}\bar{\boldsymbol{\varphi}}^T)\mathbf{L}_r^{\ T}\left[\mathbf{I}_{n_r} - \frac{(1-e_k^{(r)})}{(1+e_k^{(r)})}\bar{\mathbf{v}}_r\bar{\mathbf{v}}_r^{\ T}\right]\mathbf{L}_r(\mathbf{I}_n - \bar{\boldsymbol{\varphi}}\bar{\boldsymbol{\varphi}}^T)}{\|\mathbf{v}_r\|^2(e_k^{(r)}+1)e_k^{(r)}}\right\}$

Table 2 Leading order of J_{xy} for parameters in the r-th setup and global mode shape; $N_f^{(r)} \to \infty$; $\zeta \to 0$; $\|\boldsymbol{\varphi}\| = 1$.

	$x = f_r$	ζ_r	S_r	S_{e_r}	$\boldsymbol{\varphi}$
$y = f_r$	$\frac{4N_c^{(r)}}{f_r^{\,2}\zeta_r}\left(\tan^{-1}\kappa_r - \frac{\kappa_r}{\kappa_r^2+1}\right)$	$\frac{4N_c^{(r)}}{f_r}\left(\tan^{-1}\kappa_r + \frac{2\kappa_r^3+\kappa_r}{(\kappa_r+1)^2}\right)$	$-\frac{2N_c^{(r)}\zeta_r}{f_r S_r}\left(2\tan^{-1}\kappa_r + \frac{\kappa_r^3}{\kappa_r^2+1}\right)$	$-\frac{8N_c^{(r)}\zeta_r^{\,3}}{3f_r S_r}(7\kappa_r^3+6\kappa_r)$	$O(N_f^{1/2})$
ζ_r		$\frac{4N_c^{(r)}}{\zeta_r}\left(\tan^{-1}\kappa_r + \frac{\kappa_r}{\kappa_r^2+1}\right)$	$-\frac{4N_c^{(r)}}{S_r}\tan^{-1}\kappa_r$	$-\frac{16N_c^{(r)}\zeta_r^{\,2}\kappa_r}{S_r}$	$O(N_f^{1/2})$
S_r			$\frac{N_f^{(r)}}{S_r^{\,2}}$	$\frac{8N_c^{(r)}\zeta_r^{\,3}}{3S_r^{\,2}}(\kappa_r^3+3\kappa_r)$	$O(N_f^{1/2})$
S_{e_r}				$\frac{(n_r-1)N_f^{(r)}}{S_{e_r}^{\,2}}$	$O(N_f^{1/2})$
$\boldsymbol{\varphi}$	sym.				$\sum_r \frac{N_c^{(r)}\tan^{-1}\kappa_r}{\nu_r\zeta_r}\mathbf{L}_r^{\,T}(\mathbf{I}_{n_r} - \bar{\mathbf{v}}_r\bar{\mathbf{v}}_r^{\,T})\mathbf{L}_r$

Terms w.r.t. global mode shape φ

Applying the Taylor approximation $(1+e_k^{(r)})^{-1} \approx 1$ and further taking $(1-e_k^{(r)})(1+e_k^{(r)})^{-1} \approx 1$, term $J^{(\varphi\varphi)}$ can be simplified to

$$\begin{aligned} J^{(\varphi\varphi)} &= \sum_r \sum_k \left\{ \frac{2(\mathbf{I}_n - \bar{\boldsymbol{\varphi}}\bar{\boldsymbol{\varphi}}^T)\mathbf{L}_r{}^T \left[\mathbf{I}_{n_r} - \frac{(1-e_k^{(r)})}{(1+e_k^{(r)})} \bar{\mathbf{v}}_r \bar{\mathbf{v}}_r{}^T \right] \mathbf{L}_r (\mathbf{I}_n - \bar{\boldsymbol{\varphi}}\bar{\boldsymbol{\varphi}}^T)}{\|\mathbf{v}_r\|^2 (e_k^{(r)}+1) e_k^{(r)}} \right\} \\ &\approx \sum_r \sum_k \left\{ 2\|\mathbf{v}_r\|^{-2} e_k^{(r)^{-1}} (\mathbf{I}_n - \bar{\boldsymbol{\varphi}}\bar{\boldsymbol{\varphi}}^T)\mathbf{L}_r{}^T \left[\mathbf{I}_{n_r} - \bar{\mathbf{v}}_r \bar{\mathbf{v}}_r{}^T \right] \mathbf{L}_r (\mathbf{I}_n - \bar{\boldsymbol{\varphi}}\bar{\boldsymbol{\varphi}}^T) \right\} \\ &= \sum_r \sum_k \left\{ \frac{2D_{k_r}}{\nu_r} (\mathbf{I}_n - \bar{\boldsymbol{\varphi}}\bar{\boldsymbol{\varphi}}^T)\mathbf{L}_r{}^T \left[\mathbf{I}_{n_r} - \bar{\mathbf{v}}_r \bar{\mathbf{v}}_r{}^T \right] \mathbf{L}_r (\mathbf{I}_n - \bar{\boldsymbol{\varphi}}\bar{\boldsymbol{\varphi}}^T) \right\} \\ &= \sum_r \sum_k \left[\frac{2D_{k_r}}{\nu_r} \mathbf{L}_r{}^T (\mathbf{I}_{n_r} - \bar{\mathbf{v}}_r \bar{\mathbf{v}}_r{}^T) \mathbf{L}_r \right] \end{aligned} \tag{146}$$

The discrete sum of D_{k_r} over k is asymptotically given by [91]

$$\sum_k D_{k_r} \approx \frac{N_c^{(r)}}{2\zeta_r} \tan^{-1} \kappa_r \tag{147}$$

Substituting (147) into (146), $J^{(\varphi\varphi)}$ can then be rewritten as

$$J^{(\varphi\varphi)} = \sum_r \frac{N_c{}^{(r)} \tan^{-1} \kappa_r}{\nu_r \zeta_r} \mathbf{L}_r{}^T (\mathbf{I}_{n_r} - \bar{\mathbf{v}}_r \bar{\mathbf{v}}_r{}^T) \mathbf{L}_r \tag{148}$$

4.4.3 Parameter asymptotic decoupling

Deriving the posterior covariance matrix requires the inverse of the FIM. It can be analytically intractable when directly inverting the entire FIM. Alternatively, if some parameters are asymptotically 'decoupled' from the remaining parameters, the dimension of the inverse can be significantly reduced. In this section, the parameter

decoupling behaviour is investigated for scalar parameters and vector parameters, respectively. Results in terms of the order of magnitude are summarised in Table 3.

4.4.3.1 Scalar parameter

A scalar parameter θ_i is said to be asymptotically decoupled from θ_j if the cross-sensitivity coefficient

$$q_{\theta_i\theta_j} = \frac{J^{(\theta_i\theta_j)}}{[J^{(\theta_i\theta_i)}]^{1/2}[J^{(\theta_j\theta_j)}]^{1/2}} \tag{149}$$

is small compared to 1, i.e., $q_{\theta_i\theta_j} \ll 1$.

If θ_i can be asymptotically decoupled from the remaining parameters, the leading order posterior variance w.r.t θ_i is simply given by $1/J^{(\theta_i\theta_i)}$. To prove this, let the FIM be denoted by

$$J = diag\left[\{\sqrt{J^{(\theta_i\theta_i)}}\}_{i=1}^{n_\theta}\right] \mathbf{Q}\ diag\left[\{\sqrt{J^{(\theta_i\theta_i)}}\}_{i=1}^{n_\theta}\right] \tag{150}$$

where $\mathbf{Q}$ is a sensitivity matrix with the (i, j)-entry being $q_{\theta_i\theta_j}$ and the diagonals being ones. The inverse of J can then be expressed as

$$J^{-1} = diag\left[\{1/\sqrt{J^{(\theta_i\theta_i)}}\}_{i=1}^{n_\theta}\right] \mathbf{Q}^{-1}\ diag\left[\{1/\sqrt{J^{(\theta_i\theta_i)}}\}_{i=1}^{n_\theta}\right] \tag{151}$$

Without loss of generality, consider the cross-sensitivity of θ_1 with the remaining parameters to be small, i.e., $q_{\theta_1\theta_j} \ll 1$ for all $j \neq 1$. The matrix $\mathbf{Q}$ can then be written as

$$\mathbf{Q} = \begin{bmatrix} 1 & \mathbf{q}_{\theta_1\theta_j}{}^T \\ \mathbf{q}_{\theta_1\theta_j} & \mathbf{V} \end{bmatrix} \tag{152}$$

where $\mathbf{q}_{\theta_1\theta_j}$ is a vector of collection $\{q_{\theta_1\theta_j}\}_{j=2}^{n_\theta}$; $\mathbf{V}$ is the remaining sensitivity matrix that excludes the terms associated with θ_1. Since $\mathbf{q}_{\theta_1\theta_j}$ is small, $\mathbf{Q}$ can be treated as a block diagonal matrix and its inverse is given by

$$\mathbf{Q}^{-1} \approx \begin{bmatrix} 1 & \\ & \mathbf{V}^{-1} \end{bmatrix} \tag{153}$$

The inverse of J can then be expressed as

$$J^{-1} \approx diag\left[\{1/\sqrt{J^{(\theta_i\theta_i)}}\}_{i=1}^{n_\theta}\right] \begin{bmatrix} 1 & \\ & \mathbf{V}^{-1} \end{bmatrix} diag\left[\{1/\sqrt{J^{(\theta_i\theta_i)}}\}_{i=1}^{n_\theta}\right] \tag{154}$$

and so $\left(J^{\theta_1\theta_i}\right)^{-1} \approx 1/J^{(\theta_1\theta_i)}$.

The cross-sensitivity coefficients w.r.t $\{f_r, \zeta_r, S_r, S_{e_r}\}$ are summarised in Table 3 in terms of their orders of magnitude. Under small damping assumption, $\{f_r, S_{e_r}\}$ can be asymptotically decoupled from the remaining parameters; while ζ_r and S_r remain correlated. The dimension of the inverse has now been significant reduced, so that it is possible to derive the leading order of the posterior covariance w.r.t. $\{f_r, \zeta_r, S_r, S_{e_r}\}$.

Table 3 Leading order sensitivity coefficients q_{xy} for parameters in the r-th setup and global mode shape.

	$x = f_r$	ζ_r	S_r	S_{e_r}	$\boldsymbol{\varphi}$
$y = f_r$	1	$O(\zeta)$	$O(\kappa^{1/2}\zeta)$	$O(\nu\kappa^{5/2}\zeta^3 n^{-1/2})$	$O(N_f^{-1/2})$
ζ_r		1	$O(\kappa^{-1/2})$	$O(\nu\kappa^{1/2}\zeta^2 n^{-1/2})$	$O(N_f^{-1/2})$
S_r			1	$O(\nu\kappa^{1/2}\zeta^2 n^{-1/2})$	$O(N_f^{-1/2})$
S_{e_r}				1	$O(N_f^{-1/2})$
$\boldsymbol{\varphi}$	sym.				1

Table 4 Leading order posterior statistics for parameters in the r-th setup and global mode shape; $N_f^{(r)} \to \infty$; $\zeta \to 0$.

	$x = f_r$	ζ_r	S_r	S_{e_r}	$\boldsymbol{\varphi}$
$y = f_r$	$\dfrac{f_r^{\,2}\zeta_r}{4N_c^{(r)}}\left(\tan^{-1}\kappa_r - \dfrac{\kappa_r}{\kappa_r^2+1}\right)^{-1}$	$O(\zeta)$	$O(\kappa_r^{1/2}\zeta)$	$O(\nu\kappa_r^{5/2}\zeta^3 n^{-1/2})$	$O(N_f^{1/2})$
ζ_r		$\dfrac{\zeta_r}{4N_c^{(r)}}\left(\tan^{-1}\kappa_r + \dfrac{\kappa_r}{\kappa_r^2+1} - \dfrac{2(\tan^{-1}\kappa_r)^2}{\kappa_r}\right)^{-1}$	$O(\kappa_r^{1/2})$	$O(\nu\kappa_r^{3/2}\zeta^2 n^{-1/2})$	$O(N_f^{1/2})$
S_r			$\dfrac{S_r^2}{N_f^{(r)}}\left[1 - \dfrac{2(\tan^{-1}\kappa_r)^2}{\kappa_r(\tan^{-1}\kappa_r + \dfrac{\kappa_r}{\kappa_r^2+1})}\right]^{-1}$	$O(\nu\kappa_r^2\zeta^2 n^{-1/2})$	$O(N_f^{1/2})$
S_{e_r}				$\dfrac{S_{e_r}^2}{(n_r-1)N_f^{(r)}}$	$O(N_f^{1/2})$
$\boldsymbol{\varphi}$	sym.				$\left[\sum_r k_r \mathbf{M}_r\right]^{\dagger}$

4.4.3.2 Vector parameter

For a vector-valued parameter such as the global mode shape, the asymptotic decoupling with the remaining parameters requires the maximum value of the vectorised cross-sensitivity coefficient to be small compared to 1, i.e., $q_{\theta_j \boldsymbol{\varphi}} \ll 1$, where

$$q_{\theta_j \boldsymbol{\varphi}} = \max_{\substack{\mathbf{u} \in R^n \\ \|\mathbf{u}\|=1}} \frac{J^{(\theta_j \boldsymbol{\varphi})} \mathbf{u}}{[J^{(\theta_j \theta_j)}]^{1/2} [\mathbf{u}^T J^{(\boldsymbol{\varphi}\boldsymbol{\varphi})} \mathbf{u}]^{1/2}} \tag{155}$$

and θ_j is from $\{f_r, \zeta_r, S_r, S_{e_r}\}$. The results of the cross-sensitivity coefficient w.r.t the global mode shape and the remaining parameters are shown in Table 3. It can be found that the global mode shape is asymptotically decoupled from the remaining parameters.

4.4.4 Leading order uncertainty

From Table 3, it can be seen that, for sufficiently long data and small damping, the cross-sensitivity coefficient of natural frequency, prediction error and global mode shape with the remaining parameters are asymptotically zero. This implies that f_r, S_{e_r} and $\boldsymbol{\varphi}$ are asymptotically decoupled from the remaining parameters. The coefficient $q_{\zeta_r S_r}$ is of the order of $\kappa^{-1/2}$, implying that damping ratio and modal force PSD are still coupled.

Terms w.r.t $\{f_r, \zeta_r, S_r, S_{e_r}\}$

Since the natural frequency and prediction error are decoupled from the remaining parameters, their posterior variances are directly given by the reciprocal of the corresponding leading order of J_{xy}, i.e.,

$$\sigma_{f_r}^2 \sim \frac{1}{J^{(f_r f_r)}} \qquad \sigma_{S_{e_r}}^2 \sim \frac{1}{J^{(S_{e_r} S_{e_r})}} \tag{156}$$

By substituting $J^{(f_r f_r)}$ and $J^{(S_{e_r} S_{e_r})}$ from Table 2 to (156), the posterior variance of the natural frequency and the prediction error can be determined. The results are summarised in Table 4. The parameters ζ_r and S_r are correlated and their variances need to be derived together. Utilising the cross-sensitivity $q_{\zeta_r S_r}$, the inverse of the FIM w.r.t. these two parameters can be shown to be

$$\begin{bmatrix} J^{(\zeta_r \zeta_r)} & J^{(\zeta_r S_r)} \\ J^{(\zeta_r S_r)} & J^{(S_r S_r)} \end{bmatrix}^{-1} = \begin{bmatrix} J^{(\zeta_r \zeta_r)^{-1/2}} & \\ & J^{(S_r S_r)^{-1/2}} \end{bmatrix} \begin{bmatrix} 1 & q_{\zeta_r S_r} \\ q_{\zeta_r S_r} & 1 \end{bmatrix}^{-1} \begin{bmatrix} J^{(\zeta_r \zeta_r)^{-1/2}} & \\ & J^{(S_r S_r)^{-1/2}} \end{bmatrix} \tag{157}$$

where

$$\begin{bmatrix} 1 & q_{\zeta_r S_r} \\ q_{\zeta_r S_r} & 1 \end{bmatrix}^{-1} = \frac{1}{1 - q_{\zeta_r S_r}^2} \begin{bmatrix} 1 & -q_{\zeta_r S_r} \\ -q_{\zeta_r S_r} & 1 \end{bmatrix} \tag{158}$$

$$q_{\zeta_r S_r} = \frac{J^{(\zeta_r S_r)}}{\sqrt{J^{(\zeta_r \zeta_r)} J^{(S_r S_r)}}} = -\sqrt{2}(\tan^{-1}\kappa)\kappa^{-1/2}(\tan^{-1}\kappa + \frac{\kappa}{\kappa^2 + 1}) \tag{159}$$

The posterior variance of ζ_r and S_r can then be determined by

$$\sigma_{\zeta_r}^2 \sim \frac{1}{J^{(\zeta_r\zeta_r)}(1-q_{\zeta_r S_r}^2)} \qquad \sigma_{S_r}^2 \sim \frac{1}{J^{(S_rS_r)}(1-q_{\zeta_r S_r}^2)} \tag{160}$$

The above results are summarised in Table 4, where the diagonal entries are further used for deriving the (104).

The expressions of the posterior variance w.r.t f_r, ζ_r, S_r and S_{e_r} for the r-th setup are consistent with those developed for single setup case (see [92]). These results are as expected. Since the measurement for different setups are independent, the uncertainty w.r.t. $\{f_r, \zeta_r, S_r, S_{e_r}\}$ for the r-th setup only depends on the data from that particular setup. As a result, the uncertainty w.r.t. $\{f_r, \zeta_r, S_r, S_{e_r}\}$ is the same as that in the single setup case.

Term w.r.t global mode shape $\boldsymbol{\varphi}$

Table 3 shows that the global mode shape $\boldsymbol{\varphi}$ is asymptotically decoupled from the remaining parameters when the data is sufficiently long. Deriving the posterior covariance matrix of global mode shape $\mathbf{C}_{\boldsymbol{\varphi}}$ requires the inverse of the FIM w.r.t. $\boldsymbol{\varphi}$, that is

$$\mathbf{C}_{\boldsymbol{\varphi}} \sim \left(J^{(\boldsymbol{\varphi}\boldsymbol{\varphi})}\right)^{-1} \tag{161}$$

where

$$J^{(\boldsymbol{\varphi}\boldsymbol{\varphi})} = \sum_r k_r \mathbf{L}_r{}^T (\mathbf{I}_{n_r} - \bar{\mathbf{v}}_r \bar{\mathbf{v}}_r{}^T) \mathbf{L}_r \tag{162}$$

$k_r = N_c^{(r)} \nu_r^{-1} \zeta_r^{-1} \tan^{-1}(\kappa_r)$ and $\nu_r = S_{e_r} / S_r$; $\mathbf{L}_r$ is the selection matrix of the r-th setup.

In a typical multiple-setup test, the roving DOFs among different setups should not overlap. This implies that, in the selection matrix $\mathbf{L}_r$, each column has only one non-zero element. Besides, the reference DOFs are commonly fixed among different setups. This implies that the elements in $\mathbf{L}_r$ corresponding to the reference DOFs are the same for all the selection matrices. For this context of the selection matrix, one has $\mathbf{L}_r\mathbf{L}_r^T = \mathbf{I}_{n_r}$, where $\mathbf{I}_{n_r}$ is the identity matrix with a dimension of $n_r \times n_r$.

Now consider

$$\mathbf{M}_r = \mathbf{L}_r{}^T(\mathbf{I}_{n_r} - \bar{\mathbf{v}}_r\bar{\mathbf{v}}_r{}^T)\mathbf{L}_r \tag{163}$$

Since the partial mode shape $\bar{\mathbf{v}}_r$ has unit norm, when multiplied by $\mathbf{L}_r$ and its transpose on both sides, $\mathbf{M}_r$ becomes a singular matrix with $(n-n_r+1)$ zero eigenvalues. Therefore, the inverse of $\mathbf{M}_r$ should be taken as the pseudo inverse. Due to the special structure of $\mathbf{M}_r$, it can be shown

$$\mathbf{M}_r^+ = \mathbf{M}_r \quad \text{and} \quad \mathbf{M}_r\mathbf{M}_r^T = \mathbf{M}_r \tag{164}$$

Note that $J^{(\varphi\varphi)}$ is singular along the global mode shape direction. The inverse of $J^{(\varphi\varphi)}$ therefore has to be taken as a pseudo inverse. Substituting (163) into (162) and taking the pseudo inverse gives the posterior covariance of the global mode shape, i.e.,

$$\mathbf{C}_{\boldsymbol{\varphi}} = \left[\sum_r k_r\mathbf{M}_r\right]^+ \tag{165}$$

where $\left[k_r\mathbf{M}_r\right]^+ = k_r^{-1}\mathbf{M}_r$ for $r=1,...,n_s$. It can be shown that when $n_s=1$, $\mathbf{C}_{\boldsymbol{\varphi}}$ is given directly by $k_r^{-1}\mathbf{M}_r$, which is consistent with the results for single setup (see [91]). For multiple setups, deriving the analytical expression of $\mathbf{C}_{\boldsymbol{\varphi}}$ involves the inverse of the sum of $k_r\mathbf{M}_r$ over different setups, which can be algebraically intractable. The problem size grows with the number of setups involved. Unless $\mathbf{M}_r$ has some special pattern that can help simplify the inverse of the summation, deriving the analytical expression of $\mathbf{C}_{\boldsymbol{\varphi}}$ requires other means.

4.4.5 E-MAC and mode shape c.o.v.

The 'modal assurance criterion' (MAC) is often used to quantify the discrepancy between two mode shapes, which is defined as their dot product. It can also be used for quantitively assessing the global mode shape uncertainty, by considering the expectation of the MAC between the uncertain mode shape and its MPV. This quantity is called the 'expected modal assurance criterion' (E-MAC) [133]. It is asymptotically given by [130]

$$\rho = E\left[\frac{\hat{\boldsymbol{\varphi}}^T\bar{\boldsymbol{\varphi}}}{\|\hat{\boldsymbol{\varphi}}\|\|\bar{\boldsymbol{\varphi}}\|}\right] \sim (1+\delta_{\boldsymbol{\varphi}}^2)^{-1/2} \tag{166}$$

where $\delta_{\boldsymbol{\varphi}}^2$ is the sum of the eigenvalues of $\mathbf{C}_{\boldsymbol{\varphi}}$. It can be shown using the Taylor approximation $\rho \sim 1-\delta_{\boldsymbol{\varphi}}^2/2$ for small $\delta_{\boldsymbol{\varphi}}$. Typically, ρ is close to one. This means that $\delta_{\boldsymbol{\varphi}}$, which is the square root of the trace of $\mathbf{C}_{\boldsymbol{\varphi}}$, can be used to describe the mode shape uncertainty. The lower the $\delta_{\boldsymbol{\varphi}}$ the smaller the uncertainty. The mode shape c.o.v. $\delta_{\boldsymbol{\varphi}}$ is defined as

$$\delta_{\boldsymbol{\varphi}} = \sqrt{\mathrm{tr}(\mathbf{C}_{\boldsymbol{\varphi}})} = \sqrt{\begin{matrix}\text{sum of the eigenvalues of} \\ \text{global mode shape covariance matrix}\end{matrix}} \tag{167}$$

The following investigates the eigenvalues of the global mode shape covariance matrix and their sum. The global mode shape c.o.v. is equal to the sum of the reciprocal of the eigenvalues of the FIM w.r.t. $\boldsymbol{\varphi}$. Consider a multiple-setup ambient test for measuring a total number of n DOFs. Let n_{ref} be the number of reference DOFs; $n_{rov}^{(r)}$ be the number of roving DOFs for the r-th setup; n_s be the number of setups. Assume that all the setups share the same reference DOFs. This means that the number of reference DOFs is the same for all the setups. The total number of measured DOFs is then given by $n = n_{ref} + \sum_{i=1}^{n_s} n_{rov}^{(r)}$.

Recall $\mathbf{M}_r$ from (163), which has the dimension $n \times n$. Due to the special structure of $\mathbf{M}_r$, it can be shown that the eigenvalues of $\mathbf{M}_r$ comprise a number of $n_{rov}^{(r)}$ eigenvalues that are equal to one, and the remaining eigenvalues are zero. That is

$$\mathrm{eig}\left(\mathbf{M}_r\right) = \mathrm{eig}\left[\mathbf{L}_r{}^T(\mathbf{I}_{n_r} - \bar{\mathbf{v}}_r\bar{\mathbf{v}}_r{}^T)\mathbf{L}_r\right] = \left[\underbrace{1,...,1}_{n_r-1},\underbrace{0,...,0}_{n-n_r+1}\right]^T \tag{168}$$

where $\mathrm{eig}(.)$ denotes the eigenvalues of the term in bracket; n_r is the number of DOFs in the r-th setup and $n_r = n_{ref} + n_{rov}^{(r)}$.

The eigenvalues of $J^{(r)(\boldsymbol{\varphi}\boldsymbol{\varphi})}$ for the r-th setup are then given by

$$\mathrm{eig}\left(J^{(r)(\boldsymbol{\varphi}\boldsymbol{\varphi})}\right) = \mathrm{eig}\left(k_r\mathbf{M}_r\right) = \left[\underbrace{k_r,...,k_r}_{n_r-1},\underbrace{0,...,0}_{n-n_r+1}\right]^T \tag{169}$$

Due to the special pattern of the eigenvalues of $J^{(r)(\varphi\varphi)}$, its summation $J^{(\varphi\varphi)}$ also follows a special pattern, which will be elaborated as follow.

Let $\{m_1,...,m_n\}$ denote the eigenvalues of $J^{(\varphi\varphi)} \in R^{n\times n}$. The structure of the eigenvalues of $J^{(\varphi\varphi)}$ is shown in Figure 5. These eigenvalues can be classified into four different categories. The eigenvalues in 'Group A' are simply equal to k_i and the quantity is $(n_{rov}^{(i)}-1)$ for each $i=1,...,n_s$. In 'Group B', all the eigenvalues are equal to the sum of k_i and the quantity is $(n_{ref}-1)$. The eigenvalues in 'Group C' are difficult to derive analytically, but it can be shown that their sum is always equal to the sum of k_i. The last 'Group D' contains only a zero eigenvalue, which is due to the norm constraint ($\boldsymbol{\varphi}^T\boldsymbol{\varphi}=1$) along the global mode shape direction.

Understanding these categories of the eigenvalues of $J^{(\varphi\varphi)}$, the sum of the reciprocal of $\mathrm{eig}\left(J^{(\varphi\varphi)}\right)$ can then be separated into the sum of the reciprocals of the eigenvalues in Group A, B and C. The eigenvalue in Group D is ignored as it is zero. For Group A and B, since the eigenvalues have explicit expressions, the reciprocal can be directly obtained. The results are shown in the first two terms on RHS of formula (171).

$$\{\underbrace{\underbrace{m_1,\ldots,m_{n_{rov}-1}}_{(n_{rov}^{(1)}-1)},\underbrace{m_{n_{rov}},\ldots,m_{2(n_{rov}-1)}}_{(n_{rov}^{(2)}-1)},\ldots,\underbrace{m_{(n_s-1)n_{rov}+1},\ldots,m_{n_s(n_{rov}-1)}}_{(n_{rov}^{(n_s)}-1)}}_{\substack{\text{all the eigenvalues are equal to } k_1 \quad \text{all the eigenvalues are equal to } k_2 \quad \text{all the eigenvalues are equal to } k_{n_s} \\ \textit{Group A} \\ \text{a total number of } \sum_{i=1}^{n_s}(n_{rov}^{(i)}-1)}},\underbrace{\underbrace{m_{n_s(n_{rov}-1)+1},\ldots,m_{n_s(n_{rov}-1)+n_{ref}-1}}_{(n_{ref}-1)}}_{\substack{\text{all the eigenvalues are equal to the sum of } (k_i) \\ \textit{Group B} \\ \text{a total number of } (n_{ref}-1)}},\underbrace{\underbrace{m_{n_s(n_{rov}-1)+n_{ref}},\ldots,m_{n_s n_{rov}+n_{ref}-1}}_{n_s}}_{\substack{\text{sum of the eigenvalues is equal to the sum of } (k_i) \\ \textit{Group C} \\ \text{a total number of } n_s}},\underbrace{\underbrace{m_{n_s n_{rov}+n_{ref}}}_{1}}_{\substack{\text{eigenvalue is equal to } 0 \\ \textit{Group D} \\ \text{a total number of } 1}}\}$$

$$\text{In total} \quad \sum_{i=1}^{n_s}(n_{rov}^{(i)}-1)+(n_{ref}-1)+n_s+1=\sum_{i=1}^{n_s}n_{rov}^{(i)}+n_{ref}=n$$

Figure 5 The structure of the eigenvalues of $J^{(\varphi\varphi)}$.

For those eigenvalues in Group C, determining the reciprocal of each eigenvalue can be mathematically intractable. However, it can be shown that the sum of the reciprocals of the eigenvalues in Group C is given by:

$$\sum\left[\text{eigenvalues in Group C}\right]^{-1} = \sum_{\substack{i=1;\, j=2;\\ i\neq j}}^{C_{n_s}^2} \frac{c_i c_j}{c_{ref}} (k_i^{-1} + k_j^{-1}) + \sum_{i=1}^{n_s} k_i^{-1} \tag{170}$$

where $C_{n_s}^2$ is the combination of two different numbers from 1 to n_s; c_i and c_j are the sum of the squared mode shape values at the roving DOFs in the i-th and j-th setup, respectively; c_{ref} is the sum of the squared mode shape values at the reference DOFs. Equation (170) is concluded based on the pattern of the sum of the reciprocals of the eigenvalues in Group C. Its correctness has been verified numerically.

Summarising the above eigenvalue reciprocals, the trace of the global mode shape covariance matrix (i.e., squared global mode shape c.o.v.) can be analytically expressed as

$$\delta_{\boldsymbol{\varphi}}^2 = \underbrace{\sum_{i=1}^{n_s} (n_{rov}^{(i)} - 1) k_i^{-1}}_{\substack{\sum_{i=1}^{n_s}(n_{rov}^{(i)}\text{-1}) \text{ eigenvalues}\\ \text{from the group A with reciprocal}}} + \underbrace{(n_{ref} - 1)(\sum_{i=1}^{n_s} k_i)^{-1}}_{\substack{(n_{ref}\text{ -1}) \text{ eigenvalues}\\ \text{from the group B with reciprocal}}} + \underbrace{\left[\sum_{\substack{i=1;\, j=2;\\ i\neq j}}^{C_{n_s}^2} \frac{c_i c_j}{c_{ref}} (k_i^{-1} + k_j^{-1}) + \sum_{i=1}^{n_s} k_i^{-1} \right]}_{\substack{n_s \text{ eigenvalues}\\ \text{from the group C}}} \tag{171}$$

Further simplifying the above formula gives

$$\delta_{\boldsymbol{\varphi}}^2 = \sum_{\substack{i=1;\, j=2;\\ i\neq j}}^{C_{n_s}^2} \frac{c_i c_j}{c_{ref}} (k_i^{-1} + k_j^{-1}) + \sum_{i=1}^{n_s} n_{rov}^{(i)} k_i^{-1} + (n_{ref} - 1)(\sum_{i=1}^{n_s} k_i)^{-1} \tag{172}$$

Define the following $n_s \times 1$ vectors

$$\mathbf{c}=\begin{bmatrix} c_1 \\ \vdots \\ c_{n_s} \end{bmatrix} \qquad \mathbf{b}=\begin{bmatrix} 1 \\ \vdots \\ 1 \end{bmatrix} \qquad \mathbf{n}_{rov}=\begin{bmatrix} n_{rov}^1 \\ \vdots \\ n_{rov}^{n_s} \end{bmatrix} \qquad \mathbf{k}=\begin{bmatrix} k_1 \\ \vdots \\ k_{n_s} \end{bmatrix} \tag{173}$$

The squared global mode shape c.o.v. can be rewritten in a compact manner:

$$\delta_{\varphi}^2=\frac{\mathbf{c}^T\mathbf{A}\mathbf{c}}{2c_{ref}}+\mathbf{n}_{rov}^T\mathbf{k}^{-1^*}+(n_{ref}-1)(\mathbf{b}^T\mathbf{k})^{-1} \tag{174}$$

where $\mathbf{k}^{-1^*}$ denotes the reciprocal of all the elements in $\mathbf{k}$; $\mathbf{A}$ is a collection of k_i:

$$\mathbf{A}=\begin{bmatrix} 0 & k_1^{-1}+k_2^{-1} & \cdots & k_1^{-1}+k_{n_s}^{-1} \\ k_2^{-1}+k_1^{-1} & 0 & \ddots & \vdots \\ \vdots & \ddots & \ddots & k_{n_s-1}^{-1}+k_{n_s}^{-1} \\ k_{n_s}^{-1}+k_1^{-1} & \cdots & k_{n_s}^{-1}+k_{n_s-1}^{-1} & 0 \end{bmatrix} \tag{175}$$

Formulae (172) and (174) are applicable for both single setup and multiple setups. When $n_s=1$, the first term on the RHS of (172) vanishes and the global mode shape c.o.v. becomes $(n-1)k_1$, which is the same expression as that in the single setup case (see [91]). For multiple setups, it should be noted that these formulae are only valid when n_{ref} and $n_{rov}^{(i)}$ are non-zero, which is typical in multiple-setup applications. For other cases, e.g., no reference DOFs or no roving DOFs, there is no practical significance and it is not considered in this work.

The above two formulae can be used to determine the squared posterior global mode shape c.o.v. in multiple-setup OMA. The value of δ_{φ}^2 reflects the level of global mode shape uncertainty. It can be seen from (174) that δ_{φ}^2 depends on c_{ref}, n_s, n_{ref}, $\mathbf{c}$, $\mathbf{n}_{rov}$ and $\mathbf{k}$, which are included in the test configuration of multiple setups. These formulae reveal the relationship between the global mode shape uncertainty and the multiple-

setup test configuration. An investigation of the global mode shape c.o.v is conducted in the next section.

4.5 Investigating mode shape c.o.v.

Formulae (172) and (174) provide closed-form expressions for determining the squared posterior global mode shape c.o.v. From the formulae, it can be seen that the parameters consist of

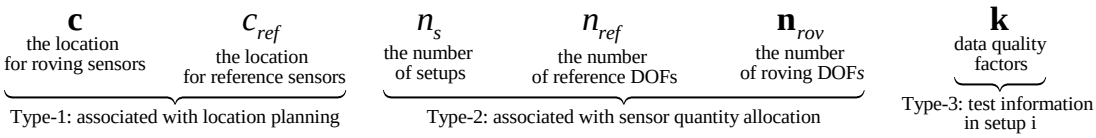

These parameters can be classified into three different categories. Type-1 parameters include the sum of the squared mode shape values of roving locations ($\mathbf{c}$) and the sum of the squared mode shape values of reference locations (c_{ref}). Type-2 parameters include the number of reference sensors (n_{ref}), the number of roving sensors ($\mathbf{n}_{rov}$) and the number of setups (n_s). The parameters in type-1 and type-2 together govern the entire setup configuration. The parameter of type-3 is $\mathbf{k}$, which is a vector that comprises the data quality factor for each setup. This section focuses on investigating how the global mode shape c.o.v. depends on the sensor locations, i.e., investigating type-1 parameters. The location planning for multiple setups is also addressed.

4.5.1 Location planning

Location planning involves the selection of reference sensor locations and roving sensor locations, which are reflected by $\mathbf{c}$ and c_{ref}, respectively. The elements in $\mathbf{c}$ are given by the sum of squared mode shape values at the roving locations for each

setup. The parameter c_{ref} is given by the sum of squared mode shape values at the reference locations. To investigate the location factors, the following objective function is formulated based on (174), considering the norm constraint $\mathbf{b}^T\mathbf{c}+c_{ref}=1$ that is handled by a Lagrange multiplier. That is

$$J(\mathbf{c},c_{ref},\lambda)=\frac{\mathbf{c}^T\mathbf{A}\mathbf{c}}{2c_{ref}}+\mathbf{n}_{rov}^T\mathbf{k}^{-1^*}+(n_{ref}-1)(\mathbf{b}^T\mathbf{k})^{-1}+\lambda\left(1-c_{ref}-\mathbf{b}^T\mathbf{c}\right) \tag{176}$$

To investigate the effect of $\mathbf{c}$ and c_{ref}, we assume that $\mathbf{n}_{rov}$, n_{ref} and $\mathbf{k}$ are fixed and known. Setting the derivative of J w.r.t. $\mathbf{c}$ to be zero and solving for $\mathbf{c}$ gives

$$\mathbf{c}^T=\lambda c_{ref}\mathbf{b}^T\mathbf{A}^{-1} \tag{177}$$

Further differentiating J w.r.t λ and then setting the equation to be zero gives

$$\mathbf{b}^T\mathbf{c}=1-c_{ref} \tag{178}$$

Right-multiplying $\mathbf{b}$ in (177) gives

$$\lambda=\frac{1-c_{ref}}{c_{ref}\mathbf{b}^T\mathbf{A}^{-1}\mathbf{b}} \tag{179}$$

Further substituting (179) into (177) gives

$$\hat{\mathbf{c}}=(1-c_{ref})\frac{\mathbf{A}^{-1}\mathbf{b}}{\mathbf{b}^T\mathbf{A}^{-1}\mathbf{b}} \tag{180}$$

The corresponding value of J is

$$\hat{J} = \frac{1}{2\mathbf{b}^T\mathbf{A}^{-1}\mathbf{b}}(c_{ref} + \frac{1}{c_{ref}} - 2) + \mathbf{n}_{rov}^T\mathbf{k}^{-1^*} + (n_{ref} - 1)(\mathbf{b}^T\mathbf{k})^{-1} \tag{181}$$

Equation (181) gives an optimal J that depends on c_{ref}, where $0 < c_{ref} < 1$. It can be shown that $\hat{J}$ is monotonic decreasing with c_{ref}. The larger the c_{ref} the smaller the $\hat{J}$. This simply suggests one to place the reference sensors at the locations where c_{ref} value is as large as possible.

Equation (180) gives the optimal value of $\hat{\mathbf{c}}$, which depends on $\mathbf{A}$ and c_{ref}. The matrix $\mathbf{A}$ consists of k_i from different setups, where $k_i = N_c^{(i)}\nu_i^{-1}\zeta_i^{-1}\tan^{-1}\kappa_i$ as in (175). Assume nominally that the setups are under similar conditions, i.e., the ambient excitation and the instrument noise are in a similar level among different setups. It is then reasonable to assume the same value of k_i for all the setups. The expression of $\hat{\mathbf{c}}$ can then be simplified to

$$\hat{\mathbf{c}} = \frac{(1 - c_{ref})}{n_s}\mathbf{b} \tag{182}$$

This $\hat{\mathbf{c}}$ corresponds to $c_1 = c_2 = ,..., = c_{n_s}$. Note that the Hessian of J w.r.t $\mathbf{c}$ is negative definite, which implies that $\hat{\mathbf{c}}$ maximises J. This means that the global mode shape c.o.v. is the greatest when the roving sensors in each setup are placed at the locations that provide the same $\hat{c}_i$ value for the i-th setup.

4.5.2 Numerical example

To illustrate the findings in the previous sections, a numerical example is presented in this section. Without loss of generality, consider a shear building with ten DOFs (see

Figure 6). Consider a multiple-setup plan with two reference sensors, four roving sensors and two setups.

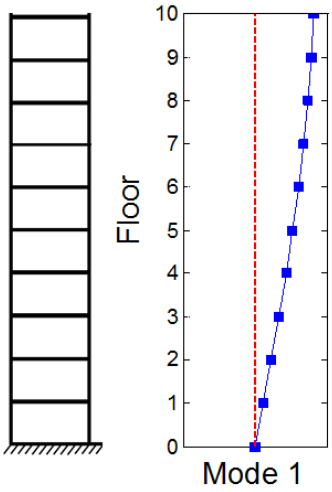

Figure 6 Ten-storey shear building and its first mode shape.

Synthetic data is generated as in Section 3.4. Assume a natural frequency of 1 Hz and damping ratio of $\zeta = 1\%$. Assume that the modal force and prediction error are i.i.d. Gaussian white noise with a PSD of 1.6 $(\mu g)^2/\text{Hz}$ and 1 $(\mu g)^2/\text{Hz}$, respectively. The data is generated for 1,000 seconds at a sampling rate of 100 Hz.

Consider the first mode of the building (see Figure 6). For different settings of reference and roving sensors, the global mode shape c.o.v. can be calculated using (174). By exhausting all possible choices of the reference and roving locations, a plot of δ_{φ}^2 w.r.t c_{ref} is shown in Figure 7. The blue stars indicate all the different choices of location planning. The red circles indicate the value of δ_{φ}^2 calculated at the value of c_i that maximises δ_{φ}^2. The ref option 1 in the figure shows the minimum value of c_{ref} that can be obtained when the reference sensors are placed on the bottom two floors (floors 1 and 2). The ref option 2 shows the maximum c_{ref} when the reference sensors are located on the top two floors (floors 9 and 10).

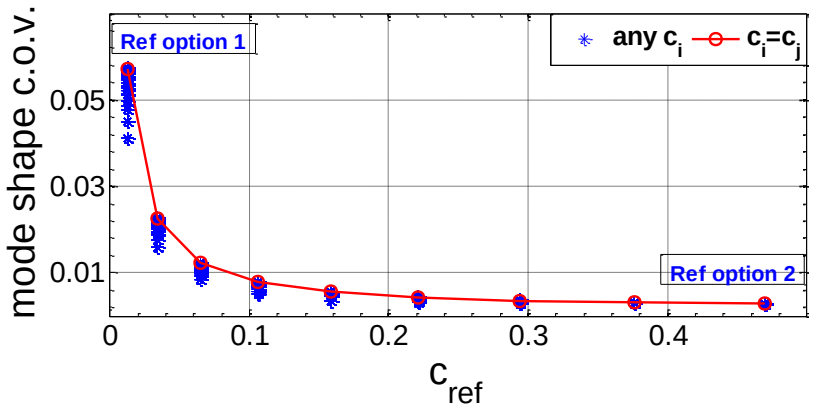

Figure 7 The global mode shape c.o.v. with different c_{ref} .

It can be seen that the global mode shape c.o.v. decreases with c_{ref} . This demonstrates that the higher c_{ref} , the lower the global mode shape c.o.v. This implies that the reference sensors should be placed at those locations whose c_{ref} value is as large as possible. The figure also shows that as c_{ref} increases, the variation of δ_{φ}^2 calculated based on different c_i decreases. This implies that, as long as the reference sensors are in a good position (i.e., with a reasonably large value of c_{ref}), the choice of roving sensors become insignificant. The red circles illustrate the maximum value of global mode shape uncertainty when the roving sensors are placed at the locations with the same c_i for all the setups.

By investigating **c** and c_{ref} through (174), scientific guidance for reducing the identification uncertainty can be made for multiple-setup location planning. The reference sensors should be placed at those locations whose sum of the squared mode shape values is as large as possible. As long as the reference locations are placed in a good position, it does not matter how the roving locations are planned, as different settings can yield similar level of global mode shape uncertainty. This means the selection of roving locations can be simplified by focusing on other planning aspects

(e.g., logistics), rather than identification precision. It should be noted that the investigation here is based on the planning for a single mode. For multiple modes, the planning should consider all the different modes.

4.6 Empirical studies

This section presents empirical studies, where synthetic, experimental and field test data are used to validate the uncertainty law of multiple setups and the long data asymptotic behaviour of the posterior covariance matrix. The data length effect is investigated through the normalised data length N_c, which is proportional to the number of FFT coordinates in the selected frequency band. Three quantities of the uncertainty (posterior variance, uncertainty law and the CRB) are assessed and the results are compared to each other. The posterior variance refers to the diagonal entry of the posterior covariance matrix, which is calculated from the inverse of the Hessian of the NLLF and evaluated at MPV. The uncertainty law refers to the long data asymptotic expression of the leading order of the posterior covariance matrix. It is calculated using the expressions in Table 4 and evaluated at MPV. For the global mode shape, the quantity is calculated using (106), which is the trace of the posterior covariance of the global mode shape. The CRB is obtained from the diagonal entry of the inverse of the entire FIM (see Table 1). This FIM should be calculated from the expectation of the Hessian of the NLLF at the 'true' parameter values. Note that these actual parameters only exist in the synthetic data example. For laboratory and field test, the actual parameters are unknown or even may not exist. To validate the uncertainty law and to avoid misjudging the difference between the actual values and MPVs, the CRB is evaluated at MPV. For this reason, it no longer refers to the lower

bound of the posterior uncertainties. The name used here is merely to ensure consistency with the conventional terminology in classical statistics.

4.6.1 Eleven-DOF shear building (synthetic data)

An eleven-storey shear type building is considered with eleven horizontal DOFs distributed on each floor. The building is assumed to have a uniform stiffness of 100 $\mathrm{kN/mm}$, with a floor mass of 50 ton. The fundamental frequency is calculated as 0.9714 Hz. Assume classical damping with a damping ratio of 1% for all modes. The structure is subjected to horizontal i.i.d. Gaussian white noise excitations with a PSD of 0.24 $\mathrm{N^2/Hz}$. The data is assumed to be contaminated by i.i.d. Gaussian white noise with a PSD of 4 $(\mu\mathrm{g})^2/\mathrm{Hz}$.

Consider a multiple-setup ambient vibration test with five uniaxial accelerometers. Assume that three setups are planned to cover all eleven DOFs with two fixed reference sensors ($1^{\#}$ and $2^{\#}$) and three roving sensors ($3^{\#}$, $4^{\#}$ and $5^{\#}$) that move from the top floor to the bottom floor (see setup information in Figure 8 (left)). The data in all setups are generated with the same sampling rate at 100 Hz.

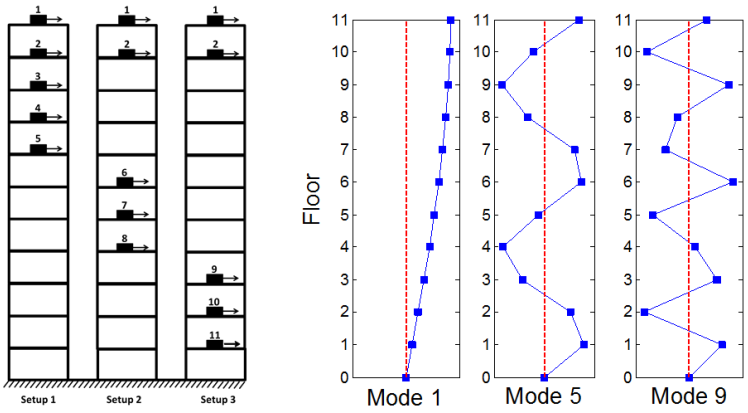

Figure 8 Setup information (left) and the global mode shapes of modes 1, 5 and 9 (right).

The synthetic data is first examined using a root singular value (SV) spectrum, which is the square root of the eigenvalues of the sample PSD matrix. The SV spectrum is a conventional tool used in OMA to visualise the potential modes in the frequency domain. Figure 9 shows the root SV spectrum produced by the first setup data, where the peaks indicate potential modes. A Bayesian modal identification method incorporating multiple-setup data [65] is applied to obtain the MPV of the modal parameters and the posterior covariance matrix.

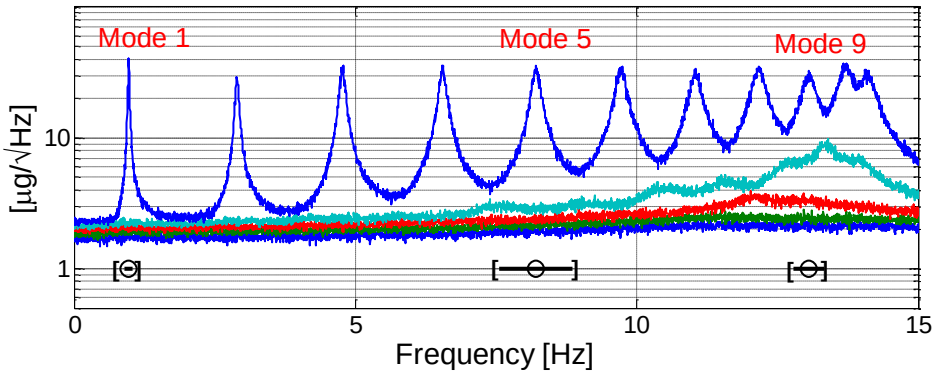

Figure 9 The root SV spectrum with selected frequency bands using the first setup data.

Without loss of generality, three modes (1, 5, 9) with different levels of s/n ratio are selected for modal identification and validation of the uncertainty law. The theoretical global mode shapes are calculated and plotted in Figure 8 (right).

The modal s/n ratio is calculated based on the identification results. It is given by the ratio of the spectral density of modal excitation to the spectral density of prediction error at the resonance peak, i.e.,

$$\gamma = \frac{S}{4S_e\zeta^2} \tag{183}$$

The modal s/n ratio reflects how well-excited a mode is compared to the noise level. The ratios of the first, fifth and ninth modes in each setup are shown in Figure 10. The

ratios of the first mode are above 200, which are considered moderately high. In contrast, the ratios of the ninth mode are below 100, which are considered low. The s/n ratios for the fifth mode are at a moderate level.

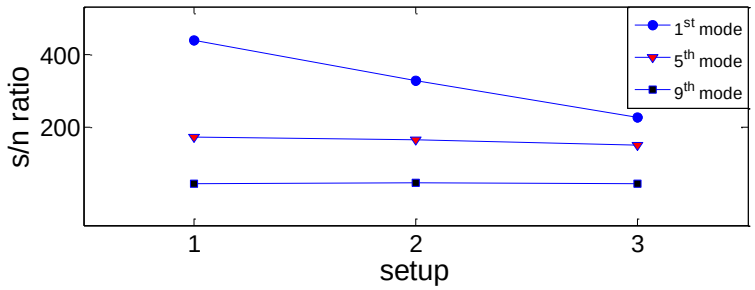

Figure 10 The modal s/n ratios of the modes 1, 5 and 9 among setups.

First mode

By selecting a frequency band of [0.893 1.049] Hz , it is possible to identify the modal parameters of the first mode. Figure 11 shows the identification results of the first setup. The MPVs (blue dots) with ± two standard derivations (error bars) are plotted against the data length N_c from 100 to 10,000. The red dash lines in the figure indicate the 'actual' parameter values. It can be seen that all of the identified modal parameters converge to the actual parameter values as N_c increases. The variances of the modal parameters are also reduced. Similar trends can be found in the remaining setups. For this mode, the s/n ratios for different setups with $N_c = 10{,}000$ are calculated as 439, 328 and 229, respectively.

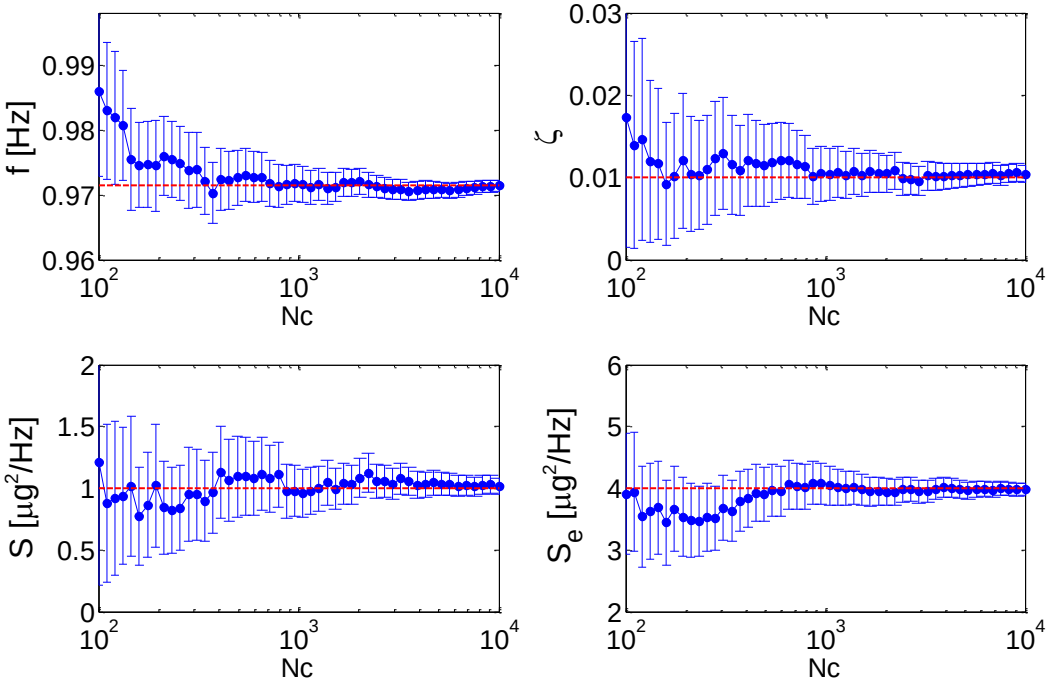

Figure 11 Identified modal parameters (MPVs, blue dots) with ±2 standard derivations (error bars) and actual parameter values (red dash lines), mode 1, setup 1.

Three uncertainty quantities of the modal parameters are calculated and compared with each other. Figure 12 shows the values for the first setup as data length increases. The posterior variance (red triangle), the diagonal entry of the CRB (black cross) and the uncertainty law (blue circle) are plotted. These quantities decrease with data length. Their values approach each other as data length increases. Figure 13 shows the global mode shape c.o.v of these three quantities as N_c increases. Similar trends can also be found. From the plots, the long data asymptotic behaviour of the posterior variance is validated. The uncertainty law established in this work is also validated.

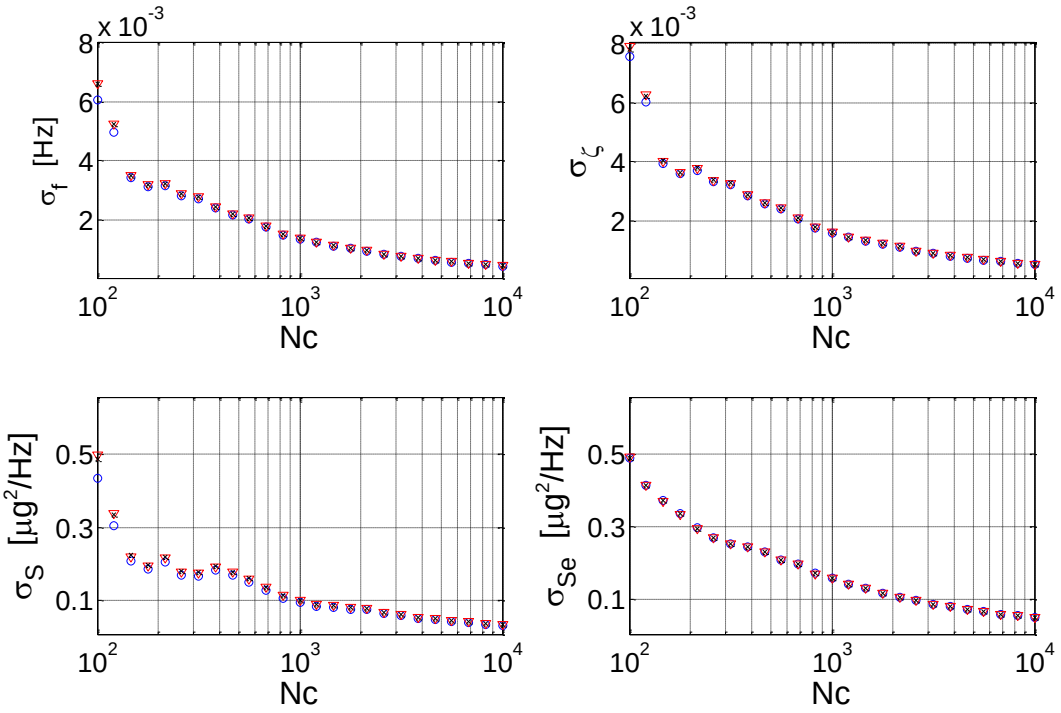

Figure 12 Posterior standard derivation of modal parameters (red triangle), CRB (black cross) and uncertainty law (blue circle), mode 1, setup 1.

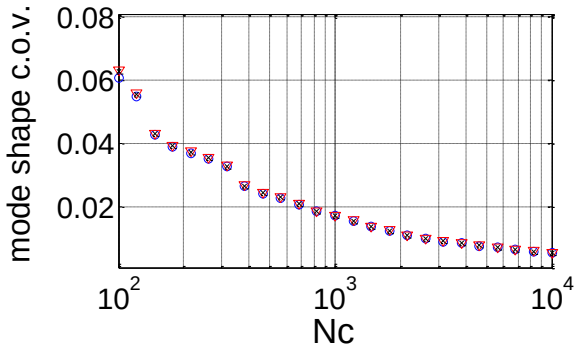

Figure 13 Posterior global mode shape c.o.v. (red triangle), CRB (black cross) and uncertainty law (blue circle), mode 1, setup 1.

Fifth mode

The fifth mode is identified with a selected frequency band of $[7.55\ 8.86]$ Hz . Similar to the first mode, the identification results for natural frequency, damping ratio and modal force PSD converge to their actual values The uncertainties decrease as data length increases. Figure 14 shows the results for the first setup. Due to increased modelling error, the prediction error is higher than the initial setting ($4\ \mu g^2/Hz$) and

its value converges to approximately $5.8\ \mu g^2/Hz$. The s/n ratios with $N_c = 1{,}000$ for different setups are calculated as 173, 167 and 151.

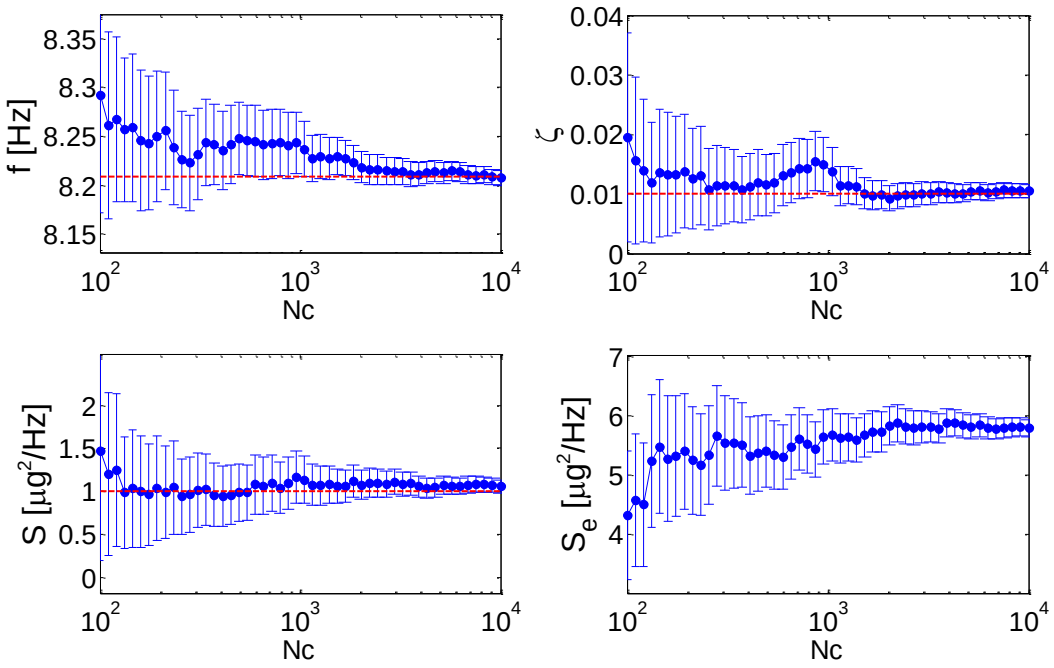

Figure 14 Identified modal parameters (MPVs, blue dots) with ±2 standard derivations (error bars) and actual parameter values (red dash lines), mode 5, setup 1.

Figure 15 and Figure 16 show the results of the three uncertainty quantities plotted with data length. As can be seen, there is a decreasing trend with data size. The uncertainty quantities are closer to each other and finally converge. This demonstrates that with a moderate level of s/n ratio, the proposed uncertainty law and the asymptotic behaviour of the posterior covariance are valid.

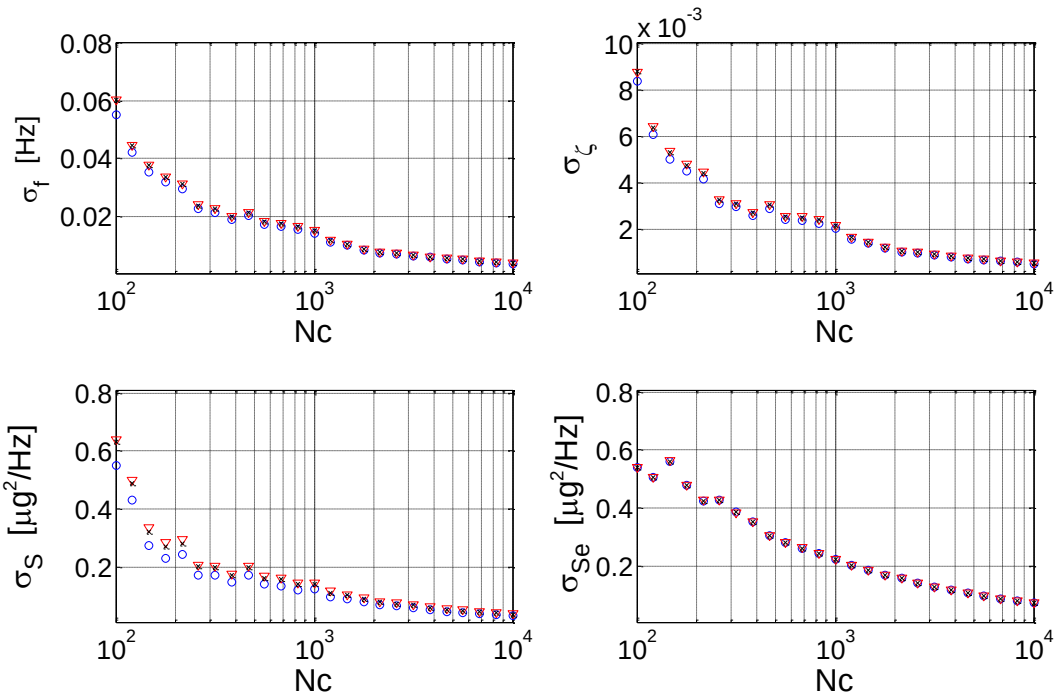

Figure 15 Posterior standard derivation of modal parameters (red triangle), CRB (black cross) and uncertainty law (blue circle), mode 5, setup 1.

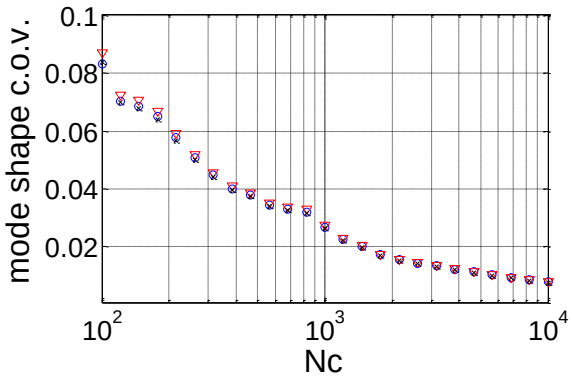

Figure 16 Posterior global mode shape c.o.v. (red triangle), CRB (black cross) and uncertainty law (blue circle), mode 5, setup 1.

Ninth mode

The ninth mode is selected in order to validating a low s/n ratio case. The modal parameters are identified with a frequency band selected from [12.78 13.33] Hz . The identification results are shown in Figure 17, where natural frequency, damping ratio and modal force PSD converge to their actual values. Due to increased modelling error in higher modes, the prediction error of the ninth mode is much larger than the initial setting value ($4\ \mu g^2/Hz$). With sufficiently long data, the prediction error converges

to approximately 18 $\mu g^2/Hz$. The s/n ratios for different setups with $N_c = 1{,}000$ are calculated as 45, 49 and 46.

Figure 18 and Figure 19 show the plots of the results as data length increases. Due to the low s/n ratio, when the data length is relatively short ($N_c < 1{,}000$), large discrepancies among these quantities can be seen. In contrast, when the data length is sufficiently long, the discrepancies vanish and the results eventually match. This implies that although the uncertainty law is developed based on small damping and high s/n ratio conditions, the long data asymptotic behaviour of the posterior covariance is still valid for low s/n ratio situation.

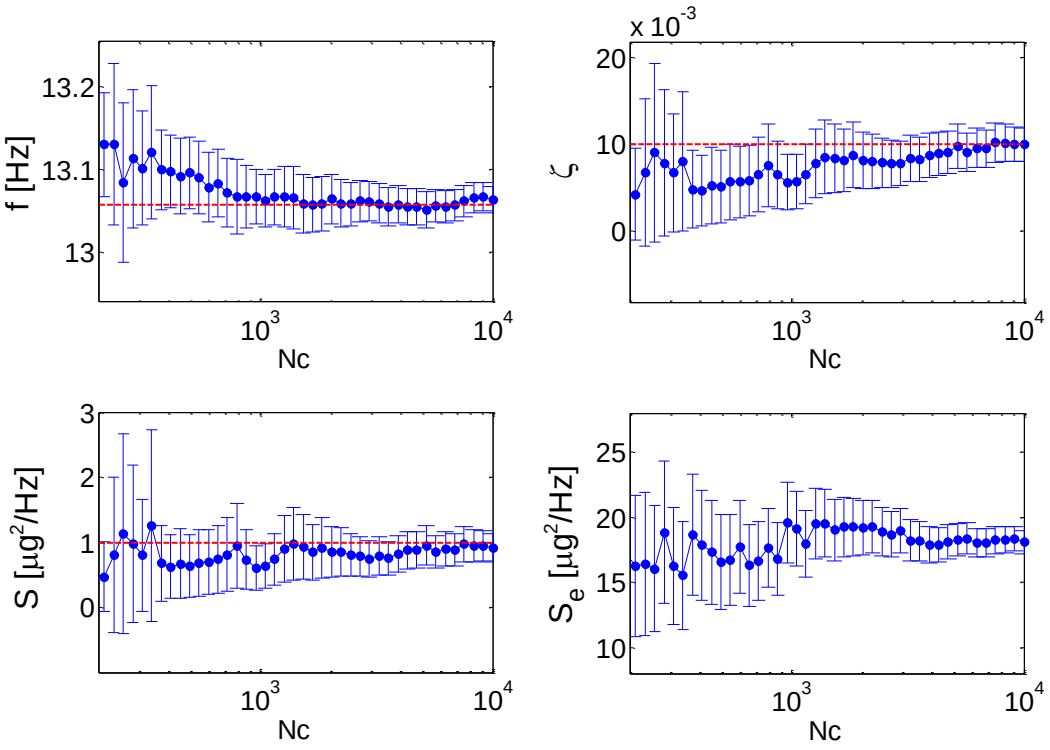

Figure 17 Identified modal parameters (MPVs, blue dots) with ±2 standard derivations (error bars) and actual parameter values (red dash lines), mode 9, setup 1.

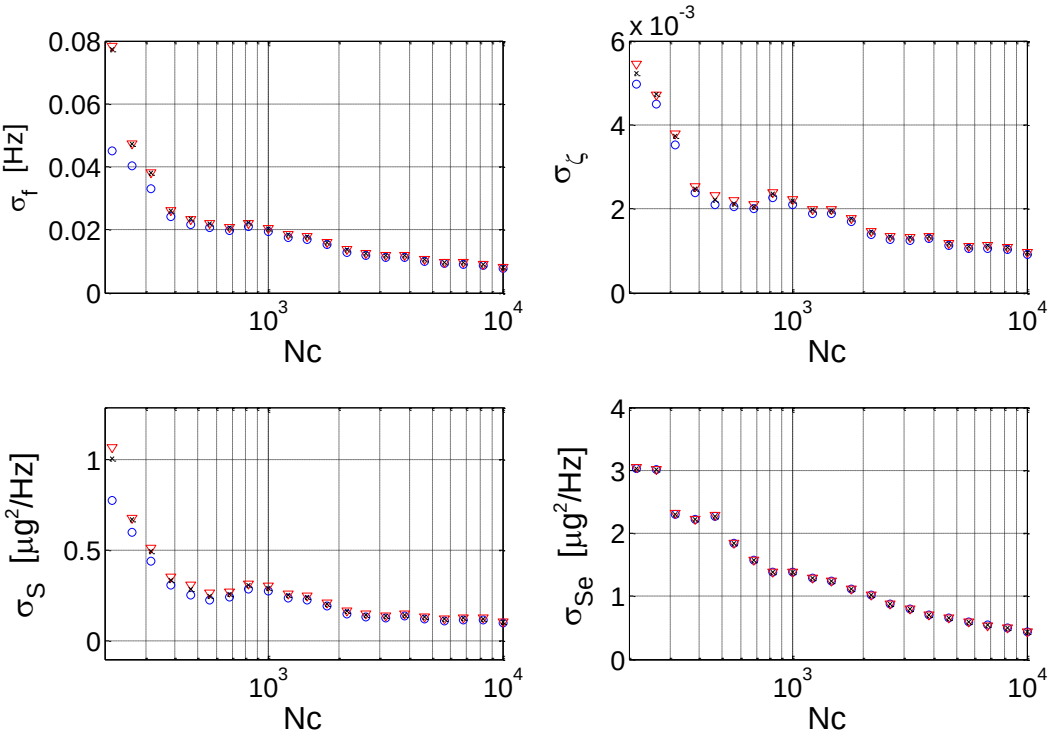

Figure 18 Posterior standard derivation of modal parameters (red triangle), CRB (black cross) and uncertainty law (blue circle), mode 9, setup 1.

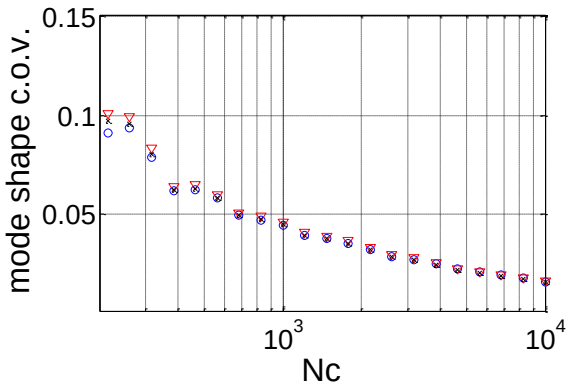

Figure 19 Posterior global mode shape c.o.v. (red triangle), CRB (black cross) and uncertainty law (blue circle), mode 9, setup 1.

4.6.2 Three-storey shear frame (laboratory experiment)

A laboratory experiment on a three-storey aluminium shear frame is presented to illustrate the long data asymptotic behaviour of the posterior covariance. Different from synthetic data simulation, a laboratory experiment provides real data that are measured.

The shear frame is shown in Figure 20 (a). Each floor has a uniform mass of 4.86 kg (aluminium plate with dimensions of 30 cm × 20 cm × 3 cm). The columns are fixed at four corners of each floor, with dimensions of 22 cm in height, 1.5 cm in width and 0.3 cm in thickness. Four piezoelectric accelerometers with biaxial channels (horizontal x and y directions) are used for ambient vibration measurement. The test covers the four corners of each floor, giving a total of 24 measured DOFs.

Multiple setups are planned with four reference DOFs and ten roving DOFs and two setups. See Figure 20 (b), where the red locations correspond to the references. The data for each setup is collected for 100 mins, which is considered long enough to cover the N_c at a maximum value of 10,000. The measurement is taken at a sampling rate of 2048 Hz , which is later decimated to 256 Hz for analysis.

Figure 21 plots the root SV spectrum within 30 Hz , where five potential modes can be observed. Without loss of generality, two modes (highlighted in Figure 21) are selected for modal identification and validation of the uncertainty law.

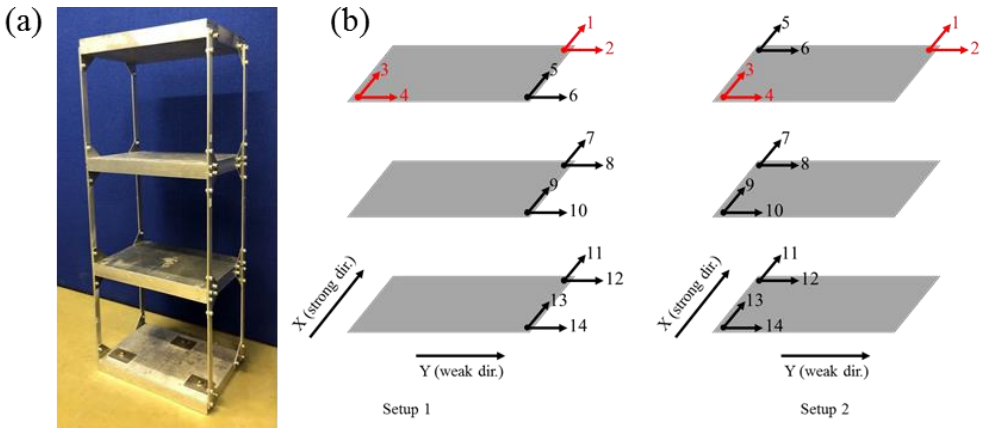

Figure 20 (a) Three-storey aluminium shear frame; (b) setup plan.

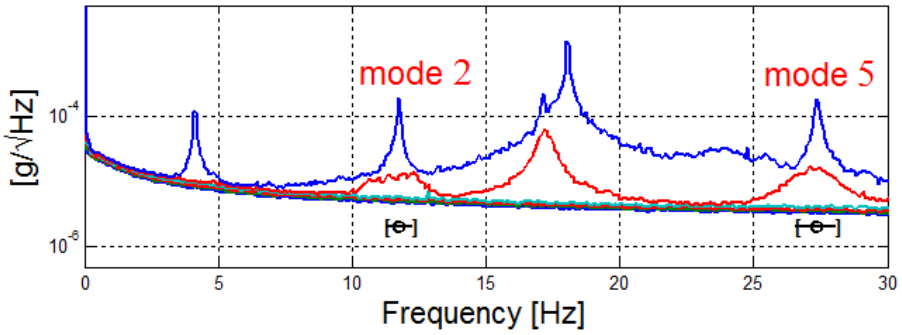

Figure 21 The root SV spectrum with selected frequency bands using the first setup data.

Second mode

By selecting a frequency band of [11.25 12.25] Hz, the second mode is identified. Figure 22 shows the identification results of the first setup. The MPVs (blue dots) with ± two standard derivations (error bars) are plotted with data length. The MPV of natural frequency and damping ratio converge as data length increases. The error bars shorten as N_c increases. For the MPV of modal force PSD and prediction error, due to the random nature of the ambient excitation, variation in results can still be observed even for long data length. The variances of these two parameters decrease as data length increases. Similar trends can be found in the remaining setups.

The three uncertainty quantities for the second mode are calculated. Figure 23 and Figure 24 show the values for the first setup. A decreasing trend of the uncertainties can be found as data length increases. It can also be seen that the uncertainty quantities eventually match each other. A similar trend in the remaining setups can also be found. This validates the long data asymptotic behaviour of the posterior covariance matrix.

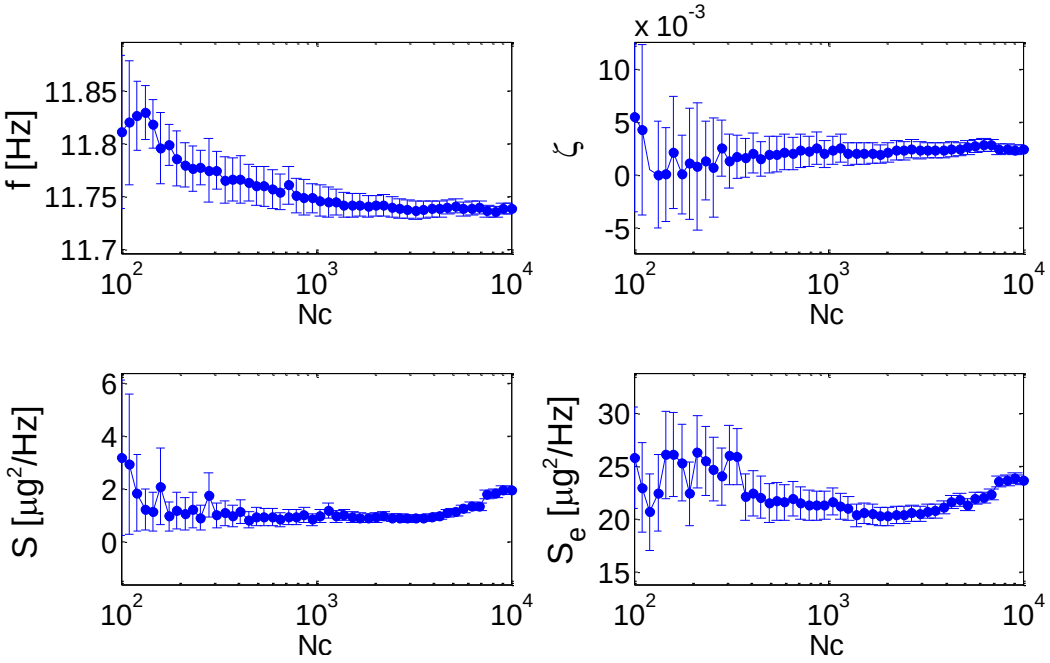

Figure 22 Identified modal parameters (MPVs, blue dots) with ±2 standard derivations (error bars), mode 2, setup 1.

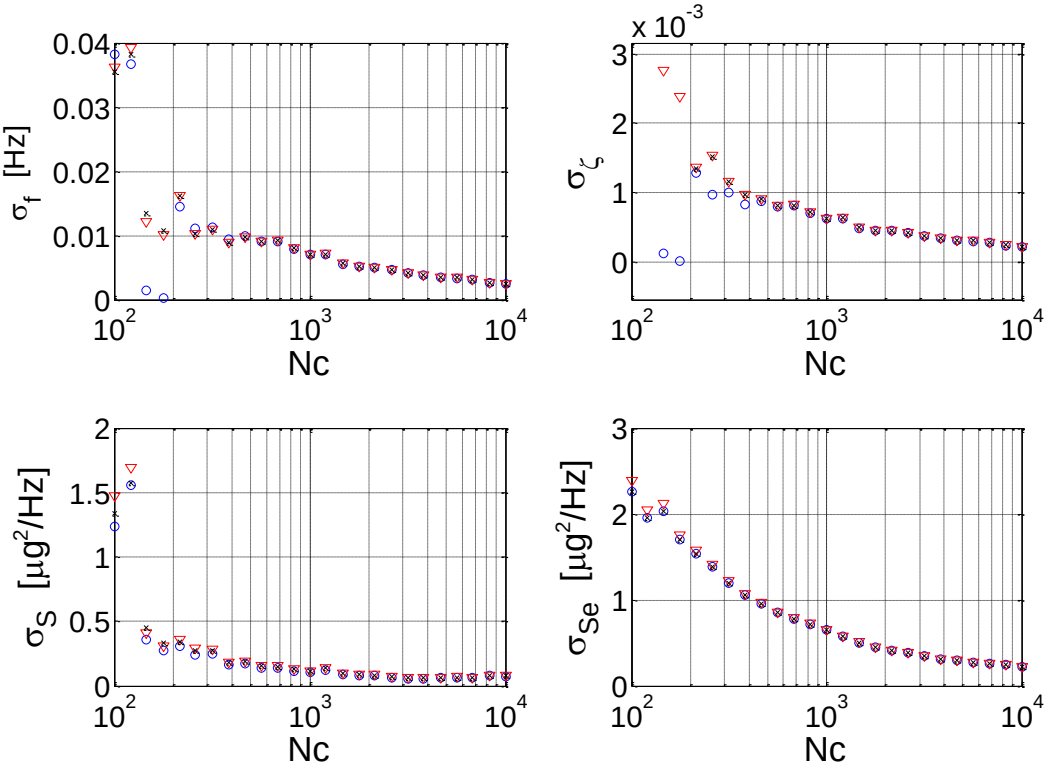

Figure 23 Posterior standard derivation of modal parameters (red triangle), CRB (black cross) and uncertainty law (blue circle), mode 2, setup 1.

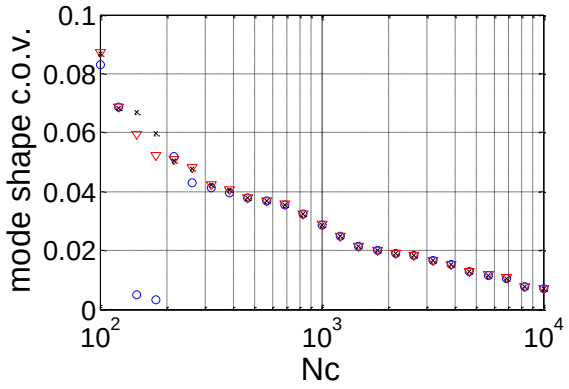

Figure 24 Posterior global mode shape c.o.v. (red triangle), CRB (black cross) and uncertainty law (blue circle), mode 2, setup 1.

Fifth mode

The fifth mode is identified with a frequency band of $[26.58\ 28.08]\,\mathrm{Hz}$. Similar plots of the identification results are shown in Figure 25. It can be seen that, as data length increases, the natural frequency and damping ratio converge and their variances are reduced. A reduction of the variance can also be found in the modal force PSD and prediction error.

Figure 26 and Figure 27 show the results of the three uncertainty quantities. The three uncertainty quantities decrease with data length. For short data length, large discrepancies in these quantities can be found. Conversely, as N_c increases, the gaps vanish and the uncertainty quantities eventually agree with each other. This again validates the proposed theory.

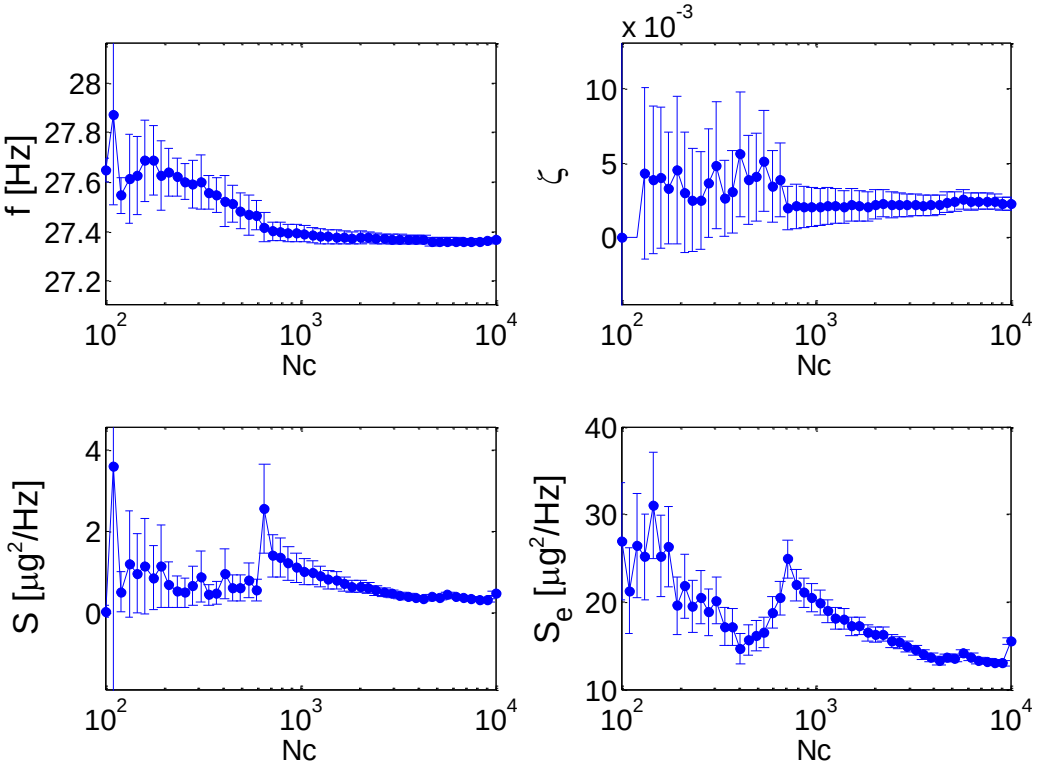

Figure 25 Identified modal parameters (MPVs, blue dots) with ±2 standard derivations (error bars), mode 5, setup 1.

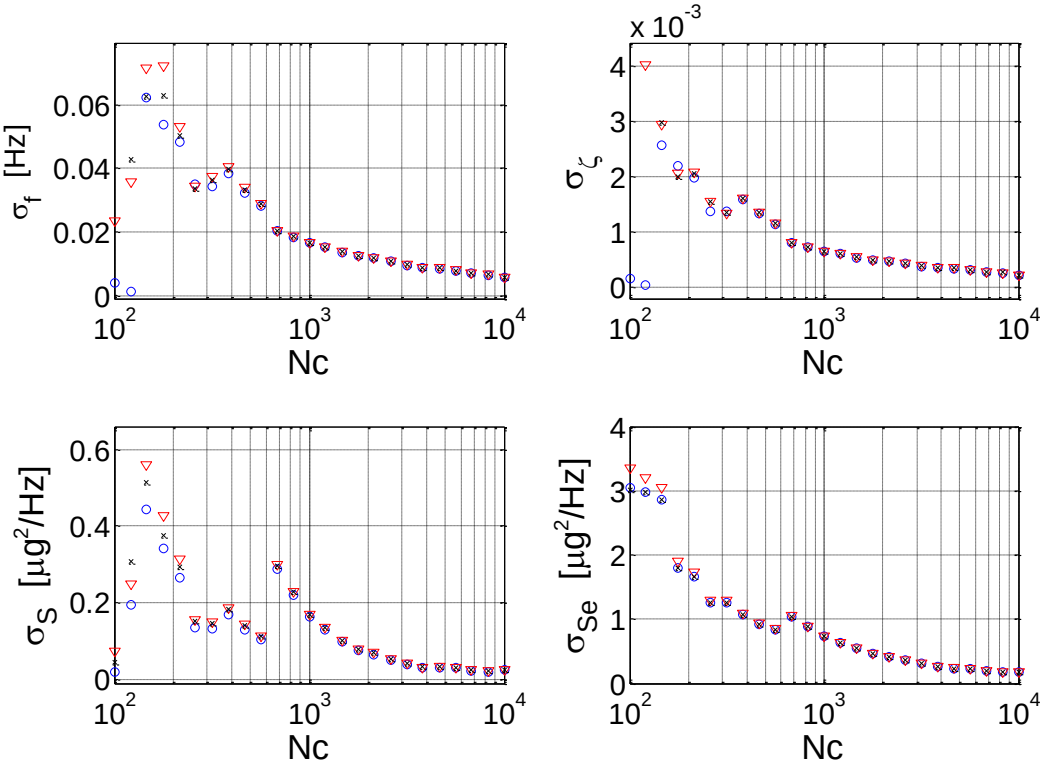

Figure 26 Posterior standard derivation of modal parameters (red triangle), CRB (black cross) and uncertainty law (blue circle), mode 5, setup 1.

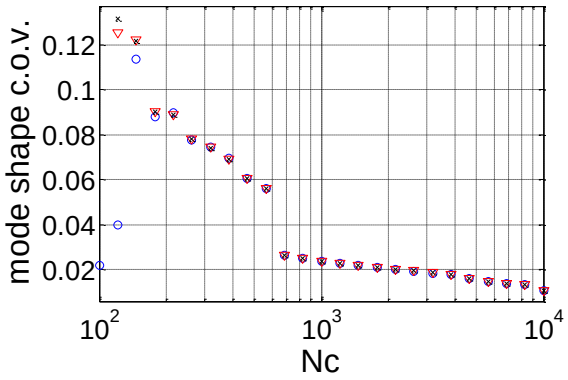

Figure 27 Posterior global mode shape c.o.v. (red triangle), CRB (black cross) and uncertainty law (blue circle), mode 5, setup 1.

4.6.3 Brodie Tower (field test)

Field test data has a variety of complications that are difficult to replicate by numerical simulation or in the laboratory. In this example, field test data from an eight-storey building called Brodie Tower is used to validate the long data asymptotic behaviour of the posterior covariance matrix. Without loss of generality, the study here focuses on one particular mode.

Figure 28 shows the overview of the building and its floor plan with sensor locations, where Ⓡ indicates the reference sensor location at one corner on the top floor; ① to ④ are the roving sensor locations for each floor. The vibration test comprises seven setups. A detailed description of the field test deployment and modal identification of the Brodie Tower can be found in Section 5.4.

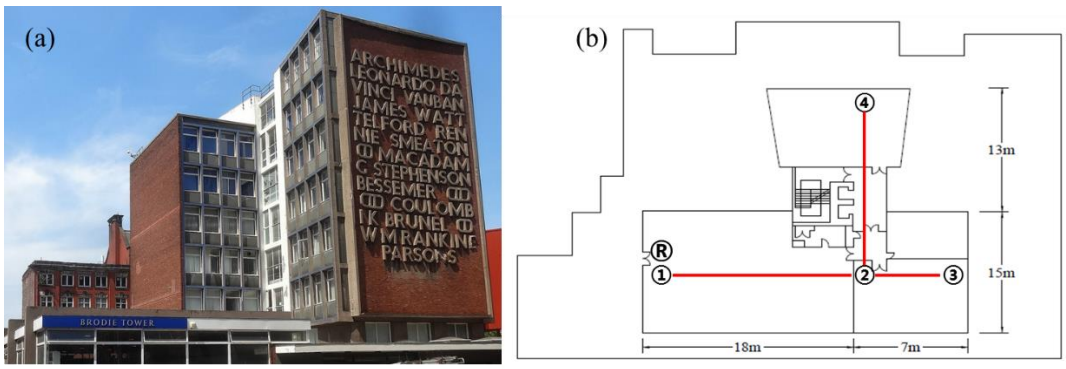

Figure 28 (a) Overview of the Brodie Tower; (b) floor plan and sensor locations.

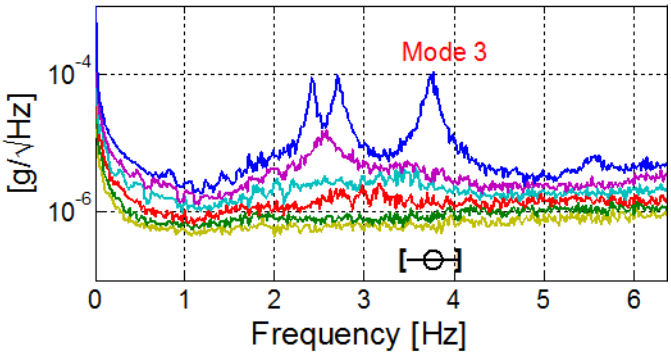

Figure 29 The root SV spectrum with selected frequency band using the first setup data.

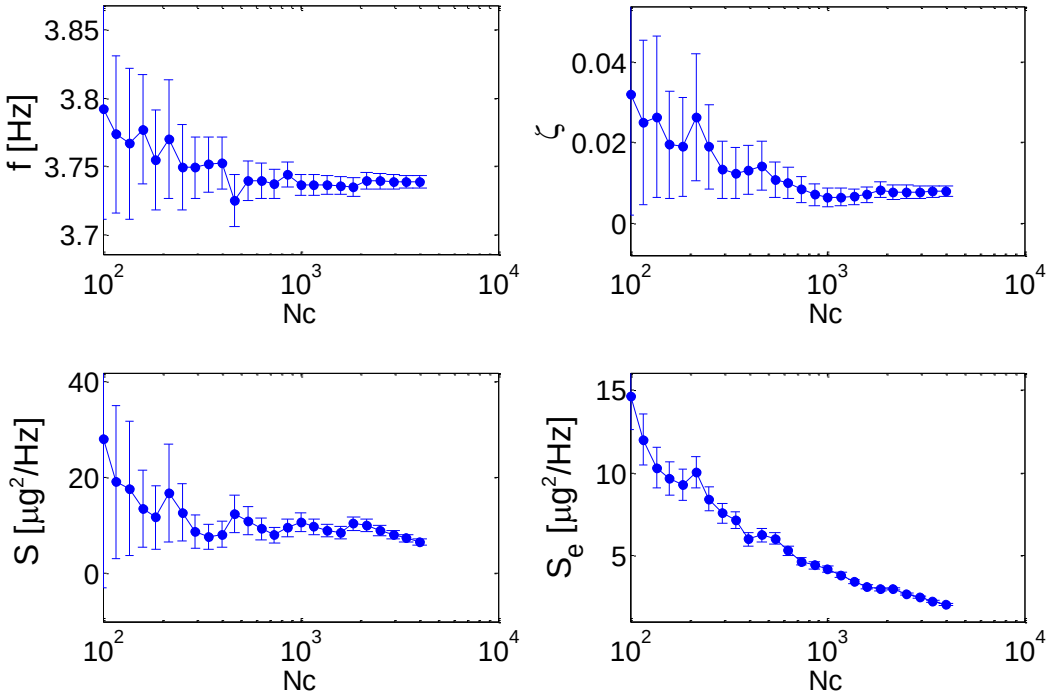

Figure 30 Identified modal parameters (MPVs, blue dots) with ±2 standard derivations (error bars), mode 3, setup 1.

The root SV spectrum with a selected frequency band is plotted using the first setup data (see Figure 29). By applying Bayesian multiple-setup modal identification with a selected frequency band of [3.467 4.067] Hz , the MPV of modal parameters and the posterior variances can be determined. The results of the first setup are shown in Figure 30. As the data length increases, the error bars in the figure shorten. Figure 31 and Figure 32 show the three uncertainty quantities calculated for each modal

parameter. As the data length increases, their values decrease and finally match each other. This validates the long data asymptotic behaviour of the posterior covariance with using field test data.

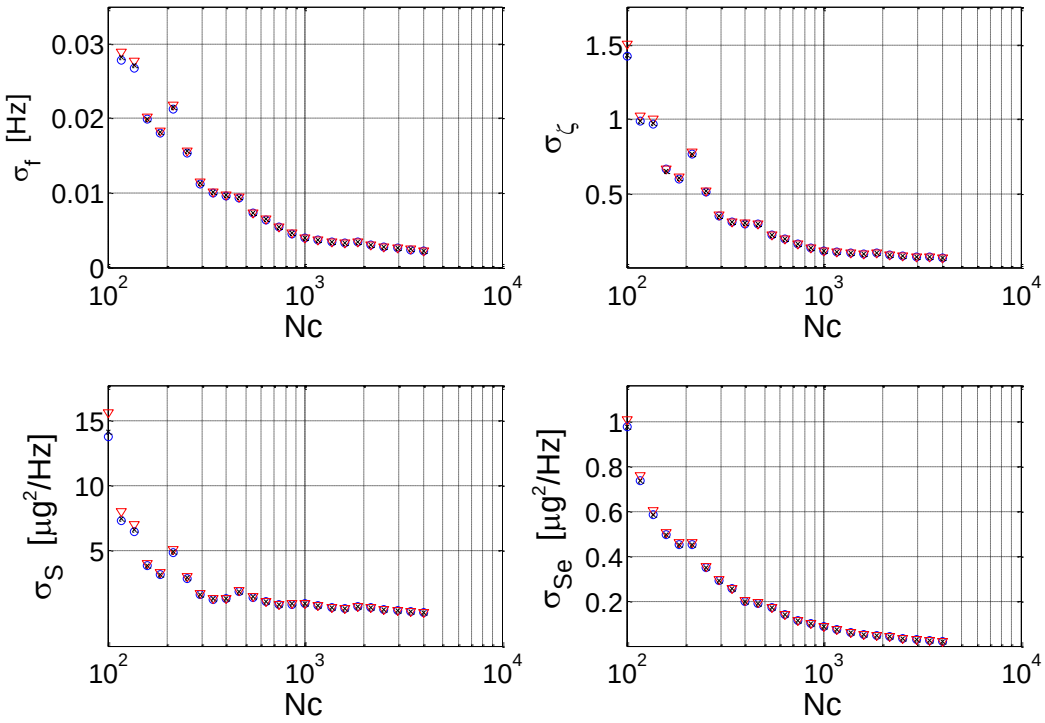

Figure 31 Posterior standard derivation of modal parameters (red triangle), CRB (black cross) and uncertainty law (blue circle), mode 3, setup 1.

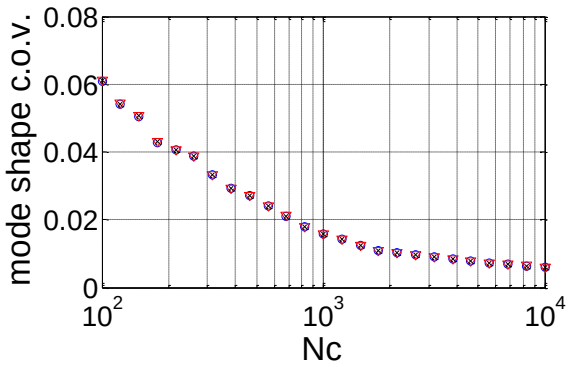

Figure 32 Posterior global mode shape c.o.v. (red triangle), CRB (black cross) and uncertainty law (blue circle), mode 3, setup 1.

4.7 Conclusion

This chapter has investigated the long data asymptotic behaviour of the posterior covariance matrix in multiple-setup OMA. Closed-form expressions of the posterior c.o.v.s of modal parameters have been developed. The relationship between identification uncertainty and multiple-setup test configuration has been established through the posterior global mode shape c.o.v. The theory has been valuated using synthetic, laboratory and field test data.

Aiming at reducing the global mode shape c.o.v. and targeting for a single mode, scientific guidance for multiple-setup ambient vibration test planning has been made. It is suggested that the reference sensors should be placed so that the sum of their squared mode shape values is as large as possible. As long as the reference sensors are deployed in a good position, it does not matter how the roving sensors are planned, since different settings give similar level of global mode shape uncertainty. The above findings simplify the planning of roving sensors so that one can focus on other planning aspects (e.g., logistics). It should be noted that the above recommendations are based on a single mode only. For planning of multiple modes, it requires a trade-off among different modes.

Chapter 5 Field test applications

5.1 Introduction

Full-scale dynamic tests provide valuable information on the performance of structures. In field tests, obtaining good quality and informative data is the first concern. This requires proper instrumentation (e.g., sensor, data acquisition system/ hardware) and test planning. Designing a multiple-setup test involves planning for both reference and roving sensors in different setups. Conventionally, a multiple-setup test is planned primarily based on qualitative judgement, which relies on the operators' knowledge and experience [14,49]. The uncertainty law of multiple setups developed in Chapter 4 reveals the relationship between identification uncertainty and multiple-setup test configuration. This allows test configuration to be planned and quantitatively assessed from an uncertainty point of view.

This chapter presents multiple-setup ambient vibration tests of two civil engineering structures. The first one is an eight-storey office building called the Brodie Tower. The other is the Queen's Park suspension footbridge. Preparation work, such as sensor selection, instrument synchronisation, power and instrument transportation is presented. Multiple-setup planning following conventional practise is presented. The measured data is analysed using a Bayesian modal identification method incorporating multiple-setup data [65]. The posterior covariance matrix is calculated using the method developed in Chapter 3. After modal identification, test configurations are quantitatively assessed using the multiple-setup uncertainty law in Chapter 4.

5.2 Preparation work

Setting up a field test requires consideration of instrumentation, logistics and practical constraints such as accessibility and budget. Preparation work must be carried out ahead of time to ensure that every step in the field test runs properly and smoothly.

Sensor selection

Different types of sensors have different levels of noise. The noise level directly affects the quality of the measured data. For ambient vibration tests, due to the low excitation intensity, the impact of sensor noise on identification precision becomes significant.

The field tests presented in this chapter use triaxial force-balance accelerometers (Guralp Systems Ltd, see Figure 33) to measure ambient vibration data. These accelerometers have a dynamic ranging from $0.1\,\mathrm{g}$ to $2.0\,\mathrm{g}$ and a sampling rate ranging from $1\,\mathrm{Hz}$ to $1{,}000\,\mathrm{Hz}$. The instrument noise is in the order of $0.01\,(\mu g)^2/\mathrm{Hz}$ in the frequencies above $1\,\mathrm{Hz}$. These accelerometers combine a sensor module, a data acquisition system (DAQ) and a Linux system. It can measure, store and transfer data individually, allowing the sensor to continually measure different locations and collect data locally.

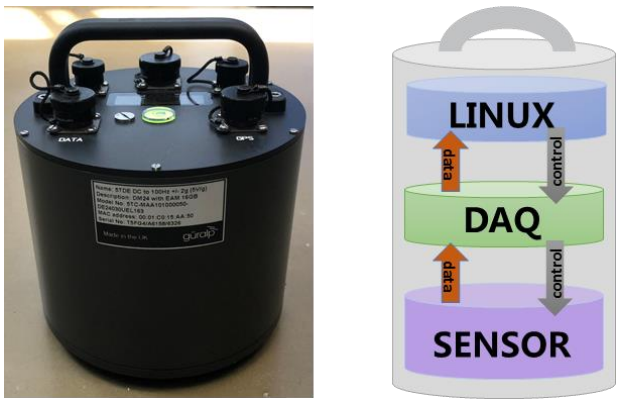

Figure 33 The accelerometer used for field test and its built-in components.

Instrument synchronisation

Instrument synchronisation can be implemented in several ways. A conventional way is to connect multiple sensor units to a central DAQ console (see Figure 34 (a)). In this setting, all the data channels are sampled by the same DAQ. As a result, the acquired data are already synchronised. Although this method of synchronisation is simple and uses fewer devices (i.e., DAQ), it requires long cables to transmit analogue signal from the sensor to the DAQ. This may increase noise or distort the signal by voltage drop. Using long cables is also laborious for field applications.

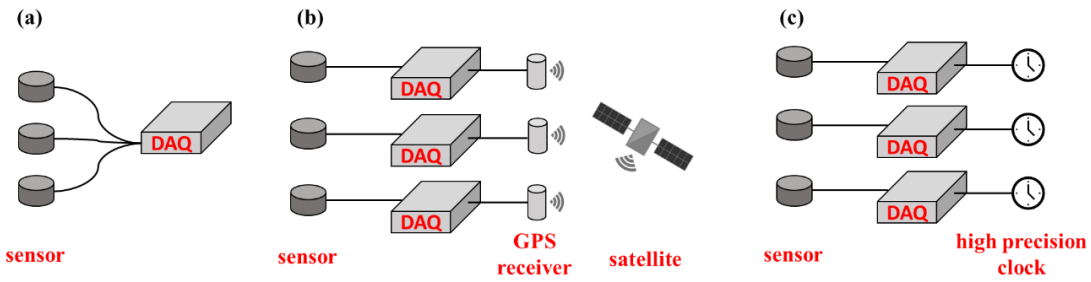

Figure 34 Instrument synchronisation methods.

For a sensor-DAQ integrated device, such as the accelerometers mentioned before (see Figure 33), the analogue signal is acquired locally by its integrated DAQ unit. Instrument synchronisation requires either connecting all the sensors to the same time source or using a high-precision clock for each device. For outdoor measurement, such as for bridges, a GPS (Global Positioning System) receiver is commonly used for receiving time signals from satellites (see Figure 34 (b)). By connecting the GPS receiver with each device, all the sensors will be synchronised and will receive the same time stamp from the GPS. For indoor tests, such as for buildings, where the GPS signals can be weak, GPS may not be applicable. Alternatively, each sensor can connect to a high-precision clock (see Figure 34 (c)). This clock can provide very

accurate time for the sensor. The high-precision clocks have to be synchronised ahead of the field test. Once they are synchronised, the clocks are able to continually provide synchronised time, for a reasonable amount of time.

The field tests on the two structures use GPS receivers and high-precision clocks for time synchronisation. The high-precision clock has an accuracy of 0.038 ppm (parts per million), which means that the relative time drift is approximately $2\times0.038\times10^{-6}\times3600\times12 \approx 3$ milliseconds for over 12 hours. For low to moderate frequencies, e.g., smaller than 100 Hz , this time drift is considered to be acceptable.

Power and instrument transportation

In the selection of power for field test instruments, consideration should be given to its stability and capacity. Mobility also needs to be considered, since it is common to have power transported with sensors during the test. Instrument transportation affects the total time requirement. Considering the time constraint (e.g., accessibility to the site), it is necessary to use well-packed equipment and have well-organised logistics.

For the field tests presented in this work, a set of equipment including an accelerometer, a GPS receiver, a high-precision clock, a battery and other accessories (e.g., cables) are packed in a water-proof rugged case, which is in-house designed for mobile instrument transportation (see Figure 35). The battery is of lithium-ion polymer type with a capacity of 16 Ah (Ampere hour). It can continually power a set of instrument for approximately two days.

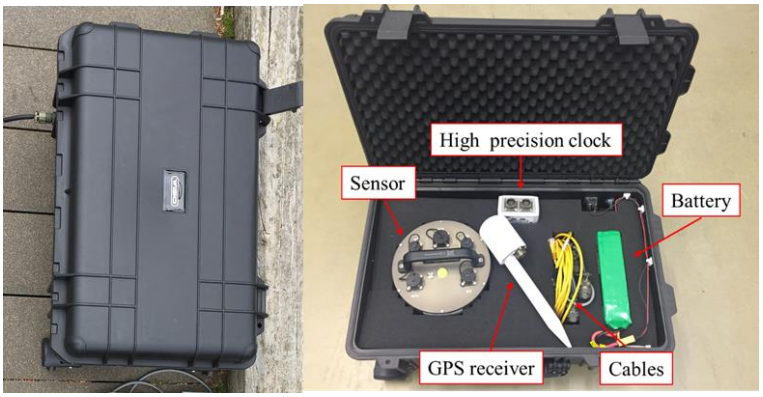

Figure 35 A set of equipment per test location.

5.3 Multiple-setup planning

In the planning of reference sensors, the primary considerations are to avoid nodes of potential modes and obtain as much informative data as possible. This requires the reference locations to have as large modal response as possible, which implies that the reference sensors should be placed where the mode shape values are as large as possible. Beside this, in order to simplify planning, it is common to have fixed reference locations for all the setups. Regarding the number of reference sensors, it is suggested to use as few as necessary, since having more reference sensors means fewer roving sensors and thus more setups. Assuming that the reference locations are able to provide sufficient information for modal identification, the planning of roving sensors can focus on satisfying other constraints (e.g., logistics) rather than identification precision.

The uncertainty law of multiple setups developed in Chapter 4 reveals the relationship between identification uncertainty and test configuration, which allows the multiple setups to be designed from an uncertainty point of view. The scientific guidance based on the uncertainty law (see Section 4.5) coincides with the above suggestions based on qualitative judgement.

5.4 The Brodie Tower

5.4.1 Building description

The Brodie Tower is an office building situated on the central school campus of the University of Liverpool, England (see Figure 36). It was built in the late 50s with concrete and bricks. It has eight storeys with a total height of approximately 25 m. The floor slabs are 'T-shaped' and span an area of 25 m × 28 m. The building houses the civil engineering department, with a structural and material laboratory located in the basement. The remaining floors are home to mainly offices and lecture rooms.

Figure 36 Overview of the Brodie Tower.

5.4.2 Test configuration

A full-scale ambient vibration test with multiple setups was performed on the Brodie Tower in May, 2016. Five force-balance triaxial accelerometers were deployed for the test. In view of the building floor plan (see Figure 37 (a)), the intention was to obtain a mode shape that resolves into the 'T-shape'. Considering the number of available sensors, four locations on each floor were measured, yielding a total of 84 DOFs. In

order to facilitate alignment, the sensors were placed in the corridors and their orientation was along the frame direction of the building (see Figure 37 (a)).

The sensor location plan is shown in Figure 37 (a), where ① to ④ are roving sensor locations for each floor and Ⓡ is the reference location only placed on the top floor. The roving sensors were roved from the top floor (7F) to the bottom floor (1F) (see Figure 37 (b)). A total of seven setups gave 7×4=28 measured locations.

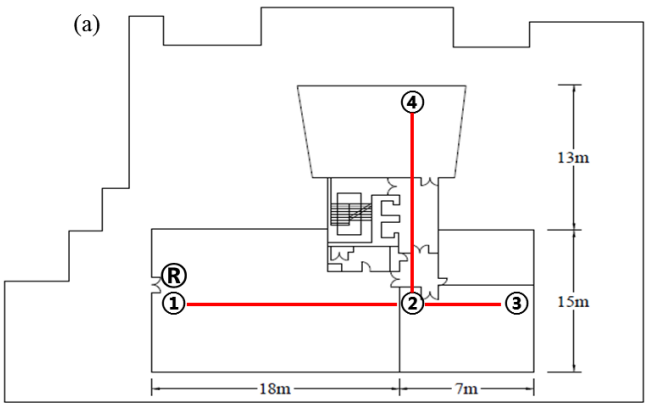

(b)

Setup No.	Floor No.	Roving direction
1	7F	
2	6F	
3	5F	
4	4F	
5	3F	
6	2F	
7	1F	

Figure 37 (a) Floor plan and sensor locations; (b) setup plan.

The ambient vibration data were measured with a sampling rate of 50 Hz . Since the majority of the measurements were taken from the indoor area, a high-precision clock was used for instrument synchronisation (see Figure 38). In each setup, the data was recorded for 20 minutes. The transition between setups took approximately 5 minutes. Instrument synchronisation in advance took approximately 20 minutes. In total it took approximately 20+(20+5)×7 = 3.25 hours from 1:30 pm to 4:45 pm.

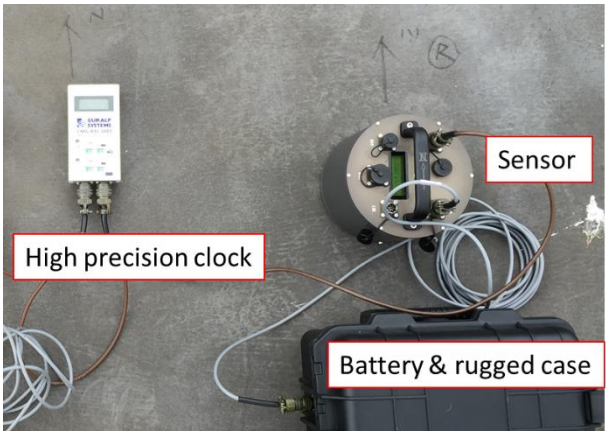

Figure 38 A set of equipment per location (synchronisation using a high-precision clock).

5.4.3 Modal identification

The root SV spectrum is first examined to locate potential modes (see Figure 39). Six potential modes below 10 Hz with the selected frequency bands are highlighted. The peaks of the first three modes are significantly above the remaining lines, which indicates high s/n ratios. The s/n ratios of the fourth, fifth and sixth modes are relatively low compared to the first three modes.

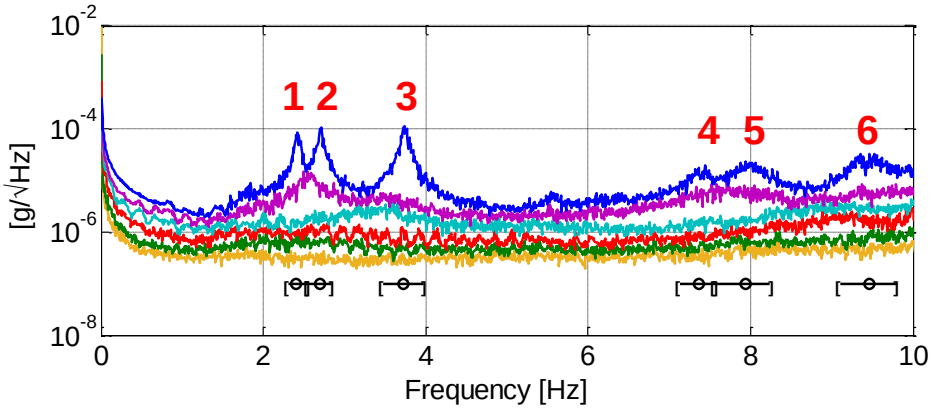

Figure 39 The root SV spectrum with selected frequency bands using the first setup data.

Identification results

Figure 40 shows the identified natural frequencies and damping ratios among setups. The blue circles represent the MPV of the modal parameters and the error bars cover

twice the posterior standard deviation. It can be seen that the identification results vary among setups. The variability of the natural frequencies is relatively small compared to that of the damping ratios.

The sample means and sample c.o.v.s of the modal parameters are shown in Table 5. The sample mean is calculated by averaging the MPV of the modal parameters across different setups. The sample c.o.v. is different from the posterior c.o.v. It is the standard derivation of the MPV among setups, which reflects the statistical variability of the identified modal properties. It can be seen that the sample c.o.v.s of the damping ratios are much larger than that of the natural frequencies.

Table 5 The sample means and sample c.o.v.s of the natural frequencies and damping ratios.

		Mode					
		1	**2**	**3**	**4**	**5**	**6**
Natural Frequency	mean (Hz)	2.422	2.707	3.750	7.405	7.995	9.782
	c.o.v. (%)	0.18	0.23	0.24	0.22	0.29	0.73
Damping Ratio	mean (%)	1.031	0.905	0.754	2.525	2.624	6.439
	c.o.v. (%)	13	15	9	12	10	26

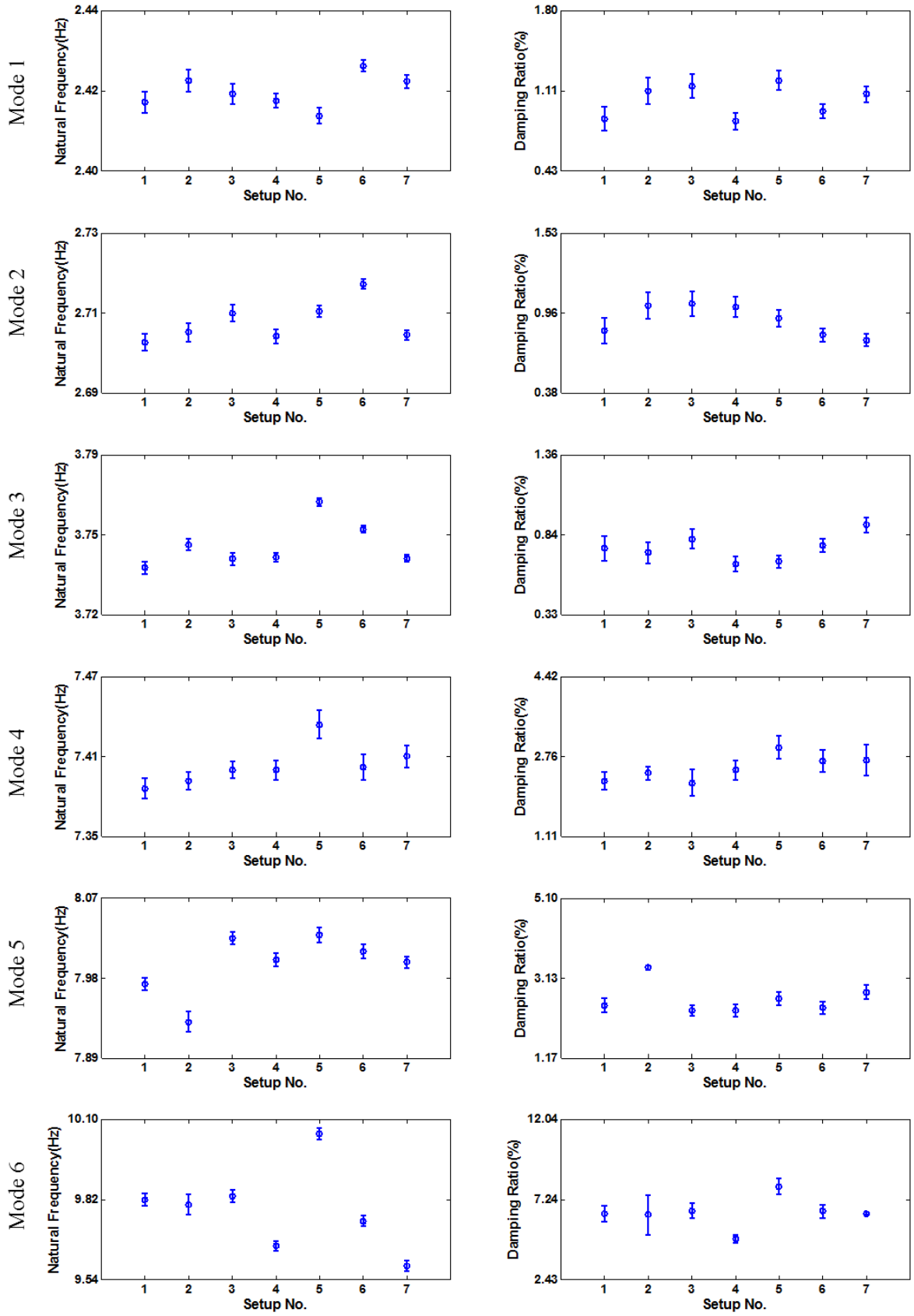

Figure 40 The identified natural frequencies and damping ratios among setups, the error bars cover +/- 2 standard deviations.

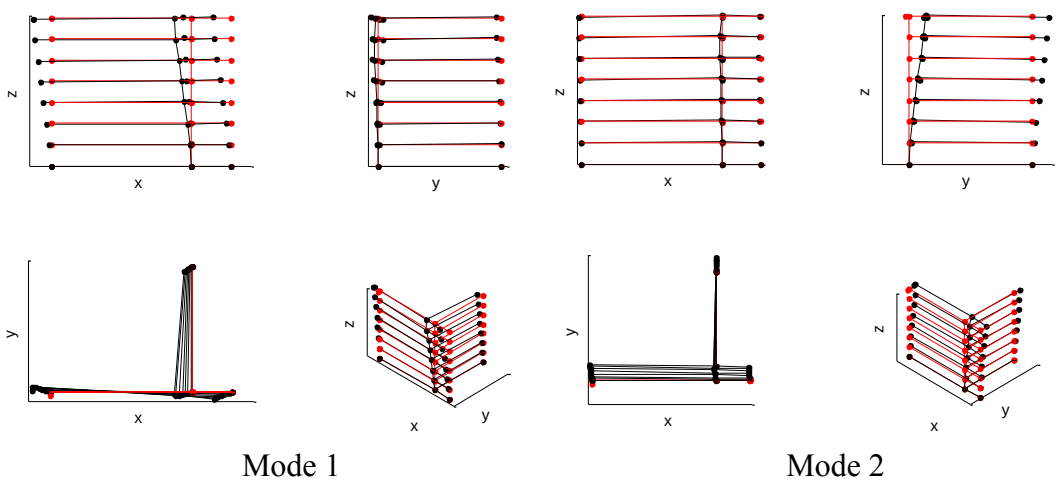

Figure 41 Global mode shapes of modes 1 and 2.

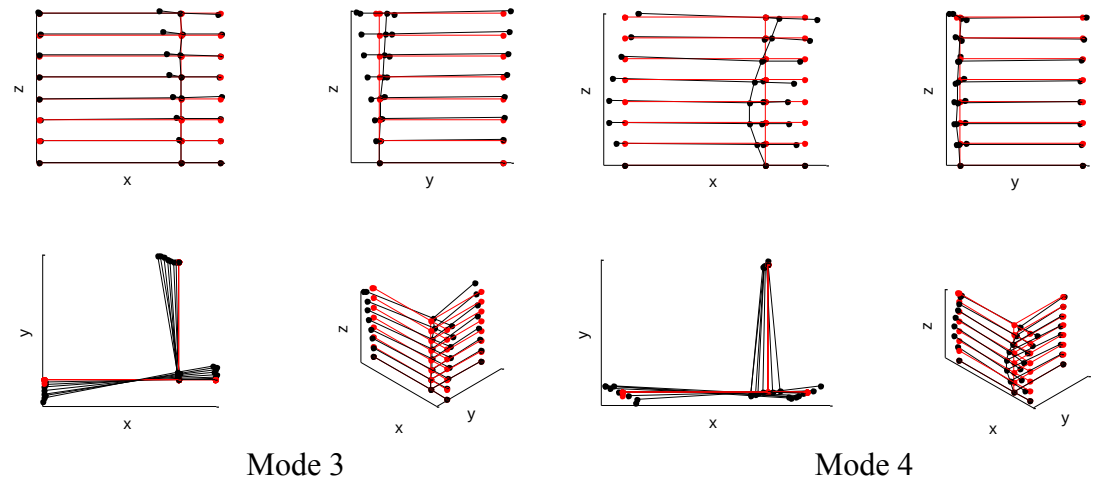

Figure 42 Global mode shapes of modes 3 and 4.

Global mode shapes

Figure 41 to Figure 43 show the global mode shapes of the first six modes. It can be seen that mode 1 is dominated by the building translational mode in the x-direction. A slight rotation in plan view can also be found, which may due to the mass distribution of the building. Mode 2 is dominated by a translational mode along the y-direction. Mode 3 is a torsion mode, where the rotation centre is on the left side of the 'T' shape. Mode 4 is a combination of the second translational mode in the x-direction and a

torsion mode. Mode 5 is the second translational mode in the y-direction. Mode 6 is a combination of the vertical motion and the second translational mode in the y-direction.

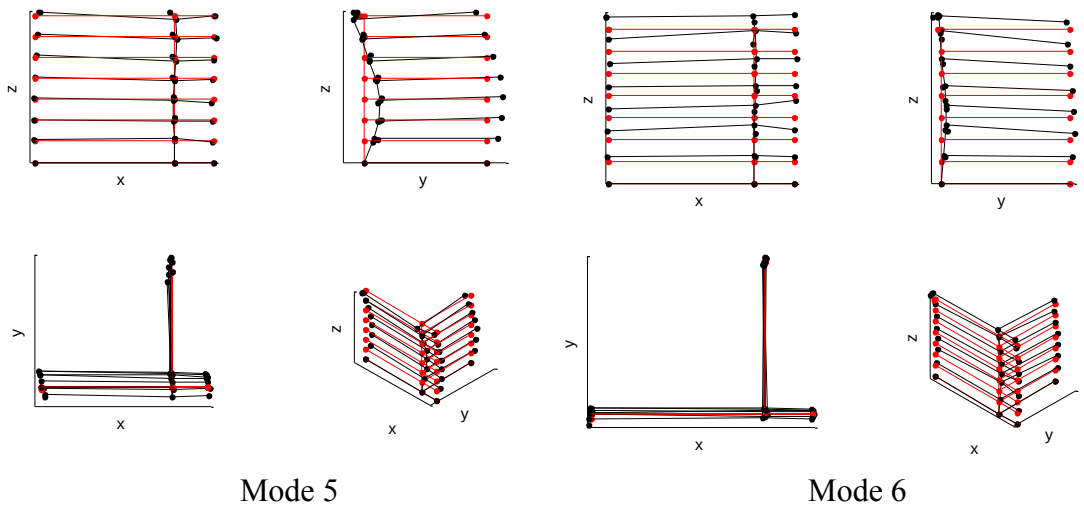

Figure 43 Global mode shapes of modes 5 and 6

5.4.4 Test configuration assessment

Using the uncertainty law developed in Chapter 4, the posterior global mode shape c.o.v. can be calculated for different setup configurations. The building was measured in a total of 28 locations with one reference sensor and four roving sensors. The reference location then has 28 possible choices. The global mode shape c.o.v. can be calculated for all the possible choices of the reference location. For each mode, the c.o.v.s are plotted with c_{ref} (the sum of the squared mode shape values at the reference locations), which is shown in Figure 44 with blue dots. The global mode shape c.o.v.s for the current setting are indicated as red circles in the figure. It can be seen that the global mode shape c.o.v.s decrease with c_{ref} and converge to a common value. This is consistent with the theory in Section 4.5, demonstrating that a higher value of c_{ref} leads to a lower global mode shape uncertainty. The figure also shows that, for modes

1-4, the global mode shape c.o.v.s based on the current setup configuration are closed to the converged values. From the global mode shapes in Figure 41 to Figure 43, it can be seen that the current setting of the reference location (i.e., one corner of the top floor) for modes 1-4 gives relatively large global mode shape values. In contrast, for modes 5 and 6, the c.o.v.s for the current setting are not as close to the converged values. From the global mode shape plots, it can be seen that the current reference location does not produce large mode shape values. Correspondingly, their global mode shape c.o.v.s are larger than those of modes 1-4.

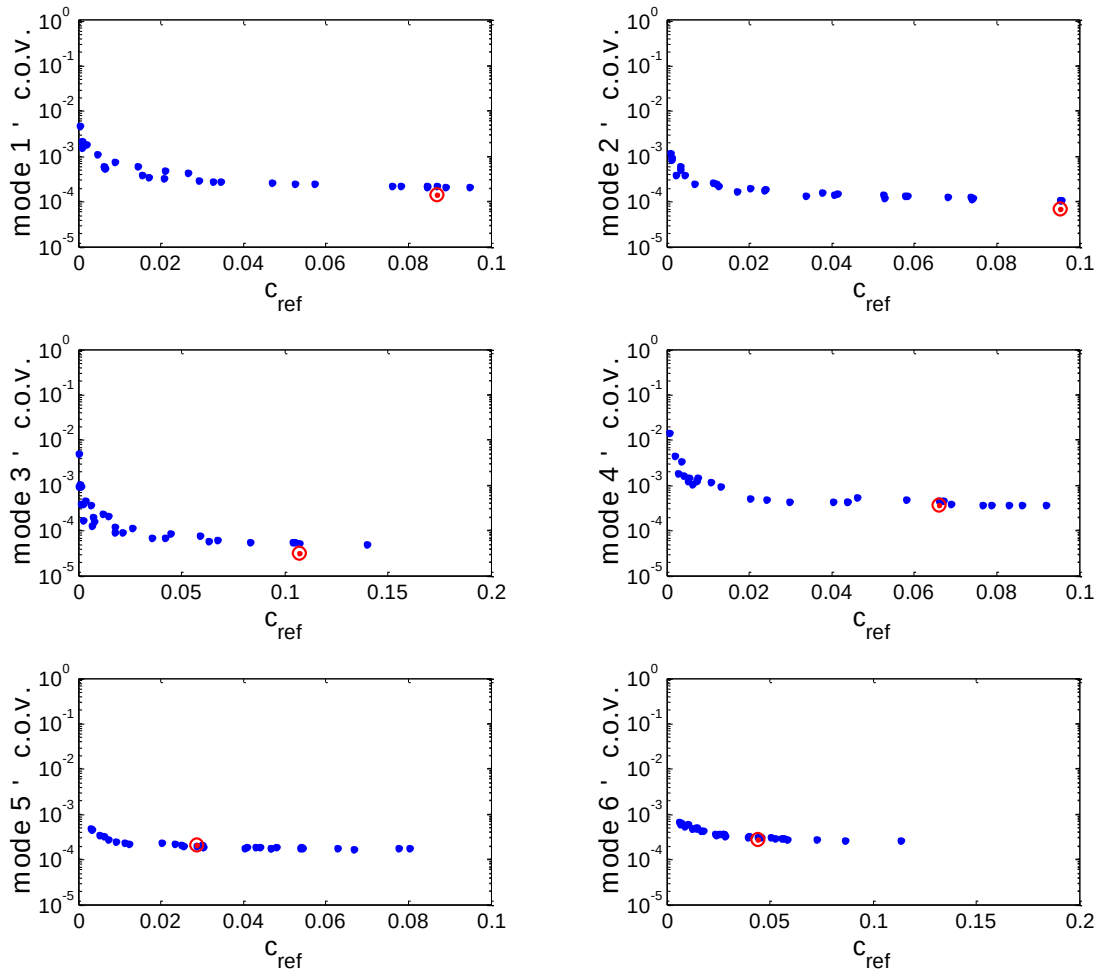

Figure 44 Global mode shape c.o.v.s to the different choices of reference locations (red circles denote current configuration, blue dots denote all the possible settings).

By comparing the current reference location with all the other possible choices, it can be seen that, for identifying modes 1-4, the current setting is able to provide enough accuracy on identifying the global mode shapes. For the modes 5 and 6, the global mode shape uncertainties are larger compared to those of the first four modes.

5.5 The Queen's Park suspension footbridge

5.5.1 Bridge description

The Queen's Park suspension footbridge is located in Chester city centre, England (see Figure 45). It was built in 1923, and later refurbished and reopened in 2012. The footbridge provides pedestrian access between the Queen's Park area and the southern bank. The main span of the bridge is 85 m long and both sides spans are 25 m long. The main structure of the bridge was built with steel members. The deck measures 3.5 m in width and was paved with timber and an anti-slip layer.

Figure 45 The Queen's Park suspension bridge.

5.5.2 Test configuration

In order to capture as much detail of the bridge as possible, the field test was planned to measure a total of 66 locations. Figure 46 shows the plan view of the bridge with selected locations for data measurement. The locations were distributed all over the bridge on both sides along the longitudinal directions (see Figure 46, the locations of 101-133 from one side and those of 201-233 from the other side).

In the field test, six triaxial force-balance accelerometers were deployed for the measurement. To simplify setup planning and facilitate logistics, the reference locations were planned to be fixed for all the setups. To avoid nodes of potential modes and to obtain as large modal response as possible, two reference locations were planned and their positions are shown in Figure 47, denoted by ®. The remaining four roving sensors roved from setup 1 towards the southern bank side until all the DOFs were covered. A total of 16 setups were required for the test.

Ambient vibration data was measured for 20 minutes for each setup with a sampling rate of 200 Hz . The instruments were synchronised through GPS receivers (see Figure 48). Instrument synchronisation took approximately 20 minutes. The transition between setups took around 5 minutes. With 16 setups, it took in total 20+(20+5)×16 = 7 hours. The test was conducted on September 22, 2017, from 10:00 am to 5:00 pm.

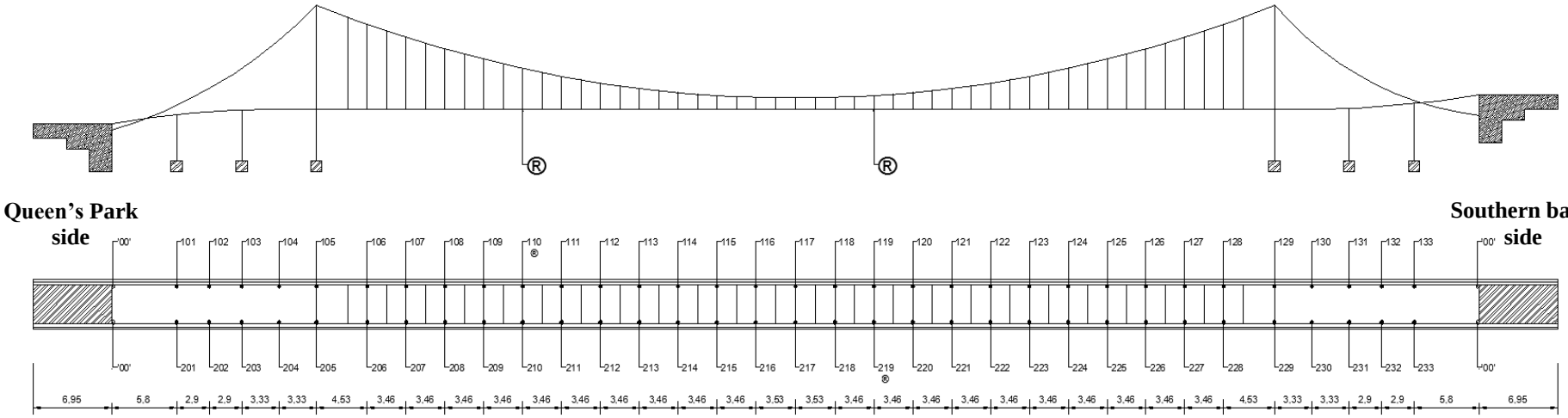

Figure 46 The plan view of the bridge with measured locations (® denotes reference locations).

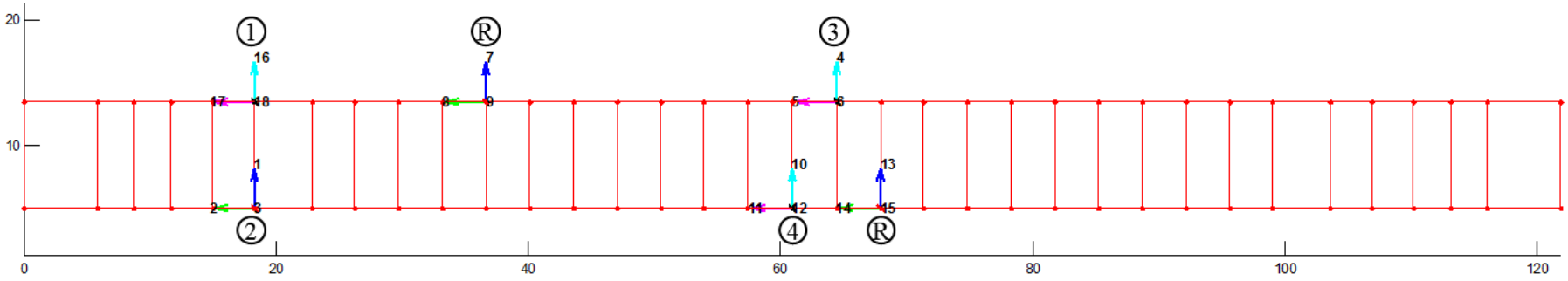

Figure 47 The first setup plan.

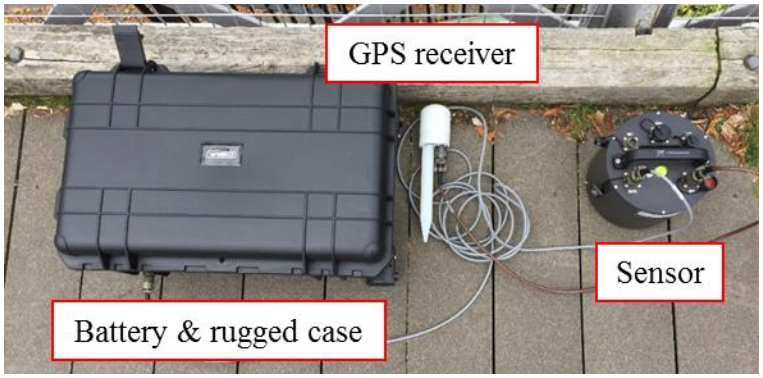

Figure 48 A set of test equipment per location.

5.5.3 Modal identification

The root SV spectrum is first examined to locate potential modes (see Figure 49 for the first setup). Eleven potential modes below 15 Hz are highlighted for modal identification. The selected frequency bands are also indicated.

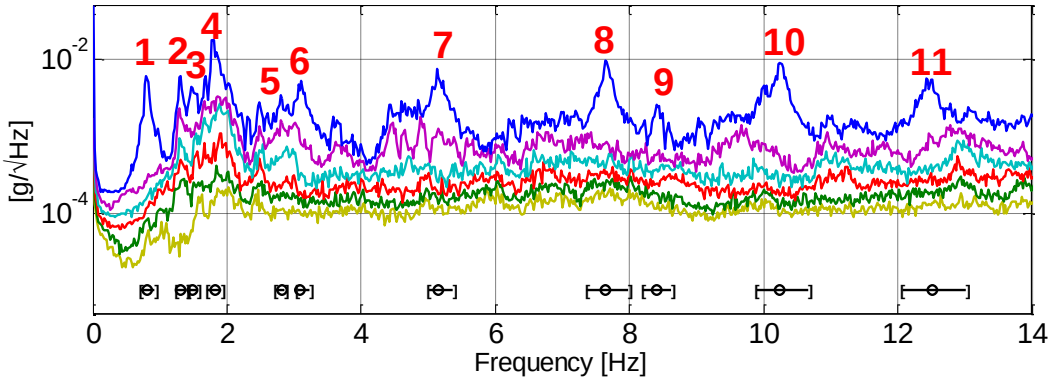

Figure 49 The root SV spectrum with selected frequency bands using the first setup data.

Identification results

Figure 50 and Figure 51 show the plots of the identified natural frequencies and damping ratios in different setups. The blue circles represent the MPV of the modal parameters. The error bars cover twice the posterior standard deviation. It can be seen that the identified natural frequencies and damping ratios vary among setups. The variations of the natural frequencies are generally smaller than those of the damping

ratios. It can also be seen that the identification uncertainties in some modes and setups are significantly large. For instance, the uncertainty of the natural frequencies in mode 1 setup 14 , mode 3 setup 7 and mode 5 setup 9 is much larger than that of the remaining modes among setups. One possible reason is that the identified mode in that particular setup is not well-excited during the measurement.

The sample means and sample c.o.v.s of the natural frequencies and damping ratios among setups are shown in Table 6. Except for modes 1 and 6, the variations of the remaining natural frequencies in different modes are smaller than 1%. In contrast, for the damping ratios, the majority of the sample c.o.v.s are in the range of 20%-50%. This reflects a high variation of the identified damping ratios.

Table 6 The sample means and sample c.o.v.s of the natural frequencies and damping ratios.

		Mode										
		1	**2**	**3**	**4**	**5**	**6**	**7**	**8**	**9**	**10**	**11**
Natural Frequency	mean (Hz)	0.78	1.3	1.47	1.80	2.8	3.05	5.15	7.65	8.41	10.2	12.5
	c.o.v. (%)	2.2	0.35	0.69	0.86	0.99	2.1	0.27	0.2	0.16	0.18	0.18
Damping Ratio	mean (%)	3	0.98	2.2	1.4	1.3	1.8	0.74	0.68	0.76	0.7	0.76
	c.o.v. (%)	35	33	46	34	57	83	30	24	27	29	17

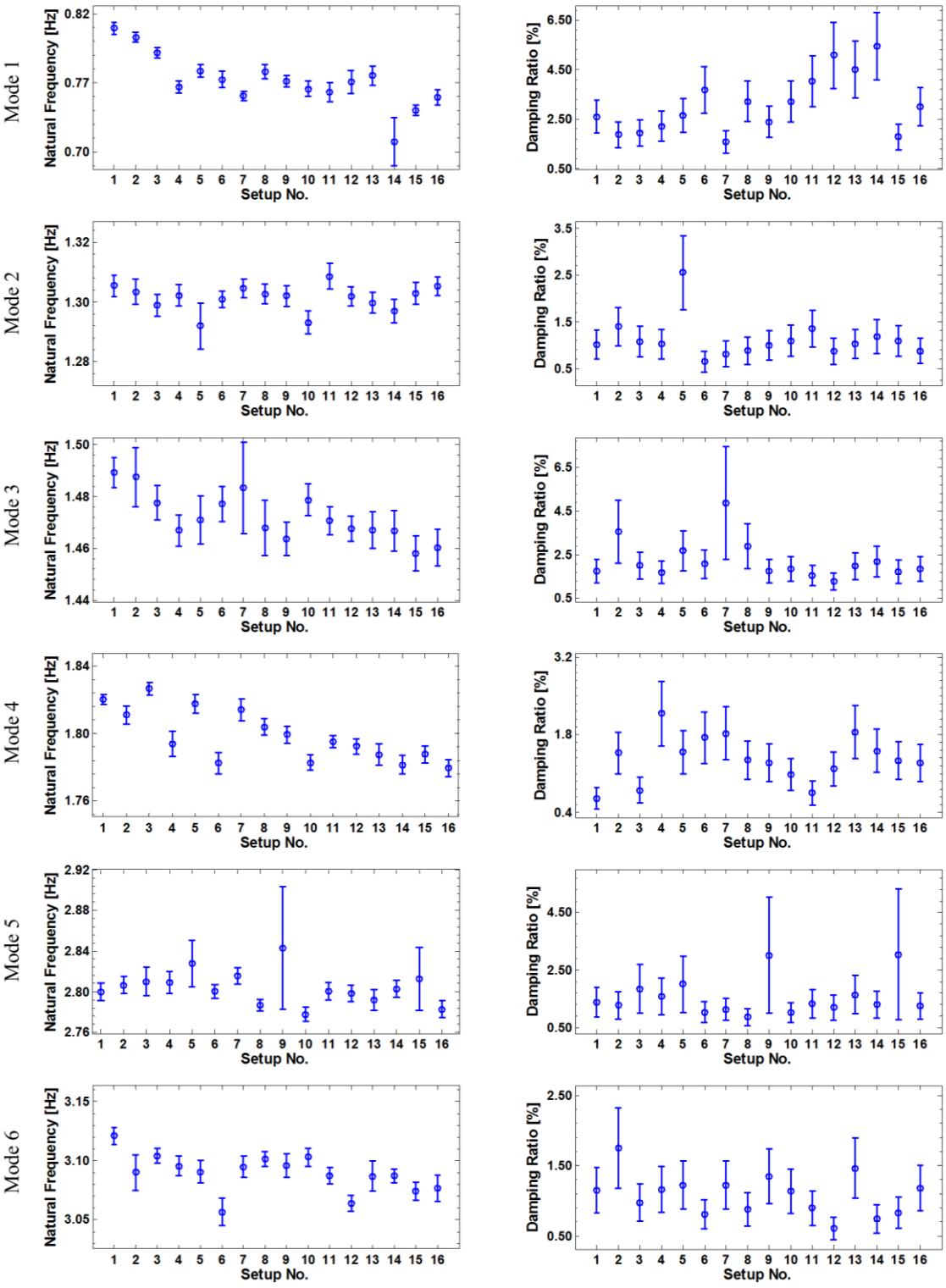

Figure 50 The identified natural frequencies and damping ratios of the modes 1 to 6 among setups, the error bars cover +/- 2 standard deviations.

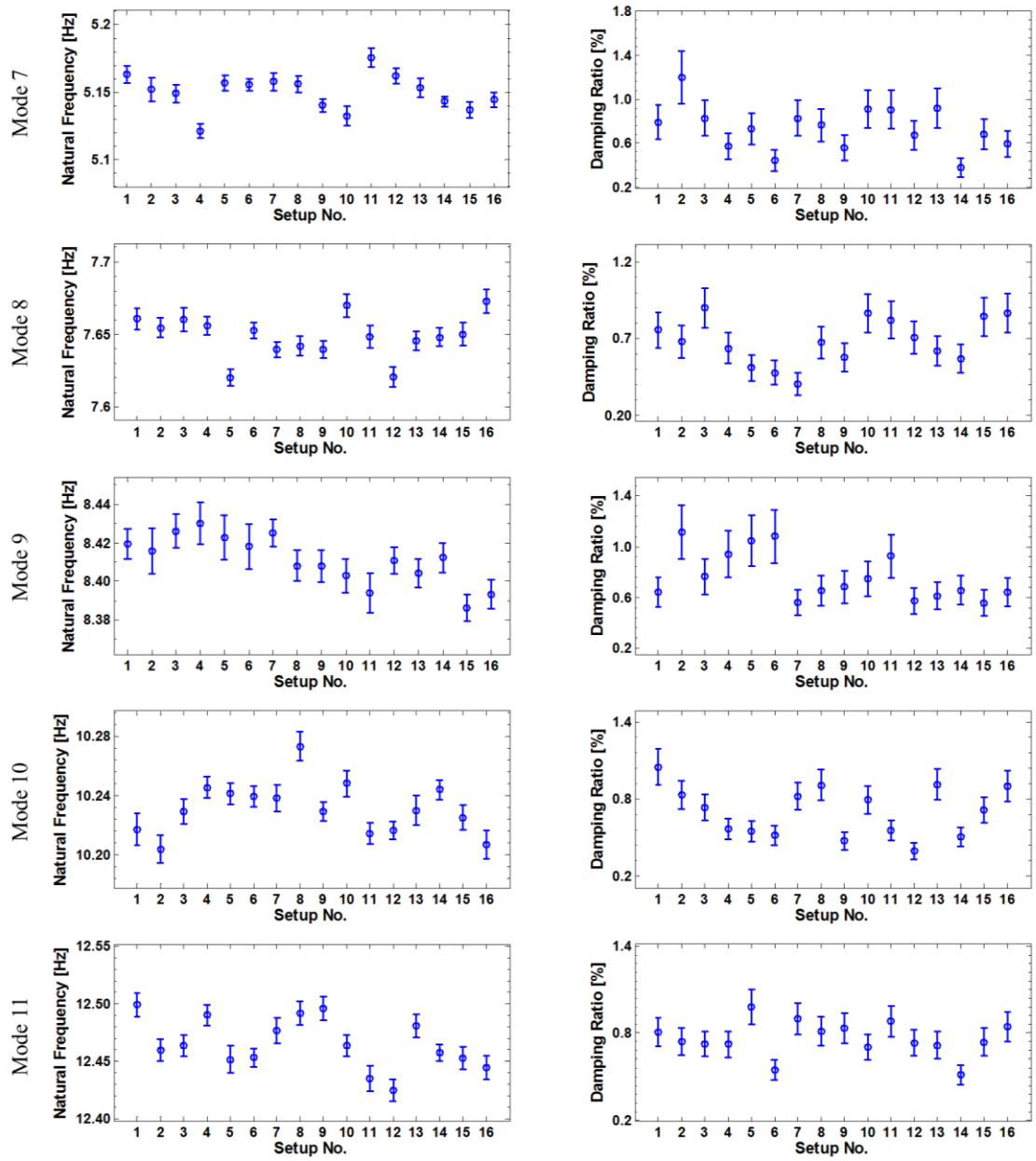

Figure 51 The identified natural frequencies and damping ratios of the modes 7 to 11 among setups, the error bars cover +/- 2 standard deviations.

Global mode shapes

The global mode shapes are plotted in Figure 52 to Figure 62. Modes 1 and 2 are primarily the first translational mode in the transverse and vertical direction, respectively. Mode 3 is the second translational mode in the vertical direction. Mode 4 is a torsional mode with a rotation centre along the longitudinal direction. Mode 5 is

a combination of the third torsional mode and the translational mode in the transverse direction. Modes 6, 7 and 8 are the third, fourth and fifth translational modes in the vertical direction, respectively. Mode 9 combines the sixth torsional mode and the translational mode in transverse direction. Modes 10 and 11 are the sixth and seventh translational modes in the vertical direction, respectively.

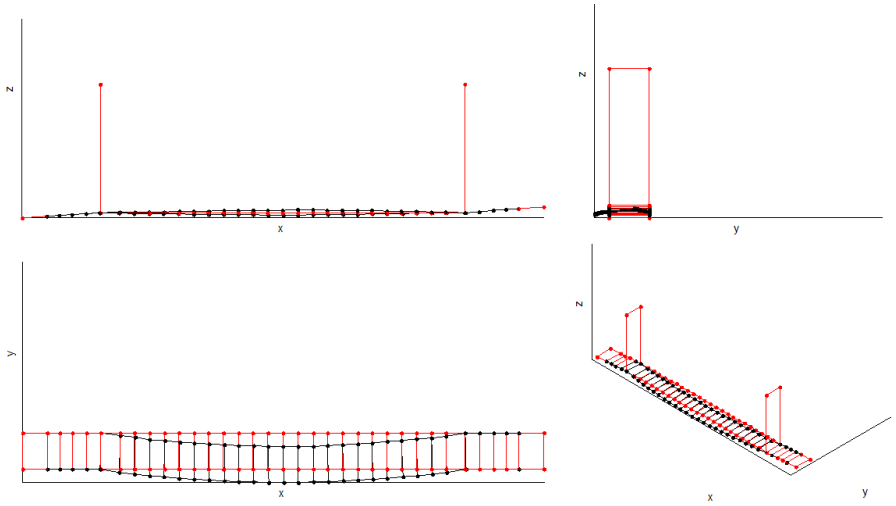

Figure 52 Global mode shape of mode 1 (natural frequency 0.78 Hz, damping ratio 8%).

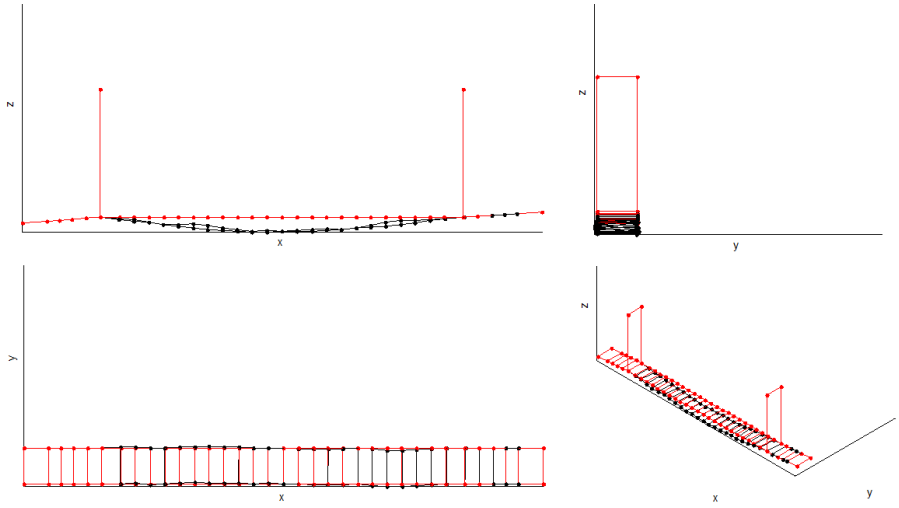

Figure 53 Global mode shape of mode 2 (natural frequency 1.3 Hz damping ratio 0.98%).

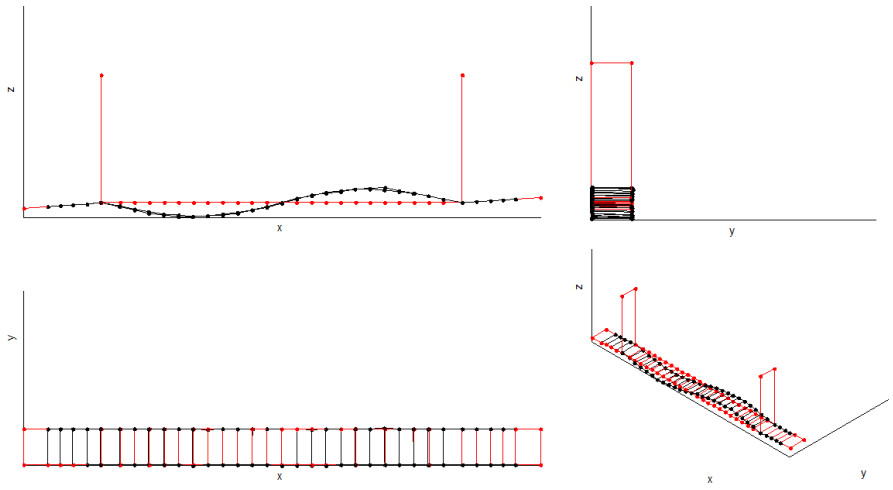

Figure 54 Global mode shape of mode 3 (natural frequency 1.47 Hz, damping ratio 2.2%).

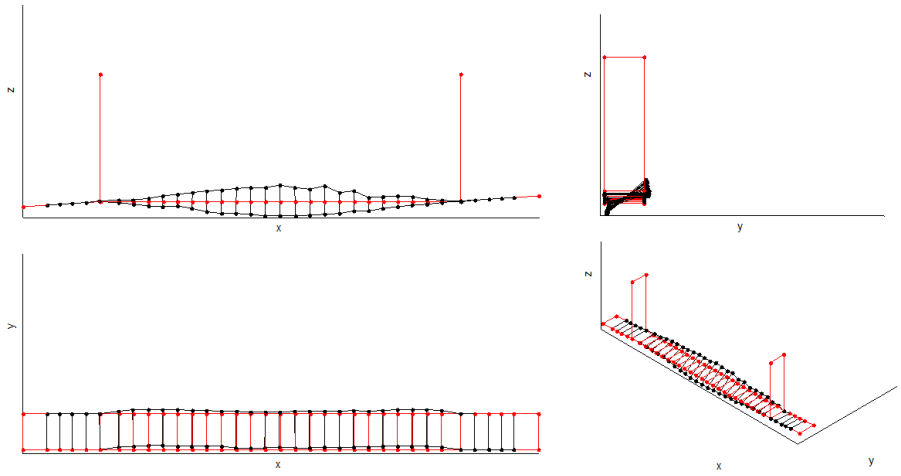

Figure 55 Global mode shape of mode 4 (natural frequency 1.80 Hz, damping ratio 1.4%).

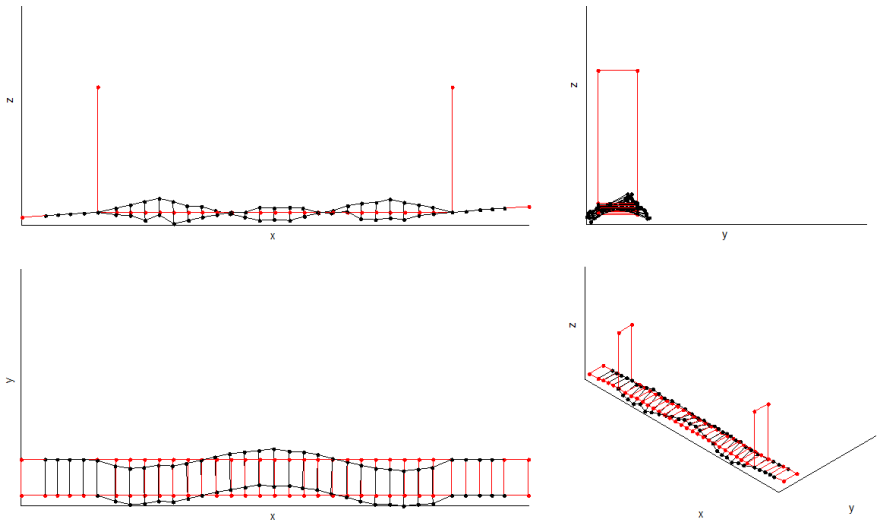

Figure 56 Global mode shape of mode 5 (natural frequency 2.8 Hz, damping ratio 1.3%).

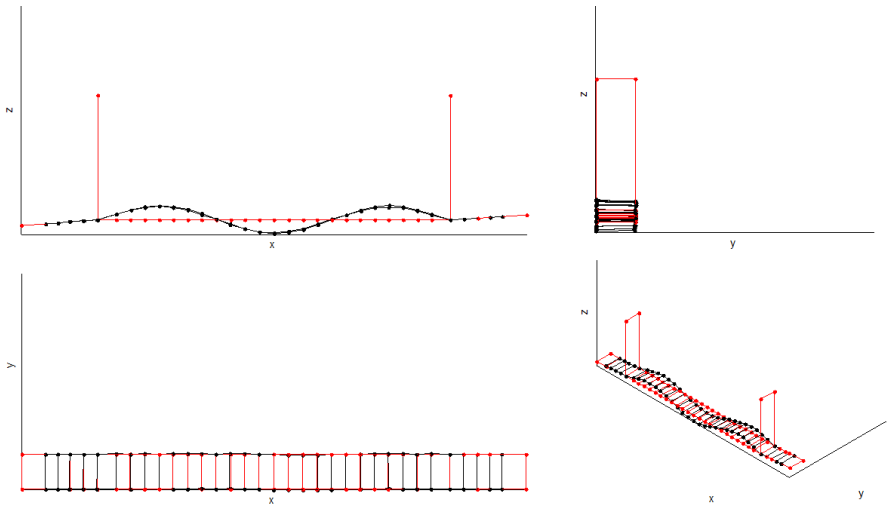

Figure 57 Global mode shape of mode 6 (natural frequency 3.05 Hz, damping ratio 1.8%).

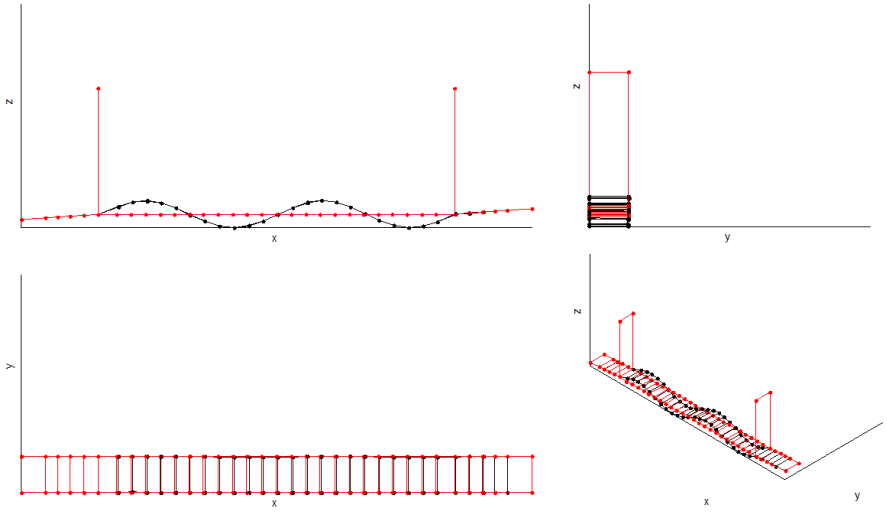

Figure 58 Global mode shape of mode 7 (natural frequency 5.15 Hz, damping ratio 0.74%).

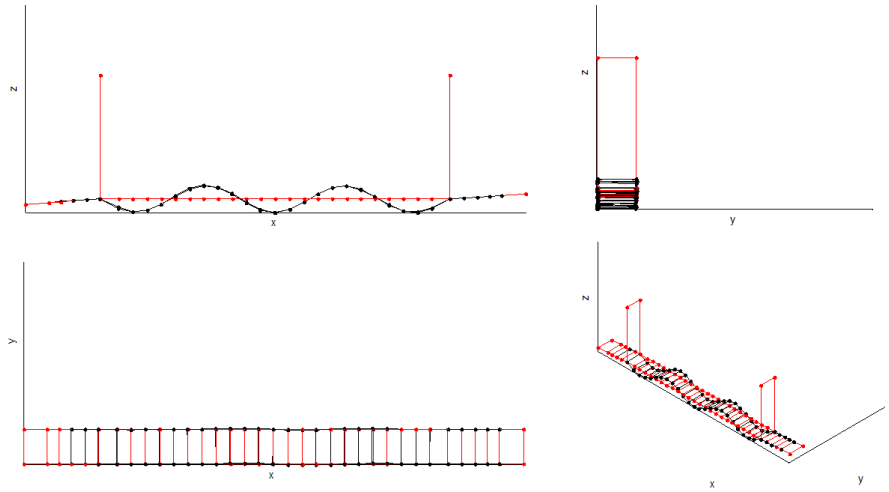

Figure 59 Global mode shape of mode 8 (natural frequency 7.65 Hz, damping ratio 0.68%).

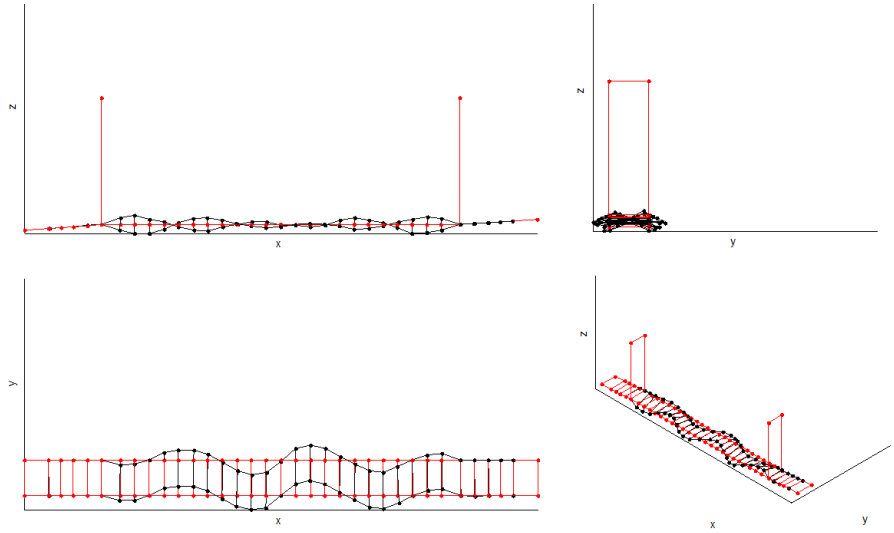

Figure 60 Global mode shape of mode 9 (natural frequency 8.41 Hz, damping ratio 0.76%).

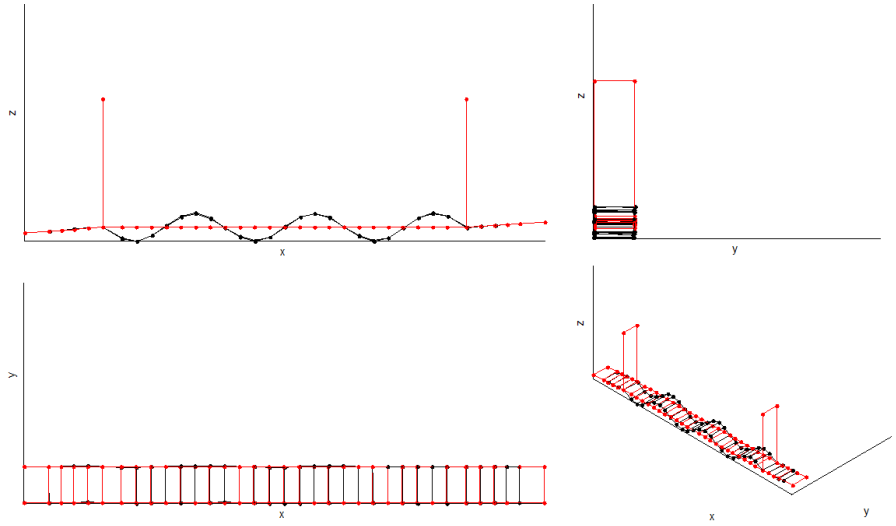

Figure 61 Global mode shape of mode 10 (natural frequency 10.2 Hz, damping ratio 0.7%).

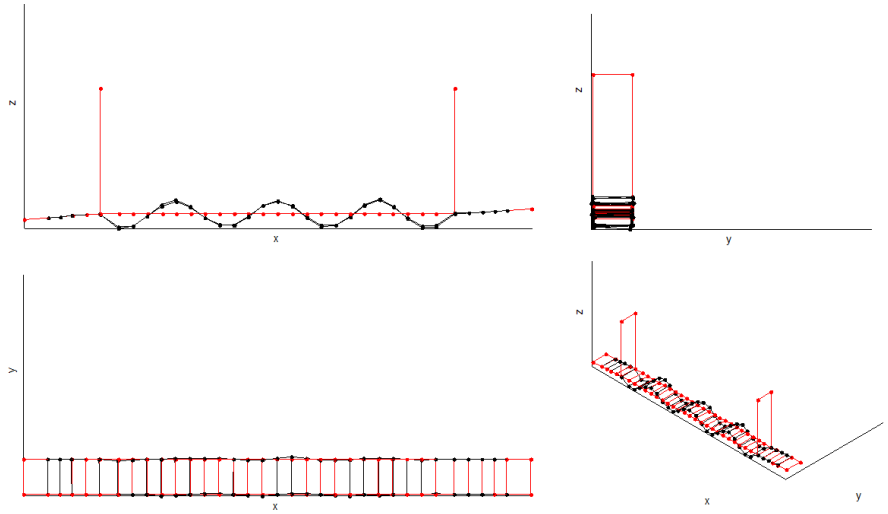

Figure 62 Global mode shape of mode 11 (natural frequency 12.5 Hz, damping ratio 0.76%).

5.5.4 Test configuration assessment

The multiple-setup test configuration of the Queen's Park suspension footbridge is assessed using the multiple-setup uncertainty law developed in Chapter 4. The bridge was measured in 66 locations with two references sensors and four roving sensors. Focusing on the reference locations, the number of possible choices is $C_{66}^{2} = 2145$. The global mode shape c.o.v.s are calculated based on different settings. Results for different modes are plotted w.r.t. c_{ref} (see Figure 63). The blue dots in the figure indicate the global mode shape c.o.v.s that are calculated based on all the possible choices of the reference locations. The red circles represent the results calculated using the current setting. It can be seen that, as c_{ref} increases, the global mode shape c.o.v.s decrease and converge. This again demonstrates that the larger the value of c_{ref}, the smaller the uncertainty of the global mode shape. The figure also shows that, except for mode 8, the global mode shape c.o.v.s produced by the current test configuration are close to the minimum values. This implies that the current setting is able to provide enough accuracy for identifying the global mode shapes. For mode 8, the c.o.v. is slightly larger than the minimum value, which implies that the current setting may not be able to provide enough accuracy. Viewing the plots of the global mode shape from Figure 52 to Figure 62, it can be seen that the current reference locations yield large mode shape values. For mode 8, the global mode shape values at reference locations are slightly smaller. Overall, using the current test configuration, it is able to provide identification accuracy to an acceptable level.

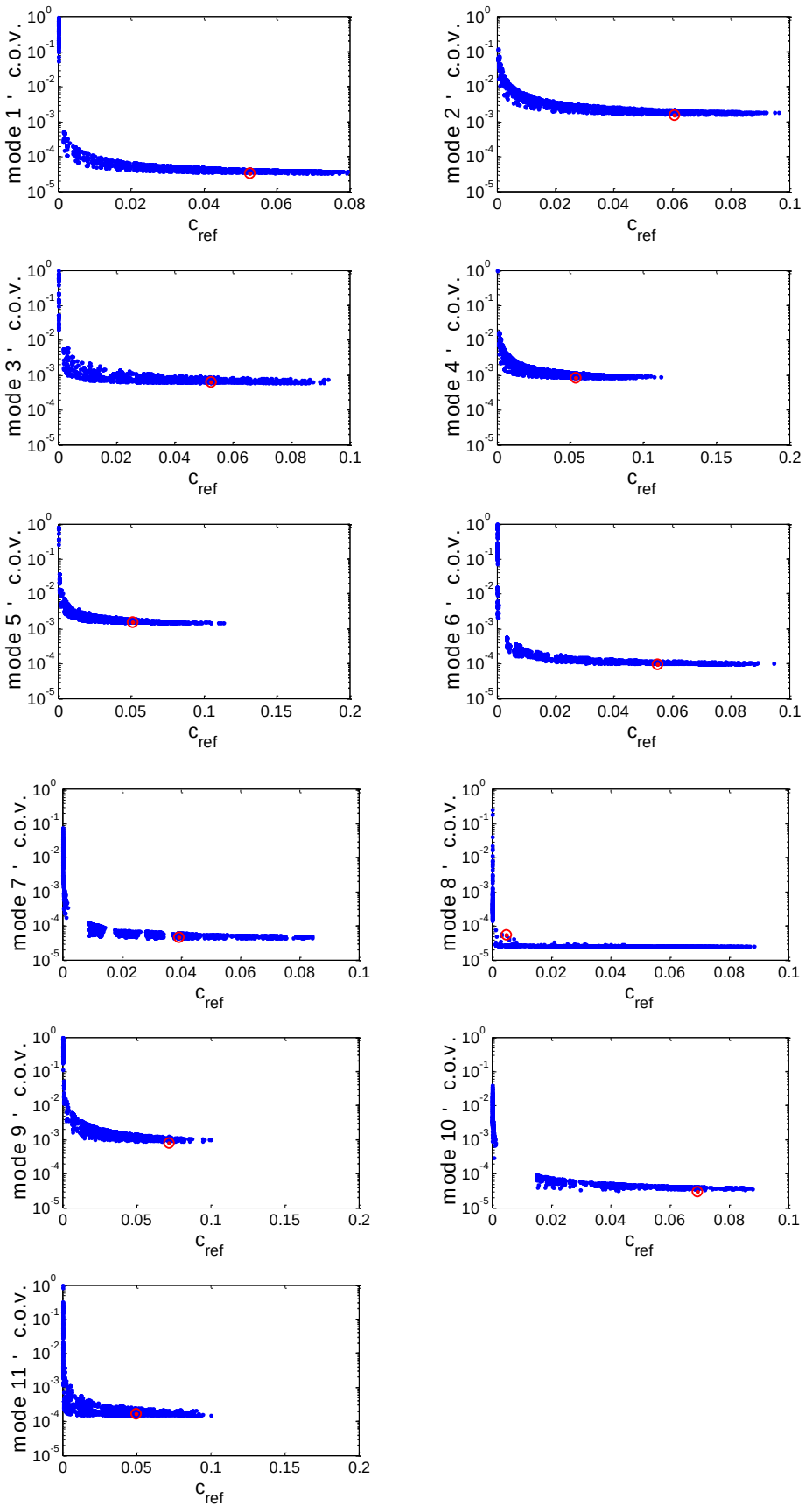

Figure 63 Global mode shape c.o.v.s to the different choices of reference locations (red circles denote current config, blue dots denote all the possible settings).

5.6 Conclusion

This chapter has presented the multiple-setup ambient vibration tests on an eight-storey office building and a suspension footbridge. The field tests were designed based on conventional planning considerations. The test configurations have been quantitatively assessed using the uncertainty law of multiple setups. The global mode shape c.o.v. based on the current test configuration has been compared with that for other possible settings. The results show that the setting used was able to provide identification accuracy to an acceptable level.

Chapter 6 Conclusions and future work

6.1 Conclusions

Uncertainty quantification and management in multiple-setup OMA have been addressed in this thesis. The main contributions lie in uncertainty computation, uncertainty management and field test applications.

In uncertainty computation, a theoretical framework has been developed to derive the Hessian of a function subjected to constraints. Based on Bayesian system identification, the developed theory has been used to derive the posterior covariance matrix. Two formulae have been developed in a systematic manner in order to handle constraints. One is applicable for general parameter value. The other is only applicable at the MPV but the formulation is more compact. The formulae have been applied to Bayesian modal identification with single setup and multiple-setup data. The proposed theory has been validated using synthetic data.

In uncertainty management, the long data asymptotic behaviour of the posterior covariance matrix has been investigated. Closed-form expressions of the leading order posterior c.o.v. of the modal parameters have been developed based on sufficiently long data and small damping. The developed theory has been validated using synthetic, laboratory and field test data. The proposed uncertainty law reveals the relationship between the uncertainty of modal parameters and the test configuration. It allows the multiple-setup test configuration to be designed and quantitatively assessed from an uncertainty point of view. Through a parametric study of the posterior global mode

shape c.o.v., scientific guidance for multiple-setup planning has been made. Targeting for a single mode, it is suggested that the reference sensors should be placed at the locations so that their sum of the squared mode shape values is as large as possible. As long as the reference sensors are deployed in a good position, it does not matter how the roving sensors are planned, since different settings give similar level of uncertainty. This finding simplifies the planning of roving sensors, allowing one to focus on other planning aspects.

The theories developed in Chapter 3 and Chapter 4 have been applied to multiple-setup field tests on an eight-storey office building and a suspension footbridge. Identification uncertainties have been calculated and appraised using the uncertainty law.

6.2 Future work

There are several research directions that may be pursued in future studies regarding the investigation of uncertainty in OMA.

1) The theoretical framework developed in Chapter 2 for deriving the Hessian of a function subjected to constraints can be applied to handle general constraints in Bayesian system identification. Besides mode shape scaling constraint that has been investigated, it can also be applied to handle other constraints, such as symmetry in the covariance matrices for noise in a state-space model.

2) The research on uncertainty management in this work has only focused on well-separated modes with multiple-setup data. Based on the connection of the posterior covariance and the FIM, it may be possible to derive the posterior uncertainty for unexplored cases, such as close modes and asynchronised data.

3) This work has established the relationship between uncertainty and multiple-setup test configuration, which allows the planning work to be designed from an uncertainty point of view. Standardising ambient vibration tests requires considering a variety of situations. Uncertainty is only one of the aspects. Due to the complication of the problem, it has yet to be fully addressed.

LIST OF PUBLICATIONS

Journal papers

[1] Siu-Kui Au, **Yan-Long Xie***, Calculation of Hessian under constraints with applications to Bayesian system identification, Comput. Methods Appl. Mech. Eng. 323 (2017) 373–388. [download]

[2] Yi-Chen Zhu*, **Yan-Long Xie**, Siu-Kui Au, Operational modal analysis of an eight-storey building with asynchronous data incorporating multiple setups, Eng. Struct. 165 (2018) 50–62. [download]

[3] Daniele Benito Calla, **Yan-Long Xie**, Giacinto Porco*, Operational modal analysis for prototype reinforced concrete structures, comparison before and after damage, Eng. Struct. (submitted).

[4] **Yan-Long Xie*,** Siu-Kui Au, Uncertainty management in operational modal analysis incorporating multiple setups (under preparation).

[5] **Yan-Long Xie*,** Siu-Kui Au, On assessing multiple-setup configurations in operational modal analysis of a suspension footbridge (under preparation).

Conference papers

[1] **Yan-Long Xie***, Yi-Chen Zhu, Siu-Kui Au, Operational modal analysis of Brodie Tower using a Bayesian approach, in: 2nd Int. Conf. Uncertain. Quantif. Comput. Sci. Eng., 2017. [download]

REFERENCES

[1] M. Sánchez-silva, D.M. Frangopol, J. Padgett, M. Soliman, Maintenance and Operation of Infrastructure Systems : Review, Am. Soc. Civ. Eng. 142 (2016) 1–16.

[2] D.M. Frangopol, M. Liu, Maintenance and management of civil infrastructure based on condition, safety, optimization, and life-cycle cost, Struct. Infrastruct. Eng. 3 (2007) 29–41.

[3] S.E. Chang, M. Shinozuka, Life-Cycle Cost Analysis with Natural Hazard Risk, J. Infrastruct. Syst. 2 (1996) 118–126.

[4] Infrastructure UK, Infrastructure Cost Review: annual report 2012-2013, HM Treasury, London, 2013.

[5] Infrastructure and Projects Authority, National Infrastructure Delivery Plan 2016-2021, HM Treasury and Cabinet Office, London, 2016.

[6] H. Sohn, C.R. Farrar, F. Hemez, J. Czarnecki, A review of structural health monitoring literature 1996-2001, Third World Conf. Struct. Control. (2002) 1–7.

[7] C.R. Farrar, K. Worden, An introduction to structural health monitoring, Philos. Trans. R. Soc. A Math. Phys. Eng. Sci. 365 (2007) 303–315.

[8] J.M.W. Brownjohn, Structural health monitoring of civil infrastructure, Philos. Trans. R. Soc. A Math. Phys. Eng. Sci. 365 (2007) 589–622.

[9] D.E. Hudson, Dynamic tests of full-scale structures, J. Eng. Mech. Div. 103 (1977) 1141–1157.

[10] A. Cunha, E. Caetano, R. Delgado, Dynamic tests on large cable-stayed bridge, J. Bridg. Eng. 6 (2001) 54–62.

[11] O.S. Salawu, C. Williams, Review of full-scale dynamic testing of bridge structures, Eng. Struct. 17 (1995) 113–121.

[12] F.J. Cara, J. Juan, E. Alarcón, State space models for multi-setup operational modal analysis, (2014) 2471–2476.

[13] E. Reynders, F. Magalhaes, G. Roeck, A. Cunha, Merging Strategies for Multi-Setup Operational Modal Analysis, IMAC 27, Int. Modal Anal. Conf. (2009).

[14] J.M.W. Brownjohn, S.K. Au, Y. Zhu, Z. Sun, B. Li, J. Bassitt, E. Hudson, H. Sun, Bayesian operational modal analysis of Jiangyin Yangtze River Bridge, Mech. Syst. Signal Process. 110 (2018) 210–230.

[15] J. Brownjohn, S.K. Au, B. Li, J. Bassitt, Optimised ambient vibration testing of

long span bridges, Procedia Eng. 199 (2017) 38–47.

[16] F.L. Zhang, H.B. Xiong, W.X. Shi, X. Ou, Structural health monitoring of Shanghai Tower during different stages using a Bayesian approach, Struct. Control Heal. Monit. 23 (2016) 1366–1384.

[17] Y. Pan, C.E. Ventura, Y. Feng, X. Li, Y. Kaya, H. Xiong, F. Zhang, J. Cao, Ambient Vibration Testing of a Super Tall Building in Shanghai, in: Conf. Proc. Soc. Exp. Mech. Ser., 2016: pp. 155–162.

[18] D.J. Ewins, Modal Testing: Theory, Practice and Application, Research Stuhes Press Ltd, 2000.

[19] S. Živanović, A. Pavic, P. Reynolds, Vibration serviceability of footbridges under human-induced excitation: a literature review, J. Sound Vib. 279 (2005) 1–74.

[20] ISO, Design of structures-serviceability of buildings against vibrations, (1992).

[21] S.H. Strogatz, D.M. Abrams, A. McRobie, B. Eckhardt, E. Ott, Theoretical mechanics: Crowd synchrony on the Millennium Bridge, Nature. 438 (2005) 43.

[22] N. Satake, K. Suda, T. Arakawa, A. Sasaki, Y. Tamura, Damping evaluation using full-scale data of buildings in Japan, J. Struct. Eng. 129 (2003) 470–477.

[23] R. Smith, R. Merello, M. Willford, Intrinsic and supplementary damping in tall buildings, Proc. Inst. Civ. Eng. Build. 163 (2010) 111–118.

[24] Y. Xia, H. Hao, J.M.W. Brownjohn, P.Q. Xia, Damage identification of structures with uncertain frequency and mode shape data, Earthq. Eng. Struct. Dyn. 31 (2002) 1053–1066.

[25] T.Y. Kam, T.Y. Lee, Detection of cracks in structures using modal test data, Eng. Fract. Mech. 42 (1992) 381–387.

[26] J.M. Ricles, J.B. Kosmatka, Damage detection in elastic structures using vibratory residual forces and weighted sensitivity, AIAA J. 30 (1992) 2310–2316.

[27] B. Rune, V. Carlos, Introduction to operational modal analysis, John Wiley & Sons, Ltd., 2015.

[28] Ranieri C. Fabbrocino, Operational Modal Analysis of Civil Engineering Structures, Springer New York Heidelberg Dordrecht London, 2014.

[29] G.H. James, T.G. Carne, J.P. Lauffer, The natural excitation technique (NExT) for modal parameter extraction from operating structures, Modal Anal. Int. J. Anal. Exp. Modal Anal. 10 (1995) 260.

[30] Jorge Rodrigues, Rune Brincker, Application of the Random Decrement Technique in Operational Modal Analysis, in: 1st Int. Oper. Modal Anal. Conf., 2005: pp. 191–200.

[31] J.R. Cole H, On-the-line analysis of random vibrations, in: 9th Struct. Dyn. Mater. Conf., 1968: p. 288.

[32] S.R. Ibrahim, Random decrement technique for modal identification of structures, J. Spacecr. Rockets. 14 (1977) 696–700.

[33] D.L. Brown, R.J. Allemang, R. Zimmerman, M. Mergeay, Parameter estimation techniques for modal analysis, SAE Trans. (1979) 828–846.

[34] H. Vold, J. Kundrat, G.T. Rocklin, R. Russell, A multi-input modal estimation algorithm for mini-computers, SAE Trans. (1982) 815–821.

[35] J. Juang, R.S. Pappa, An eigensystem realization algorithm for modal parameter identification and model reduction, J. Guid. Control. Dyn. 8 (1985) 620–627.

[36] B. Piombo, E. Giorcelli, L. Garibaldi, A. Fasana, Structures identification using ARMAV models, in: Proc. Int. Modal Anal. Conf., SEM SOCIETY FOR EXPERIMENTAL MECHANICS INC, 1993: p. 588.

[37] D. Shi, W. Stühler, Modal analysis with AR (ARMA) model and unknown excitation, in: Int. Modal Anal. Conf. 5 Th, London, Engl., 1987: pp. 1171–1176.

[38] D. Prevosto, A. Benveniste, D. Bonnecase, Application of a multidimensional ARMA model to modal analysis under natural excitation, in: Proc. 8th Int. Modal Anal. Conf. Kissimmee, FL, USA, 1990: pp. 382–388.

[39] L. Ljung, System identification: theory for the user, Prentice-hall, 1987.

[40] P. Andersen, Identification of civil engineering structures using vector ARMA models, (1997).

[41] J.B. Bodeux, J.C. Golinval, Application of ARMAV models to the identification and damage detection of mechanical and civil engineering structures, Smart Mater. Struct. 10 (2001) 479.

[42] R. Brincker, P. Andersen, ARMA models in modal space, in: Proc. 17th Int. Modal Anal. Conf. Kissimee, Florida, 1999.

[43] L. Zhang, R. Brincker, P. Andersen, An Overview of Operational Modal Analysis : Major Development and Issues, 1st Int. Oper. Modal Anal. Conf. (2005) 12.

[44] P. Van Overschee, B. De Moor, Subspace algorithms for the stochastic identification problem, in: Decis. Control. 1991., Proc. 30th IEEE Conf., IEEE, 1991: pp. 1321–1326.

[45] P. Van Overschee, B.L. De Moor, Subspace identification for linear systems: Theory, Implementation, Applications, Springer Science & Business Media, 2012.

[46] B. Peeters, G. De Roeck, Stochastic system identification for operational modal analysis: a review, J. Dyn. Syst. Meas. Control. 123 (2001) 659.

[47] L. Mevel, M. Goursat, M. Basseville, Stochastic subspace-based structural identification and damage detection and localisation-application to the Z24 bridge benchmark, Mech. Syst. Signal Process. 17 (2003) 143–151.

[48] Y. Liu, C. Loh, Y. Ni, Stochastic subspace identification for output- only modal analysis: application to super high-rise tower under abnormal loading condition, Earthq. Eng. Struct. Dyn. 42 (2013) 477–498.

[49] J.M.W. Brownjohn, F. Magalhaes, E. Caetano, A. Cunha, Ambient vibration re-testing and operational modal analysis of the Humber Bridge, Eng. Struct. 32 (2010) 2003–2018.

[50] A.J. Felber, Development of a hybrid bridge evaluation system, (1994).

[51] R.J. Allemang, Experimental modal analysis for vibrating structures, (1983).

[52] D.J. Ewins, Modal testing: theory, practice and application (mechanical engineering research studies: engineering dynamics series), Res. Stud. Pre, 2nd Ed., ISBN-13. (2000) 978–863802188.

[53] R. Brincker, L. Zhang, P. Andersen, Modal Identification from Ambient Responses using Frequency Domain Decomposition, 18th Int. Modal Anal. Conf. (2000) 625–630.

[54] R. Brincker, C. Ventura, P. Andersen, Damping estimation by frequency domain decomposition, in: 19th Int. Modal Anal. Conf., 2001: pp. 698–703.

[55] L. Zhang, T. Wang, Y. Tamura, A frequency-spatial domain decomposition (FSDD) method for operational modal analysis, Mech. Syst. Signal Process. 24 (2010) 1227–1239.

[56] J.L. Beck, K. Yuen, Bayesian Probabilistic Approach, J. Eng. Mech. 130. No. 2 (2004) 192–203.

[57] K. Yuen, L.S. Katafygiotis, Bayesian time-domain approach for modal updating using ambient data, Probabilistic Eng. Mech. 16 (2001).

[58] S.K. Au, F.L. Zhang, Y.C. Ni, Bayesian operational modal analysis: Theory, computation, practice, Comput. Struct. 126 (2013) 3–14.

[59] D.R. Brillinger, Time series: data analysis and theory, Siam, 1981.

[60] S.K. Au, Operational Modal Analysis: Modeling, Bayesian Inference, Uncertainty Laws, Springer, 2017.

[61] K. Yuen, L.S. Katafygiotis, Bayesian spectral density approach for modal updating using ambient data, Earthq. Eng. Struct. Dyn. 30 (2001) 1103–1123.

[62] K. Yuen, L.S. Katafygiotis, Bayesian Fast Fourier Transform Approach for Modal Updating Using Ambient Data, Adv. Struct. Eng. 6 (2009) 81–95.

[63] S.K. Au, Fast Bayesian FFT method for ambient modal identification with separated modes, J. Eng. Mech. 137 (2011) 214–226.

[64] S.K. Au, Fast Bayesian ambient modal identification in the frequency domain, Part I: Posterior most probable value, Mech. Syst. Signal Process. 26 (2012) 60–75.

[65] S.K. Au, F.L. Zhang, Fast Bayesian ambient modal identification incorporating multiple setups, J. Eng. Mech. 138 (2012) 800–815.

[66] Y.C. Zhu, S.K. Au, Bayesian operational modal analysis with asynchronous data, part I: Most probable value, Mech. Syst. Signal Process. 98 (2018) 652–666.

[67] S.K. Au, Y.C. Ni, F.L. Zhang, H.F. Lam, Full-scale dynamic testing and modal identification of a coupled floor slab system, Eng. Struct. 37 (2012) 167–178.

[68] S.K. Au, F.L. Zhang, P. To, Field observations on modal properties of two tall buildings under strong wind, J. Wind Eng. Ind. Aerodyn. 101 (2012) 12–23.

[69] Y.L. Xie, Y. C. Zhu, S.K. Au, Operational modal analysis of Brodie Tower using a Bayesian approach, in: 2nd Int. Conf. Uncertain. Quantif. Comput. Sci. Eng., 2017.

[70] L. Mevel, M. Basseville, A. Benveniste, M. Goursat, Merging sensor data from multiple measurement set-ups for non-stationary subspace-based modal analysis, J. Sound Vib. 249 (2002) 719–741.

[71] F.J. Cara, J. Carpio, J. Juan, E. Alarcón, An approach to operational modal analysis using the expectation maximization algorithm, Mech. Syst. Signal Process. 31 (2012) 109–129.

[72] S.K. Au, Assembling mode shapes by least squares, Mech. Syst. Signal Process. 25 (2011) 163–179.

[73] E. Orlowitz, P. Andersen, A. Brandt, Comparison of Simultaneous and Multi-Setup Measurement Strategies in Operational Modal Analysis, in: 6th Int. Oper. Modal Anal. Conf., 2015.

[74] E. Parloo, P. Guillaume, B. Cauberghe, Maximum likelihood identification of non-stationary operational data, J. Sound Vib. 268 (2003) 971–991.

[75] M. Dohler, E. Reynders, F. Magalhaes, L.Mevel, G. De Reock, A. Cunha, Pre- and Post-identification Merging for Multi-Setup OMA with Covariance-Driven SSI, in: IMAC-XXVIII, 2010: pp. 57–70.

[76] F.J. Cara, J. Juan, E. Alarcón, Estimating the modal parameters from multiple measurement setups using a joint state space model, Mech. Syst. Signal Process. 43 (2014) 171–191.

[77] S. Ciloglu, The impact of uncertainty in operational modal analysis for structural identification of constructed systems, Drexel University, 2006.

[78] K. Ciloglu, Y. Zhou, F. Moon, A.E. Aktan, Impacts of Epistemic Uncertainty in Operational Modal Analysis, J. Eng. Mech. 138 (2012) 1059–1070.

[79] F.L. Moon, A.E. Aktan, Impacts of epistemic (bias) uncertainty on structural identification of constructed (civil) systems, Shock Vib. Dig. 38 (2006) 399–420.

[80] E. Reynders, R. Pintelon, G. De Roeck, Uncertainty bounds on modal parameters obtained from stochastic subspace identification, Mech. Syst. Signal Process. 22 (2007) 948–969.

[81] P. Andersen, R. Brincker, Estimation of modal parameters and their uncertainties, 17th Int. Modal Anal. Conf. IMAC. 1 (1999) 323–329.

[82] R. Pintelon, P. Guillaume, J. Schoukens, Uncertainty calculation in (operational) modal analysis, Mech. Syst. Signal Process. 21 (2007) 2359–2373.

[83] M. Döhler, X.B. Lam, L. Mevel, Uncertainty quantification for modal parameters from stochastic subspace identification on multi-setup measurements, Mech. Syst. Signal Process. 36 (2013) 562–581.

[84] M. Döhler, L. Mevel, Efficient multi-order uncertainty computation for stochastic subspace identification, Mech. Syst. Signal Process. 38 (2013) 346–366.

[85] X.B. Lam, L. Mevel, Uncertainty quantication for Eigensystem-Realization-Algorithm, a class of Subspace system Identication, IFAC, 2011.

[86] S. Chauhan, Quantifying uncertainty in modal parameters estimated using higher order time domain algorithms, in: Model Valid. Uncertain. Quantif., 2014: pp. 317–325.

[87] S.K. Au, Fast Bayesian ambient modal identification in the frequency domain, Part II: Posterior uncertainty, Mech. Syst. Signal Process. 26 (2012) 76–90.

[88] F.L. Zhang, S.K. Au, H.F. Lam, Assessing uncertainty in operational modal analysis incorporating multiple setups using a Bayesian approach, Struct. Control Heal. Monit. 22 (2014) 395–416.

[89] Y.C. Zhu, S.K. Au, Bayesian operational modal analysis with asynchronous data, Part II: Posterior uncertainty, Mech. Syst. Signal Process. 98 (2018) 920-935.

[90] S.K. Au, J.M.W. Brownjohn, J.E. Mottershead, Quantifying and managing uncertainty in operational modal analysis, Mech. Syst. Signal Process. 102 (2018) 139–157.

[91] S.K. Au, Uncertainty law in ambient modal identification, Part I: Theory, Mech. Syst. Signal Process. 48 (2014) 15–33.

[92] S.K. Au, B. Li, Posterior uncertainty, asymptotic law and Cramér-Rao bound, Struct. Control Heal. Monit. 25 (2018) 1–21.

[93] S.K. Au, Uncertainty law in ambient modal identification, Part II: Implication and field verification, Mech. Syst. Signal Process. 48 (2014) 15–33.

[94] H. Cramér, Mathematical methods of statistics (PMS-9), Princeton university press, 2016.

[95] C.W. De Silva, Vibration monitoring, testing, and instrumentation, 2007.

[96] M. Papadopoulos, E. Garcia, Sensor placement methodologies for dynamic testing, AIAA J. 36 (1998) 256–263.

[97] B. Schwarz, M. Richardson, P. Avitabile, Locating optimal references for modal testing, Proc. IMAC-XX A Conf. Struct. Dyn. 4753 II (2002) 984–990.

[98] J. Zhang, K. Maes, G. De Roeck, E. Reynders, C. Papadimitriou, G. Lombaert, Optimal sensor placement for multi-setup modal analysis of structures, J. Sound Vib. 401 (2017) 214–232.

[99] D.J. Chmielewski, T. Palmer, V. Manousiouthakis, On the theory of optimal sensor placement, AIChE J. 48 (2002) 1001–1012.

[100] C. Papadimitriou, G. Lombaert, The effect of prediction error correlation on optimal sensor placement in structural dynamics, Mech. Syst. Signal Process. 28 (2012) 105–127.

[101] Z.H. Qureshi, T.S. Ng, G.C. Goodwin, Optimum experimental design for identification of distributed parameter systems, Int. J. Control. 31 (1980) 21–29.

[102] F.E. Udwadia, Methodology for optimum sensor locations for parameter identification in dynamic systems, J. Eng. Mech. 120 (1994) 368–390.

[103] D.C. Kammer, Sensor placement for on-orbit modal identification and correlation of large space structures, J. Guid. Control. Dyn. 14 (1991) 251–259.

[104] E. Heredia-Zavoni, L. Esteva, Optimal instrumentation of uncertain structural systems subject to earthquake ground motions, Earthq. Eng. Struct. Dyn. 27 (1998) 343–362.

[105] S. Borguet, O. Léonard, The Fisher information matrix as a relevant tool for sensor selection in engine health monitoring, Int. J. Rotating Mach. 2008 (2008).

[106] C. Papadimitriou, J.L. Beck, S.K. Au, Entropy-Based Optimal Sensor Location for Structural Model Updating, J. Vib. Control. 6 (2000) 781–800.

[107] C. Papadimitriou, Optimal sensor placement methodology for parametric identification of structural systems, J. Sound Vib. 278 (2004) 923–947.

[108] B. Li, A. Der Kiureghian, Robust optimal sensor placement for operational modal analysis based on maximum expected utility, Mech. Syst. Signal Process. 75 (2016) 155–175.

[109] C. Argyris, C. Papadimitriou, P. Panetsos, Bayesian Optimal Sensor Placement for Modal Identification of Civil Infrastructures, J. Smart Cities. 2 (2017) 69–86.

[110] B. Li, D. Li, X. Zhao, J. Ou, Optimal sensor placement in health monitoring of suspension bridge, Sci. China Technol. Sci. 55 (2012) 2039–2047.

[111] M. Meo, G. Zumpano, On the optimal sensor placement techniques for a bridge structure, Eng. Struct. 27 (2005) 1488–1497.

[112] M. Meo, G. Zumpano, Optimal sensor placement on a large-scale civil structure, in: Proc. SPIE - Int. Soc. Opt. Eng., 2004: p. 108.

[113] T.H. Yi, H.N. Li, X.D. Zhang, Sensor placement on Canton Tower for health monitoring using asynchronous-climb monkey algorithm, Smart Mater. Struct. 21 (2012).

[114] D. Yoganathan, S. Kondepudi, B. Kalluri, S. Manthapuri, Optimal Sensor Placement Strategy for Office Buildings Using Clustering Algorithms, Energy Build. 158 (2017) 1206–1225.

[115] C. Leyder, V. Dertimanis, A. Frangi, E. Chatzi, G. Lombaert, Optimal sensor placement methods and metrics-comparison and implementation on a timber frame structure, Struct. Infrastruct. Eng. 2479 (2018) 1–14.

[116] N. Debnath, A. Dutta, S.K. Deb, Placement of sensors in operational modal analysis for truss bridges, Mech. Syst. Signal Process. 31 (2012) 196–216.

[117] J.E.T. Penny, M.I. Friswell, S.D. Garvey, Automatic choice of measurement locations for dynamic testing, AIAA J. 32 (1994) 407–414.

[118] J.A. Wilson, S.Y. Guhe, Observability matrix condition number in design of measurement strategies, Comput. Aided Chem. Eng. 20 (2005) 397–402.

[119] M. Brehm, V. Zabel, C. Bucher, Optimal reference sensor positions using output-only vibration test data, Mech. Syst. Signal Process. 41 (2013) 196–225.

[120] K.J. Keesman, System Identification: An Introduction, Springer London, London, 2011.

[121] D.M. Siringoringo, Y. Fujino, System identification of suspension bridge from ambient vibration response, Eng. Struct. 30 (2008) 462–477.

[122] P.L. Green, Bayesian system identification of a nonlinear dynamical system using a novel variant of Simulated Annealing, Mech. Syst. Signal Process. 52 (2015) 133–146.

[123] G. Kerschen, K. Worden, A.F. Vakakis, J.C. Golinval, Past, present and future of nonlinear system identification in structural dynamics, Mech. Syst. Signal Process. 20 (2006) 505–592.

[124] Lennart Ljung, System Identification: Theory for the User.pdf, P T R Prentice Hall, 1987.

[125] J.L. Beck, Bayesian system identification based on probability logic, Struct. Control Heal. Monit. 17 (2010) 825–847.

[126] C. Soize, E. Capiez-Lernout, J.F. Durand, C. Fernandez, L. Gagliardini, Probabilistic model identification of uncertainties in computational models for dynamical systems and experimental validation, Comput. Methods Appl. Mech. Eng. 198 (2008) 150–163.

[127] H.A. Jensen, C. Vergara, C. Papadimitriou, E. Millas, The use of updated robust reliability measures in stochastic dynamical systems, Comput. Methods Appl. Mech. Eng. 267 (2013) 293–317.

[128] J.L. Beck, Katafygiotis, Updating models and their uncertainties. I: Bayesian Statistical Framework, (1998).

[129] E. Reynders, F. Magalhaes, G. De Roeck, A. Cunha, Merging strategies for multi-setup operational modal analysis: application to the Luiz I steel arch bridge, in: Proc. IMAC, 2009.

[130] X. Shi, Y. Wu, Y. Liu, A note on asymptotic approximations of inverse moments of nonnegative random variables, Stat. Probab. Lett. 80 (2010) 1260–1264.

[131] H. Scheffé, H. Cramér, Mathematical methods of statistics, Bull. Am. Math. Soc. 53 (1947) 733–735.

[132] Y.L. Tong, The multivariate normal distribution, Springer Science & Business Media, 2012.

[133] S.K. Au, F.L. Zhang, On assessing the posterior mode shape uncertainty in ambient modal identification, Probabilistic Eng. Mech. 26 (2011) 427–434.